AD_____

Award Number: DAMD17-97-1-7261

TITLE: Non-Invasive Determination of Breast Cancer Oxygen Tension
by F-19 NMR and Breast Cancer Physiology in Response to
Radiotherapy

PRINCIPAL INVESTIGATOR: Yulin Song

CONTRACTING ORGANIZATION: The University of Texas Southwestern
Medical Center at Dallas
Dallas, Texas 75390-9105

REPORT DATE: August 2000

TYPE OF REPORT: Annual

PREPARED FOR: U.S. Army Medical Research and Materiel Command
Fort Detrick, Maryland 21702-5012

DISTRIBUTION STATEMENT: Approved for Public Release;
Distribution Unlimited

The views, opinions and/or findings contained in this report are
those of the author(s) and should not be construed as an official
Department of the Army position, policy or decision unless so
designated by other documentation.

20010424 079

REPORT DOCUMENTATION PAGE

OMB No. 074-0188

1. AGENCY USE ONLY (Leave blank)	2. REPORT DATE August 2000	3. REPORT TYPE AND DATES COVERED Annual (1 Aug 99 – 31 Jul 00)

4. TITLE AND SUBTITLE
Non-Invasive Determination of Breast Cancer Oxygen Tension by F-19 NMR and Breast Cancer Physiology in Response to Radiotherapy

5. FUNDING NUMBERS
DAMD17-97-1-7261

6. AUTHOR(S)
Yulin Song

7. PERFORMING ORGANIZATION NAME(S) AND ADDRESS(ES)
The University of Texas Southwestern Medical Center at Dallas
Dallas, Texas 75390- 9105

E-MAIL:
song1058@hotmail.com

8. PERFORMING ORGANIZATION REPORT NUMBER

9. SPONSORING / MONITORING AGENCY NAME(S) AND ADDRESS(ES)
U.S. Army Medical Research and Materiel Command
Fort Detrick, Maryland 21702-5012

10. SPONSORING / MONITORING AGENCY REPORT NUMBER

11. SUPPLEMENTARY NOTES
This report contains colored photos

12a. DISTRIBUTION / AVAILABILITY STATEMENT
Approved for public release; distribution unlimited

12b. DISTRIBUTION CODE

13. ABSTRACT (Maximum 200 Words)

The goals of this **Predoctoral Traineeship** were two-fold: 1) To provide me with the solid and extensive training and valuable experience in a modern NMR laboratory for a career as a clinical medical physicist and a breast cancer research scientist; 2) To develop and investigate a non-invasive technique of measuring oxygen tension in breast cancer based on ^{19}F MRI of hexafluorobenzene(HFB). For the past three years, I have learned tumor biology, tumor histology, tumor modeling, surgical techniques for implanting tumors, electronic techniques of designing, constructing, and testing MRI RF coils, MRI data acquisitions, Computer programming, digital signal and image processing, near-infrared spectroscopy (NIRS), and operation of advanced medical systems and instruments. In addition, I designed and constructed a double-tuned (^{19}F-^{1}H) birdcage resonator and a switchable slotted tube resonator. I wrote several computer programs for acquiring and processing MRI and NIRS data. I developed a mathematical model for describing tumor hemodynamics following physiological perturbations, and a second mathematical model for computing tumor oxygen consumption following KCl-induced cardiac arrest using NIRS. I found that the HFB signal intensity decays exponentially with a typical biological half-life ranging from $T_{1/2} = 700$ to 1200 minutes. The global and regional clearance and redistribution of HFB within the tumors did not interfere with ^{19}F MRI oximetry. The local response to respiratory challenge depended strongly on initial baseline pO_2 in breast tumor NF13762, with voxels of high baseline pO_2 showing significant changes in pO_2, while voxels of low baseline pO_2 showed small changes. Irradiation delayed tumor growth and caused changes in tumor oxygenation.

14. SUBJECT TERMS
Breast Cancer, Hexafluorobenzene (HFB), Perfluorocarbon (PFC), ^{19}F NMR, Echo Planar Imaging (EPI), Near-Infrared Spectroscopy (NIRS) pO_2, sO_2, Hemoglobin.

15. NUMBER OF PAGES
122

16. PRICE CODE

17. SECURITY CLASSIFICATION OF REPORT Unclassified	18. SECURITY CLASSIFICATION OF THIS PAGE Unclassified	19. SECURITY CLASSIFICATION OF ABSTRACT Unclassified	20. LIMITATION OF ABSTRACT Unlimited

NSN 7540-01-280-5500

Standard Form 298 (Rev. 2-89)
Prescribed by ANSI Std. Z39-18
298-102

TABLE OF CONTENTS

1. INTRODUCTION

The fundamental goals of this **Predoctoral Traineeship** were three-fold: 1) to provide me with an opportunity to continue to learn and apply the state of the art NMR technology and radiotherapy techniques to cancer diagnosis and treatment; 2) to provide me with a solid and extensive training, and valuable experience in a modern NMR laboratory for a career as a clinical medical physicist and a breast cancer research scientist; and 3) to develop and investigate a non-invasive technique of measuring oxygen tension (pO_2) in breast cancers in an animal model based on ^{19}F MRI of hexafluorobenzene (HFB), now called the **FREDOM** (**F**luorocarbon **R**elaxometry using **E**cho planar imaging for **D**ynamic **O**xygen **M**apping). In this report, I will summarize the highlights of my past three-year's training and research as originally proposed in my **Predoctoral Traineeship** application.

2. TRAINING ACCOMPLISHMENTS

For the past three years, under the guidance of my mentor, Dr. Ralph P. Mason, I have gone through a rigorous training in tumor biology, tumor histology, tumor modeling, tumor implantation and transplantation, radiation biology, MRI physics, MRI RF coil design, construction, and testing, MRI data acquisitions, computer programming, digital signal and image processing, near-infrared spectroscopy (**NIRS**), experimental design, and data analysis. I have learned how to use many advanced medical systems and instruments. As an important part of my doctoral curriculum training and research, I needed to use an Omega CSI 4.7 T MR system with actively shielded gradients (Acustar^{TM}, Bruker Instruments, Inc., Fremont, CA, USA). This system, based on a 40-cm diameter bore horizontal magnet, is located in the Rogers Magnetic Resonance Center of the University of Texas Southwestern Medical Center at Dallas, which is an NIH Biotechnology Resource Facility. I had immediate access to the system and other resources in the center, and, on average, I used the system three days per week in the past for either experiments or data processing and programming. Now I can operate the magnet independently for both imaging and spectroscopy experiments. To meet our particular experimental needs, I modified and wrote several data acquisition and post-processing programs. These include an NMR-shell script program for computing the biological half-life of hexafluorobenzene (**HFB**) in rat breast tumors, an NMR-shell script program for displaying the T1 relaxation curve of individual voxels of MR EPI images, a C and NMR-shell script program for acquiring BOLD and Gd-DTPA data, a C program for converting MRI image files among different platforms, a Visual Basic program for processing MRI EPI data, and a LabView program for processing near-infrared spectroscopy (**NIRS**) data. In addition, I have also learned how to use electronic

instruments commonly seen in a modern RF lab, including a sophisticated HP Frequency Analyzer, and how to operate center lathes and milling machines frequently encountered in the machine shop of a radiology department. These are the necessary skills required for a professional medical physicist and biomedical engineer. With these skills, I designed, constructed, and tested a double-tuned (^{19}F-^{1}H) birdcage resonator and a switchable slotted tube resonator. Both phantom testing and *in vivo* imaging experiments indicated that the two resonators worked well. In addition, I have been working on a new type of RF coil, which combines a traditional RF coil with NIRS. These coils will allow simultaneous measurement of tumor tissue pO_2 by ^{19}F MRI, tumor vascular oxyhemoglobin concentration [HbO_2], and total hemoglobin concentration [Hb]$_{Total}$ by NIRS. This is a challenging task and successful completion of these RF coils would be significant in tumor oximetry. Another goal of this **Predoctoral Traineeship** was to investigate breast tumor physiology in response to therapeutic interventions. This required the use of rat mammary adenocarcinoma 13762NF. Implanting this type of tumor in female Fisher 344 rats in a pedicle model was a complicated and lengthy surgical procedure. Now I have learned the techniques and can do the surgery without any difficulties. I have also learned the techniques of blood gas analysis using fiber optic pulse oximeter and the operation of automated microelectrode systems. Besides comprehensive hands-on training, I developed a mathematical model for describing tumor hemodynamics following physiological perturbations, and a second mathematical model for computing tumor oxygen consumption following KCl-induced cardiac arrest using NIRS.

3. RESEARCH ACCOMPLISHMENTS

1) Background Information

Solid tumors develop regions of hypoxia during their growth due to an imbalance between the rate of tumor cell proliferation and the proliferation and branching of the blood vessels [1-3], leading to diffusion-limited or chronic hypoxia. However, tumor hypoxia can also occur due to another important reason, the deficient oxygen-carrying capacity of the blood, *i.e.*, low blood hemoglobin concentration, as observed in the case of anemic cancer patients [4-6]. Substantial clinical evidence has indicated that it is the hypoxia that is responsible for the failure of radiotherapy [7-10], some forms of chemotherapy [11, 12], and photodynamic therapy [13]. Moreover, considerable clinical studies have also shown that tumor hypoxia plays a key role for increased expression of many genes that relate to tumor angiogenesis and growth, including vascular endothelial growth factor (**VEGF**), platelet-derived growth factor (**PDGF**), and p53 [14, 15], and low oxygenation levels in tumors correlate with a higher metastatic rate [16-18]. Although the mechanism for the latter effect has not been fully understood, some studies have suggested that it could be caused by increased DNA mutation rate and overreplication

under the hypoxic condition [19-21]. In addition, a number of clinical trials have found that patient survival, measured either as tumor regression or as local control, depends largely on tumor oxygenation [10, 16, 22, 23].

Recently, the use of erythropoietin treatment and blood transfusion has gained increasing attention and popularity in tumor therapy community [24, 25] because many clinical studies have shown that there is a relationship between hemoglobin concentrations and therapeutic outcome [26, 27]. Results of several other clinical trials have indicated that higher hemoglobin concentrations correlate with improved local tumor control and a higher overall survival rate [28, 29], suggesting that hemoglobin concentration could be an independent prognostic factor in tumor therapy. However, the exact mechanism how hemoglobin concentrations affect tumor therapy and radiotherapy in particular is still being debated [30]. Available experimental and clinical data seem to support the hypothesis that low hemoglobin concentrations impair oxygen-transporting capacity of blood and eventually lead to tumor hypoxia. In view of the important role of hemoglobin in tumor therapy, it is necessary to have a means to measure and manipulate hemoglobin levels in tumor.

The critical effects of oxygenation on tumor therapy, angiogenesis, metastasis, and prognosis have stimulated the development of novel tumor oximetry techniques. Over the past several decades, substantial progress has been made in developing techniques for measuring tumor tissue oxygen tension (pO_2) and hypoxia. These include microelectrodes [31, 32], ESR/EPR [33, 34], the comet assay [35], phosphorescence quenching imaging [36], nitroimidazole binding assays [37], paired survival assay [37] and NMR [38-40]. However, none of these has been recognized generally as a perfect noninvasive method. Electrodes are highly invasive and only sample a limited region. ESR has two major drawbacks compared with NMR: lack of tissue penetration at very high frequencies (GHz) and the inability to obtain functional information at multiple locations (mapping). ^{31}P NMR is perhaps the most attractive indicator of tumor oxygenation since it is entirely non-invasive with observation of endogenous metabolites. However, it is relatively insensitive, sampling a large volume, and metabolic hypoxia may occur at an oxygen tension that considerably exceeds radiobiological hypoxia [41]. Recent studies have indicated that tissue contrast changes in ^1H MRI on the basis of the blood oxygen level dependent (**BOLD**) method provide a qualitative approach to tissue oxygenation. However, changes in blood flow affect the signal intensity and therefore, complicate the interpretation of results [42, 43]. ^{19}F NMR techniques can provide a direct measurement of pO_2 based on the principle that the ^{19}F NMR spin-lattice relaxation rates R1 (=1/T1) of perfluorocarbon (**PFC**) emulsions are linearly proportional to oxygen tension [44-46]. ^{19}F has 100% natural isotopic abundance and an 83% sensitivity relative to ^1H. ^{19}F occurs in exceedingly low concentrations in biological systems (as the fluoride ion), thus, there is essentially no background noise to interfere with *in vivo* studies. ^{19}F

NMR techniques have the potential advantages of being non-invasive, repeatable, and able to produce local tumor pO_2 maps with high spatial resolution.

Tumor oxyhemoglobin concentration $[HbO_2]$ or sO_2 is another important indicator of tumor oxygenation. However, for many years, very little progress has been made in developing techniques to measure it. One promising technique is near-infrared spectroscopy (NIRS). The NIRS tumor oximetry is based on the fact that there exists a substantial absorption difference of light in NIR region (700 ~ 900 nm) between deoxyhemoglobin [Hb] and oxyhemoglogin $[HbO_2]$, while absorption of light by other macromolecules and water is insignificant. Based on light modulation mechanisms, NIRS techniques can be classified as: continuous wave (**CW**) light spectroscopy in DC format, amplitude-modulated laser light spectroscopy in frequency domain, and pulsed-laser light spectroscopy in time domain. Using NIRS techniques, *in vivo* measurements of sO_2 have been carried out in a wide variety of biological systems such as exercised muscles [47-49] and brain [50-52]. However, so far, very limited studies have been done in *in vivo* measurements of tumor sO_2. Among the published studies, NIRS has been used to evaluate the effects of anesthetics on vascular sO_2 in RIF-1 tumors [53] and in 9L gliosarcoma [54], and to assess the effects of hypoxia, hyperoxia, and asphyxia on BA1112 rhabdomyosarcoma [55]. Recently, Mariya *et. al.* [56] has published their data on monitoring tumor oxygenation status during fractionated irradiation in two murine tumor cell lines using NIR reflection spectroscopy. NIRS is completely non-invasive, inexpensive, portable, and amenable to real-time measurements. It can be used to measure tumor vascular hemoglobin oxygen saturation sO_2, hemoglobin concentration [Hb], and tumor blood flow, and to monitor tumor transient response to therapeutic interventions. However, because of inhomogeneous nature and limited dimension of tumors, classical diffusion theory does not hold. Absolute quantification of tumor oxygenation based on photon diffusion approximation approach still remains a challenging issue. An alternative approach is to modify Beer-Lambert's law and use the measured transmitted light amplitude to compute the trends in the changing absorption coefficients and, thus, changes in $[HbO_2]$ or sO_2 and $[Hb]_{Total}$.

We have surveyed the relative sensitivity of several PFCs and found that hexafluorobenzene (HFB) offers exceptional sensitivity to changes in pO_2 with relatively little response to temperature. HFB has a single resonance, providing optimal signal-to-noise ratio (SNR). I have applied the ^{19}F MRI of HFB technique to investigate dynamic changes in pO_2 in tumors in response to respiratory challenges and the feasibility of mapping the clearance rate of HFB. In addition, I have also investigated hemodynamic changes in $[HbO_2]$ and $[Hb]_{Total}$ in tumors in response to therapeutic interventions using a newly developed NIRS system.

2) Tumor Transplantation and Handling, Tumor Volume Doubling Time (VDT), and Tumor Histology

Tumor Model

Murine mammary adenocarcinomas 13762NF [57] were used in this study. The 13762NF is a subline of mammary adenocarcinoma 13762. This tumor model was chosen because it demonstrates substantially different therapeutic sensitivity and metastatic characteristics from other tumor types. The 13762NF is less differentiated. It is inhibited by estrogen in young female rats and stimulated in adult female rats. It metastasizes to regional lymph nodes, and lung, and occasionally to liver, but not to brain. It is highly responsive to alkylating agents and platinum chemotherapeutic agents.

Tumor Transplantation and Handling

Our lab has successfully developed a tumor transplantation model, the pedicle model [58]. Murine mammary adenocarcinomas 13762NF were implanted in skin pedicles on the forebacks of adult female Fischer 344 rats (~250 g). To identify them, each tumor was assigned a unique code. The surgical procedure for creating a pedicle tumor model is as follows. A flap of depilated skin was raised from the body of the rat and held in position with a non-traumatic curved bull-dog clip. A 3-cm incision was made through the skin using the curved edge of the clip as a guide. Wound clips were used to joint the edge of the skin, producing a tube resembling a suitcase handle. Animals were housed separately after the surgery and during the entire course of experiments. Two weeks later, the clips were removed and the distal end of the pedicle severed. A piece of fresh tumor tissue (~ $2 \times 2 \times 2$ mm^3) from the first generation of mammary adenocarcinomas 13762NF was implanted in the lumen and cut closed with a wound clip.

One of the major advantages of the pedicle model is that it is basically isolated from the body proper and perfectly suited for *in vivo* NIRS and MRI studies, therapy, and manipulation. In addition, the pedicle model allows accurate measurement of tumor size. It has been shown to have no significant difference from the traditional subcutaneous site in the thigh in terms of growth [58].

Tumor Growth and Mathematical Model for Computing *VDT*

After tumors were implanted, they first entered a two-week silent period of undetected growth and then an accelerating period in which most tumors grew exponentially. Some, though they may not appear to grow exponentially over their entire life spans, did show exponential growth over short periods of time. The time for the tumors to grow to a predetermined size spanned a wide range. In some cases, the silent periods lasted more than three weeks. Once the implanted tumor tissue grew into a detectable tumor, tumor's three orthogonal dimensions were measured at least once every two days with a caliper. Depending on tumor growth rate, tumors were measured daily in some cases to improve the goodness of curve fit when computing volume doubling time (VDT). Prior to the measurements, the rats were anesthetized with 50µl ketamine hydrochloride (100 mg/ml) and the tumors' hair was cut with a pair of surgical scissors to

improve the accuracy of the measurements. Using an ellipsoidal approximation, tumor volume was determined using formula

$$V = (\frac{4\pi}{3}) \cdot (\frac{a}{2}) \cdot (\frac{b}{2}) \cdot (\frac{c}{2}) = (\frac{\pi}{6}) \cdot a \cdot b \cdot c \qquad (1)$$

where a, b, and c were the diameters along the three major orthogonal axes of the tumor. A very important proliferative feature of the solid tumors is their volume doubling time (VDT) (day), a kinetic parameter closely related to the underlying mathematical growth model.

Historically, a growing tumor is modeled as a deterministic dynamic system mathematically described by ordinary differential equations. The central concept of a dynamic system is the trajectory. In the case of tumor growth, the trajectory is the growth curve that describes the change in tumor size as a function of time from the start of proliferation of initial tumor cells. The tumor size can be expressed as dimensions or volume or mass or cellularity, depending on personal choice. For tumor modeling, these quantities are interchangeably used, because they are linearly proportional to each other for solid tumors. Unfortunately, most of these tumor growth models have been seldom validated against experimental tumor growth curves, either because of the relative scarcity of high quality tumor growth data [59]. Limited accurately measured tumor data revealed that growth curves for some human tumors are very close to exponential function [60], yielding a constant volume doubling time. However, other studies indicated that many human tumors also show irregular or decelerating growth, giving a progressively longer volume doubling time [60]. Such curves can be fitted with a variety of mathematical models, but the most prominent one is the Gompertz model [61]. However, the empirical Gompertz model lacks a truly fundamental biological explanation.

In an attempt to obtain an analytical expression for computing the tumor volume doubling time, I used a first order, autonomous differential equation to model the tumor growth

$$\frac{dV}{dt} = \lambda V, \qquad \lambda > 0 \qquad (2)$$

where λ is the tumor growth rate constant. The model is based on the fundamental biological argument that tumor growth results from exponential cell proliferation. If, for example, each healthy tumor cell divides to produce two proliferative daughters, then the growth of the tumor cell population is: 1, 2, 4, 8, ... 2^n, an exponential function, $i.e.$, the population size will increase exponentially with time. This model describes unrestricted

tumor growth as the time goes to infinity, a phenomenon not supported by experimental data. However, for a reasonable period of growth, it gives excellent description of tumor growth curves. Most importantly, we can derive an analytical expression for computing the tumor volume doubling time from this model.

The solution of Equation (2) is an exponential function: $V = V_0 \cdot \exp(\lambda t)$ or $V = V_0 \cdot \exp(t/\tau)$, where $V_0 (cm^3)$ is the initial tumor volume at time $t = 0$ (day) and τ (day) is the time constant of the exponential growth curve. A very important property of exponential tumor growth is that the tumor volume doubling time (VDT) is a constant. Thus, when time increases by one VDT, the tumor volume will be doubled. Mathematically, this is written as

$$2V = V_0 \cdot \exp(\frac{t+VDT}{\tau}) \tag{3}$$

Dividing Equation (3) by $V = V_0 \cdot \exp(t/\tau)$ gives

$$\frac{2V}{V} = \frac{V_0 \cdot \exp(\frac{t+VDT}{\tau})}{V_0 \cdot \exp(\frac{t}{\tau})} \quad \Rightarrow \quad 2 = \exp(\frac{VDT}{\tau}) \tag{4}$$

Taking natural log on both sides of Equation (4) gives an equation for computing VDT

$$VDT = \tau \ln 2 \tag{5}$$

where τ is obtained by fitting the experimental tumor data to $V = V_0 \cdot \exp(t/\tau)$.

Figure 1 shows the growth curve of a representative mammary adenocarcinoma 13762NF. This particular tumor had a "silent interval" of about 10 days. When its growth was detected, the tumor volume increased exponentially with time ($R = 0.954$) over a fairly long period of time as seen in Figure 1, indicating that the assumption for the exponential growth model was correct. The volume doubling time (VDT) as determined by Equation (5) was approximately 5.2 days. A few points worth mentioning here. First of all, the long silent phase of undetected growth was not included in the plot. If it were to be included, the entire curve would shift 10 days to the right and the shape of the exponential part of the growth curve would not changed at all. This would not, in any way, affect the result of VDT computation as the volume doubling time is a kinetic parameter used to describe the accelerating phase or, in most cases, the exponential phase of a tumor growth. Secondly, in measuring the tumor dimensions, especially when

tumors were small, the skin thickness was subtracted from the measured dimensions. Last, the *VDT*s were computed solely based on the data obtained from intact tumors. During their late growth stage, some tumors might bleed due to a variety of reasons. When this happened, the data gathered after this point were not included in the final computation of *VDT*s.
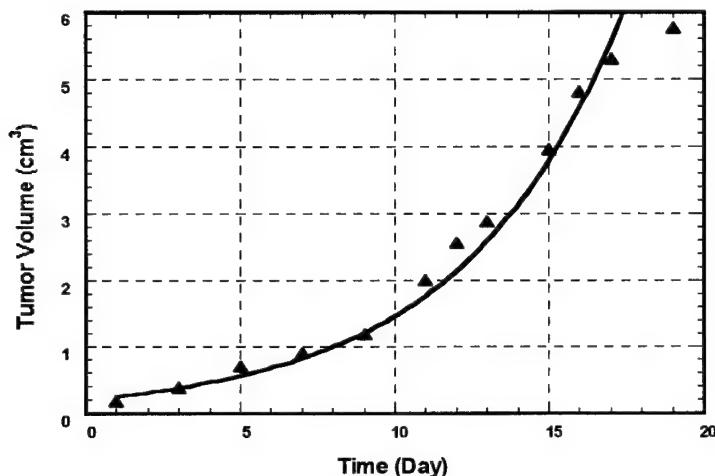

Figure 1. Tumor volume of a representative 13762NF breast tumor as a function of time after implantation. The tumor volume was computed using an ellipsoidal model: $V = (\pi/6)abc$. An excellent curve fit ($R = 0.954$) was obtained using an exponential growth model.

Table 1. A summary of tumor volume doubling time for a group of six 13762NF breast tumors.

Tumor No.	*VDT* (Day)
1	3.2
2	4.0
3	3.3
4	3.6
5	5.2
6	4.4
Mean *VDT* (Day)	**3.95 ± 0.76**

Tumor Histology

Conventional tumor histology was performed to gather information regarding tumor size, gross morphology, presence and extension of tumor necrosis, histological type and grade. Randomly chosen tumors were sacrificed by tail injection of a lethal dose of KCl. Immediately following the death of the rats, the tumors were excised and fixed in

10% neutral buffered formalin. The tumors were subsequently processed through graded ethanols and xylene, and embedded in paraffin. After embedding, sections were cut at 5μm thickness and routine hematoxylin and eosin (H&E) staining performed according to established protocols. Selected central and peripheral regions of the stained histological sections were photomicrographed using brightfield optics with a magnification of ten. Figure 2 shows histological sections of a representative 13762NF breast tumor.
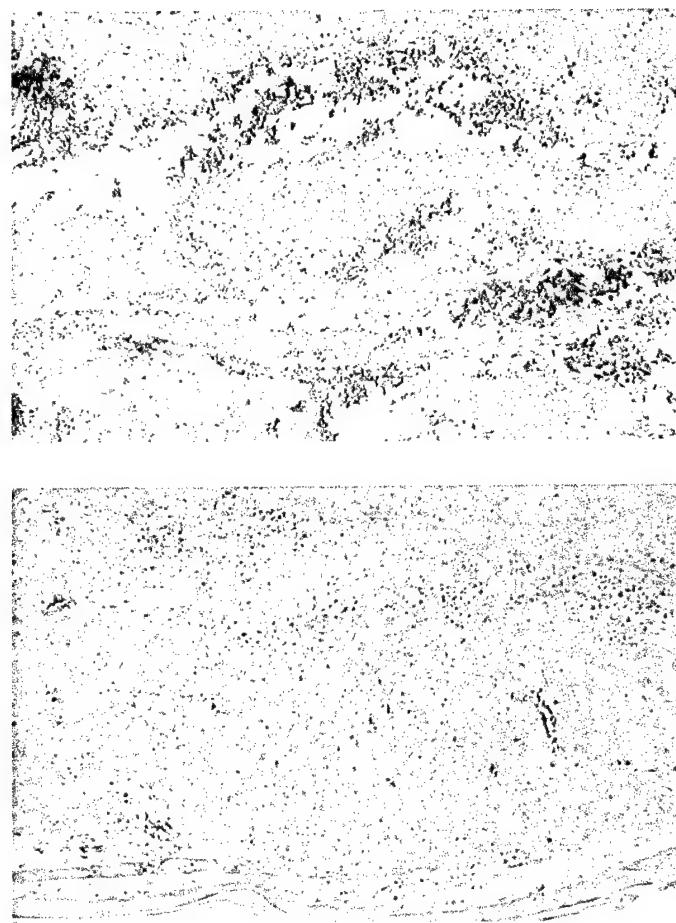
Figure 2. Histological sections of a representative 13762NF breast tumor: central (top) and peripheral (bottom) regions of the tumor.

3) Design and Construction of MRI RF Resonators

This project involved ^{19}F and ^{1}H MR imaging with living rats in a single experiment, so it was highly desirable to be able to change the resonant frequency without retuning the resonator and disturbing the animal. The desired imaging and spectroscopy resonator for our purposes would be the one that provides the highest

possible signal-to-noise ratio (**SNR**), a good filling factor, a high Q factor, minimum resistance losses, and a highly homogeneous B_1 field. To address these issues, I designed, constructed, and tested two RF resonators, one being a double-tuned birdcage resonator (^{1}H/^{19}F) and another one a swithable slotted tube resonator.

Double-Tuned (^{1}H-^{19}F) Birdcage Resonator

A birdcage resonator consists of a set of N (2, 4, 8, 16, etc.) copper wires or sheets arranged axially on the surface of a plastic cylinder and connected by high quality RF capacitors at each end. In this configuration, the effective current density in the wires or sheets varies in proportion to $cos(\phi)$, where ϕ is the azimuthal angle in cylindrical coordinates [62], and there exist several possible modes of resonance, two of which have the desired sinusoidal dependence of current on ϕ [63].

- **Design Theory**

Assuming perfectly conducting copper sheets, Figure 3 shows part of the simplified circuit model of a birdcage resonator with 16 identical legs (copper sheets), where L_i is the self inductance of the ith copper sheet and C_i is the capacitor connected between the ith and the $(i+1)$th copper sheet. The self inductance of the short copper sheet used to connect the capacitors at the ends is neglected. This is based on the fact that the electric current in the resonator is longitudinal (along the copper sheet) and maximal at the ends of the resonator.
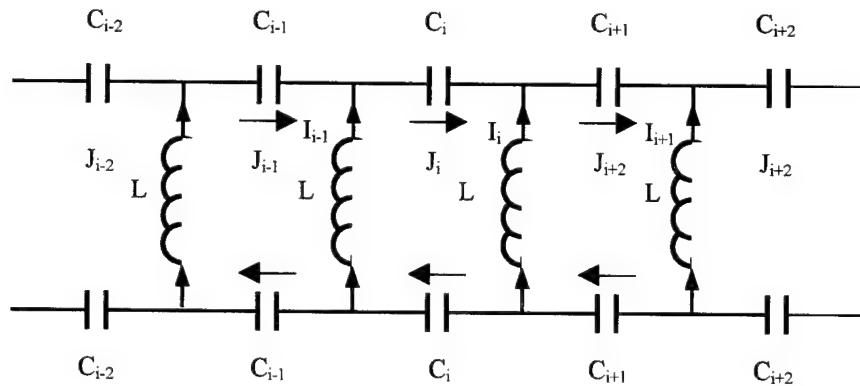

Figure 3. Part of the equivalent circuit for the high-pass double-tuned whole body birdcage resonator.

By applying Kirchhoff's Law to the ith loop made up of ith and $(i+1)$th copper sheets and ith capacitor C_i and using the complex number notation for AC current and impedance, we can get a linear system of equations:

$$\sum_k i\omega M_{i,k} I_k - \sum_k i\omega M_{i+1,k} I_k - \frac{2i}{\omega C_i} J_i = 0 \qquad (6)$$

where $M_{i,k}$ is the mutual inductance between the ith and kth copper sheets, J_i is the current in the ith capacitor, I_k is the current in the kth copper sheet, i is the imaginary number, and the summation is carried out over all possible values of index k from 0 to N − 1.

There are many ways of solving Equation (6), either analytically or numerically. The solution will represent the various resonant modes of operation of the resonator. This circuit model is a simplified one and does not take into account the complications that exist in any real implementation, such as the self-inductance of the capacitors and the inductance of the end rings. Nevertheless, the general form of the model is not altered by these factors, and the qualitative description is still valid.

- **Computer Simulation**

Instead of solving the above-described complex equation, I simulated this circuit model on a PC computer using P-Spice [64]. The desired resonant frequencies are 188.22 MHz for ^{19}F and 200.16 MHz for ^{1}H in a 4.7 T magnet. The inductance produced by the end rings was neglected in this simulation circuit, since it only accounts for ∼ 5% of the total inductance. However, the circuit model is adequate for analyzing the essential frequency characteristics of the resonator. The first step in simulating this problem was to estimate the inductance of the copper sheets, which is given by [63].

$$L = 2h[\ \ln(2h/b) + 1/2\ ] \qquad (7)$$

where L is the inductance in nanoHenries, h is the height in centimeters, and b is the width in centimeters. The copper sheets have a height of 16.5 cm and a width of 1.0 cm, with a thickness of ∼ 0.2 mm. The calculated value of the inductance based on Equation (7) was 113 nH.

The second step was to substitute this value into the simulation circuit, apply an AC current source to the circuit, vary the value of each of the 32 capacitors, and observe the amplitudes of output voltages and resonant frequencies of the circuit until two sharp resonant peaks (188.22 MHz for ^{19}F and 200.16 MHz for ^{1}H in a 4.7 T magnet) with the maximum output voltages were achieved. The capacitance values for the end ring capacitors obtained from the P-Spice simulation are tabulated in Table 1. Theoretically speaking, all the capacitance values should be equal for a single-tuned resonator and close to each other for a double-tuned resonator in order to generate a homogeneous B_1 field. The circuit model presented here is a simplified one. Therefore, the capacitance values obtained are not quite close to each other. The simulation study indicates that C10,

C26, C11, C27, C12, and C28 are relatively insensitive to ^{19}F resonant frequency, thus, they could be connected to the ^{1}H tuning circuit. I chose to place the tuning circuit in parallel to C10 since this placement provides both the best tuning for ^{1}H mode and also stabilizes the ^{19}F mode.

Table 1 Capacitance values determined by P-Spice simulation (unit: pF)

C1	C2	C3	C4	C5	C6	C7	C8
40	130	130	130	120	115	108	115
C9	**C10**	**C11**	**C12**	**C13**	**C14**	**C15**	**C16**
42	159	185	120	120	102	90	90
C17	**C18**	**C19**	**C20**	**C21**	**C22**	**C23**	**C24**
40	130	130	130	120	115	108	106
C25	**C26**	**C27**	**C28**	**C29**	**C30**	**C31**	**C32**
42	159	185	120	120	102	90	90

Fine tuning of ^{19}F mode is achieved by connecting another capacitor CF19T in parallel with C6. When ^{19}F tuning capacitor CF19T varies from 0 pF to 2000 pF, ^{19}F resonant peak varies from (188.224 MH$_z$, 14.727 V) to (184.871 MH$_z$, 16.606 V) while ^{1}H resonant peak changes only from (200.435 MH$_z$, 13.905 V) to (200.535 MHz, 13.602 V), which is a clear indication that each mode is independently tuned.

- **Construction**

    A 16-leg high-pass double-tuned birdcage resonator was constructed according to the design principles and the simulation results described above. The resonator is tunable to both 188.2 MH$_z$ and 200.1 MH$_z$ for operation at ^{19}F and ^{1}H frequencies on a 4.7 T magnet. The cylindrical resonator body is 24.60 cm in length and has an outer diameter of 24.00 cm. The outer structure of the resonator is made of a 5 mm thick plexiglass cylinder, which provides mechanical support and structural stability for the resonator. A 0.2 mm thick copper sheet shield, connected to the ground, is mounted on the inner wall of the outer plexiglass cylinder.

    The critical part of the resonator is its inner structure. The inner structure, made from a 5 mm thick plexiglass cylinder, has an outer diameter of 10.50 cm. On the inner wall of the plexiglass cylinder are mounted directly 16 copper sheets (legs) with 1.5 mm gaps and 32 capacitors. The size of the uniform region of B_1 magnetic field generated by the resonator is directly related to the number of legs. The more numerous the legs, the more uniform the B_1 magnetic field in the radial direction. I chose to build a birdcage resonator with sixteen legs because the B_1 magnetic field generated should, in principle,

be uniform enough for my applications and should produce strong NMR signal. The legs are made from 0.1 mm thick copper foil. Each of the sixteen legs is 16.5 cm in length, 1.0 cm in width in the central part and 1.5 cm in width at the two ends (Figure 4).
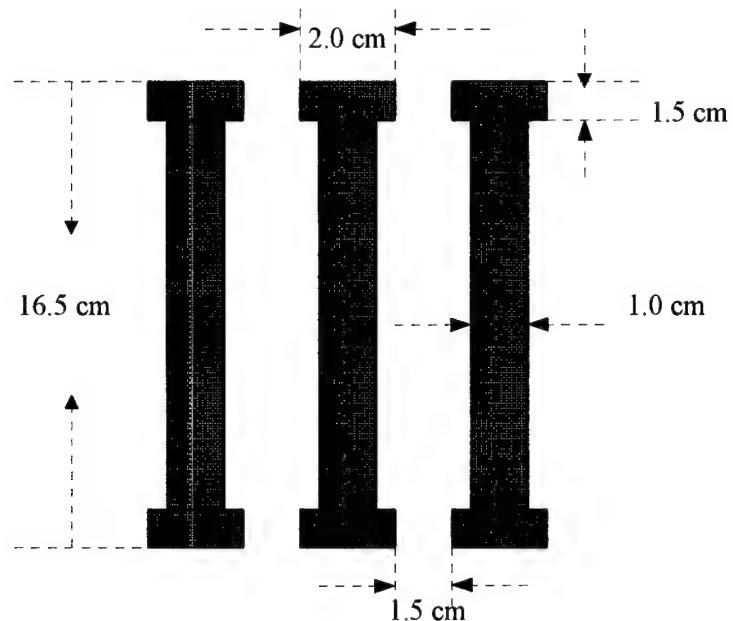

Figure 4. Geometry of the legs (copper sheets).

The structure of the two end rings, *i.e.*, the two circular bands at the ends of the resonator, consisted of capacitors and was made identical to achieve electrical balance so that the loading effects of the sample could be reduced. The resonator is double-tuned, and is driven between equivalent points on the two rings halfway between two adjacent parallel legs. The resonator was tuned by individually adjusting the CF19T and CH1T at each of the resonant frequencies. The capacitively coupled tuning loops were placed between legs 11 and 13 and legs 19 and 21. These loops were connected by standard coaxial cables to the external tuning capacitors CF19T and CH1T that allowed each resonant mode to be independently tuned. Special care was taken to ensure that there was little tuning interaction between the two resonant frequencies as possible. The resonator was matched capacitively through a variable capacitor C_{match}.

• **Bench Testing**

The laboratory bench testing was carried out using a frequency analyzer (HP8752A). To test the resonator's performance, it was essential to have a set of standard samples that simulated the type of *in vivo* samples used in the magnet. Two NMR

phantoms were prepared for this purpose, which roughly had the same loading effects (lowering Q and shifting resonant frequencies) as a male adult rat (~ 250 g). A 444 ml phantom was made of an NMR compatible plastic bottle filled with a solution of saline and trifluoroacetic acid (TFA, 5% v/v). A smaller 250 ml phantom, also made of an NMR compatible plastic bottle, was filled with a solution of TFA (5% V/V) and $CuSO_4$ (1 g/liter) in distilled water. The major chemical components and their concentrations of the phantoms are listed in Table 2.

Table 2. Major chemical components and their concentrations of the saline phantoms.

CHEMICAL NAME	CONCENTRATION (g/l)
NaCl	6.90
KCl	0.375
$MgSO_4$	0.145
$CaCl_2$	0.185
Na_2HCO_3	2.10
Glucose	1.80

The resonator's resonant frequencies, unloaded and loaded Q values (quality factors) and Q damping for each of the resonant modes as measured by the frequency analyzer are presented in Table 3. Q_0 is the unloaded Q value measured with the resonator in air (without the phantom), while Q_L is the Q value measured when the saline phantom was placed centrally inside the resonator. The Q damping is defined as the ratio of Q_0/Q_L. The results are the means of three measurements. The loaded Q values are affected by the dimensions of the phantom and its position in the resonator. In general, the loaded Q values are dominated by the effect of the RF lossy sample. The Q values decrease as the dimensions of the sample increases.

Table 3. Results of the laboratory bench testing of the birdcage resonator. Q_0 and Q_L were measured with the 444 ml phantom.

Resonant Mode	Resonant Frequency (MHz)	Unloaded Q_0	Loaded Q_L	Q_0/Q_L
^{19}F	188.22	14	9	1.56
^1H	200.16	13	8	1.63

It can be seen from Table 3 that the unloaded Q_0, loaded Q_L, and the Q damping Q_0 /Q_L for both resonant modes are similar. The relatively low Q values may be attributed to the relatively long coaxial cables used to connect the tuning and match circuits. Another possible reason could be the large size of the resonator because the longer the legs, the larger their resistance, causing increased resistance losses and significantly lowering Q values. One of the consequences of the low Q values on the NMR experiments would be to increase the 90^0 pulse width for a given RF power level. This can be verified by the following equation [64]:

$$ PW = K \left(\frac{V_R}{Q} \right)^{\frac{1}{2}} \tag{8} $$

where PW is the 90^0 pulse width, V_R is the resonator volume, Q is the quality factor of the resonator, and the factor K is roughly a constant for all resonator designs. This equation indicates that the 90^0 pulse width is linearly proportional to the square root of resonator' volume and inversely proportional to the square root of resonator's Q value.

- **Phantom Imaging**

The double-tuned birdcage resonator's NMR performance was tested on the Omega CSI 4.7 T magnet, which operates at a proton frequency of 200.106 MH$_z$ and a fluorine frequency of 188.273 MH$_z$. The phantom was centered in the resonator and the resonator was positioned in the isocenter of the magnet, with its axis being aligned with the direction of the magnet's static magnetic field B_0. The 90^0 pulse widths were determined from a 180^0 null of the whole sample. Typical 90^0 pulse widths were 700 µs for proton and 350 µs for fluorine. Shimming was accomplished on the water proton FID of the saline solution in the phantom, with the resonator tuned to the double resonant modes. The goal was to obtain a B_0 of homogeneous strength over the entire imaging sample volume. Fourteen shim currents were adjusted on the proton FID throught the system automated shimming utility until a symmetrical and long FID was obtained. The proton spectral linewidth at half height after shimming was 34 Hz, which was sufficient for imaging experiments.

To minimize acquisition time, a driven equilibrium spin-echo pulse sequence with a fairly short echo time (TE = 8ms) was employed so that the T_2 dephasing effects were not significant. Proton transaxial (transverse) images were acquired as a 3-D data set with a repetition time TR = 150 ms, echo time TE = 8 ms, and a 128 x 64 x 8 matrix size over 100 mm x 100 mm field of view (FOV), providing 0.78 mm x 1.56 mm x 25 mm digital resolution. To improve signal-to-noise ratio (SNR), two acquisitions were averaged for each image, thus, giving a total acquisition time of 2 min 33 sec. Proton coronal and sagittal images were also acquired with the same imaging parameters.

SNRs for the images with 2 averages were measured using a standard routine. The values for signal were measured from a randomly chosen portion of images by a square crop and the values for noise were taken from the four corners of the image background. For each measurement, the square crop covered a reasonably large area of the image or background, so that the data obtained were unbiased. The results of SNR measurements for the proton images are listed in Table 4. The resonator's B_1 field homogeneity was estimated by visual inspection of the images.

Table 4. Results of SNR measurements for the proton images.

	Upper-Left SNR	Upper-Right SNR	Lower-Left SNR	Lower-Right SNR	Mean SNR	SD
Transaxial Section	88.0	97.4	93.0	93.3	92.9	3.9
Sagittal Section	279.8	272.7	278.7	294.0	281.3	9.0
Coronal Section	287.5	114.3	267.7	125.8	198.8	91.4

The magnet frequency was then set on resonance for the CF_3 group of TFA, without retuning the resonator. The 90^0 pulse was 360 ms. The ^{19}F spin-echo images were acquired as transaxial, saggital and coronal projections. The images were fluorine density-weighted with TR = 150 ms and TE = 8 ms and were averaged 16 times to achieve an acceptable SNR. Thus, each image was acquired in 2 min 33 sec. The image matrix size was 128 x 64 with a field of view of 100 x 100 mm for the tranaxial projection and 200 x 200 mm for the sagittal and coronal projections, respectively.

Table 5. Results of SNR measurements for the ^{19}F images.

	Upper-Left SNR	Upper-Right SNR	Lower-Left SNR	Lower-Right SNR	Mean SNR	SD
Transaxial Section	3.2	3.3	3.4	3.5	3.3	0.1
Sagittal Section	5.9	6.7	7.3	6.9	6.7	0.6
Coronal Section	4.3	4.5	3.8	3.7	4.1	0.4

The image SNRs were measured in the same way as the proton images and the results are presented in Table 5. The spin-lattice relaxation time T1 of the CF_3 group was estimated by applying a non-spatially selective inversion recovery (IR) RF pulse. Seven different IR delays (τ) increasing in the range between 800 ms to 20 sec were used (Table

6). The T1 value was calculated based on the Levenberg-Marquardt three-parameter fitting algorithm [65] on peak intensity values (Table 6).

Table 6. Results of T1 measurement for TFA solution and delay list (τ) of the inversion recovery pulse sequence.

Function: $y = A*(1-(W+1)*exp(-\tau/T1)$

$A = 1.92e+06 \pm 26484$

$W = 0.026 \pm 0.042$

$T1 = 2.3 \pm 0.19$

Standard Error = 41129.6

Y Standard Deviation = 31091.1

τ	Intensity	Calculated	Difference	SD
20.000	1923050.524	1923610.434	559.911	0.018
16.000	1932423.278	1921888.260	-10535.018	-0.339
8.000	1857983.273	1859578.430	1595.157	0.051
4.000	1534324.010	1567419.792	33095.782	1.064
2.000	1135584.863	1085041.321	-50543.542	-1.626
1.000	587685.972	637132.244	49446.272	1.590
0.800	545796.816	522178.645	-23618.170	-0.760

Slotted Tube Resonator

The slotted-tube resonator was originally developed to efficiently provide ^{1}H decoupling to samples in high-field magnets [66]. The common slotted tube resonator consists of a conducting tube with two slots cut symmetrically along both sides of the tube. The surface current distribution produced by the slotted tube resonator peaks near the edges of the conducting tube adjacent to the slots. The conducting tube of the slotted tube resonator is opaque to RF field and diverts all the B_1 field flux through the two slots. Thus, the aperture angle of the slots must be optimized in order for the resonator to generate a homogeneous field. The fundamental feature of the slotted tube resonator is that the conducting component has a low inductance, and hence, large volume resonators can be constructed. At the RF frequencies encountered in clinical MRI systems, this means that the slotted tube resonators can be designed to contain samples of size comparable to that of the human head. The major applications of the slotted tube resonator are for imaging and for localized spectroscopy techniques demanding a uniform flip angle over the entire sample.

- **Design Theory**

The circuit model is illustrated in Figure 5. L_s and R_s are sample inductance and resistance, respectively. This circuit model can be further simplified in terms of equivalent circuit (Figure 6) with

$$Z'_2 = \frac{i(L_3 C_3 \omega^2 - 1)}{\omega(C_3 - C_2(L_3 C_3 \omega^2 - 1))} \tag{9}$$

where ω is the resonant frequency of the circuit and i is the imaginary number. Thus, the tuning impedance Z_T is given by the following expression:

$$Z_T = Z_1 + Z'_2 = \frac{-i}{C_1\omega} + Z'_2$$
$$= i\frac{C_1(l_3 C_3 \omega^2 - 1) - \omega(C_3 - C_2(L_3 C_3 \omega^2 - 1))}{\omega C_1(C_3 - C_2(L_3 C_3 C^2 - 1))} \tag{10}$$
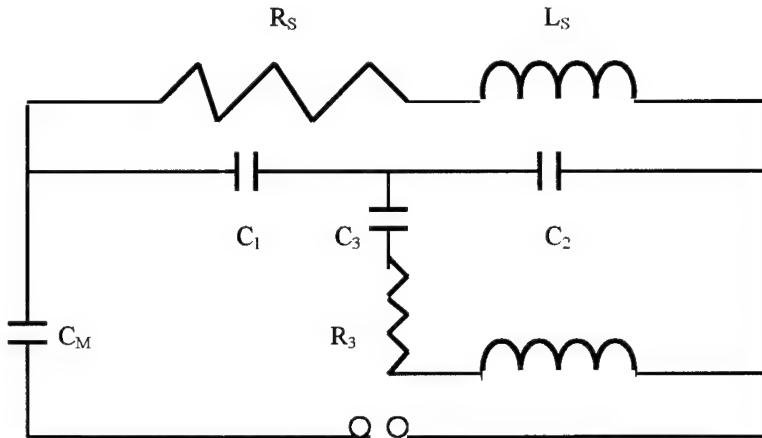
Figure 5. The circuit model of the switchable slotted tube resonator. R_s is the sample resistance and L_s the sample inductance. R_3 is the equivalent resistance of the tuning loop.

When the resonator operates at the higher frequency $\omega = \omega_h$, the tuning impedance Z_T is a function of the total capacitance of the tuning circuit and is given by the expression

$$Z_T = -i\frac{(C_1 + C'_2)}{\omega_h C_1 C'_2} \tag{11}$$

where

$$C'_2 = \frac{C_2(L_3C_3\omega_h^2 - 1) - C_3}{L_3C_3\omega_h^2 - 1} \qquad (12)$$

Thus, the tuning is achieved by adjusting all the capacitors. When the resonator operates at the lower frequency $\omega = \omega_l$, the series L_3C_3 circuit has a zero impedance and the total tuning impedance is reduced to

$$Z_T = -\frac{i}{C_1\omega_1} \qquad (13)$$

Thus, tuning is obtained by adjusting C_1 only.
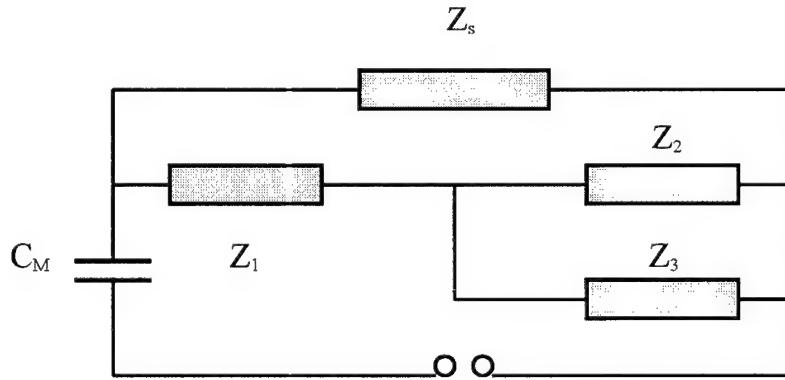
Figure 6. Equivalent circuit model of the slotted tube resonator.

- **Construction**

A switchable slotted tube resonator was constructed based on the above design theory using two copper sheets, which cover an 80^0 arc [67] for optimal B_1 field homogeneity. The cylindrical resonator body is 23.5 cm long with outer diameter 25.4 cm. The outer structure of the resonator is made of a 5mm thick plexiglass cylinder. The inner structure is made of a 3 mm thick plexiglass cylinder, having a small outer diameter of 7.6 cm to increase the filling factor and reduce the pulse width. The two ends of the resonator are covered by two 6 mm thick plexiglass boards stabilized by 6 nonmagnetic screws on each end, respectively. The two boards, along with the outer structure, provide very stable mechanical support for the resonator. Three capacitors of 20.0 pF were positioned symmetrically between the guard rings and the copper sheets to obtain uniform surface current distribution.

The resonator has a usable length of 15.5 cm, sufficient for *in vivo* adult rat NMR experiments. The two guard rings and two copper sheets are made from 0.3 mm thick copper foil. The width of each of the guard rings is 1.0 cm and there is a spacing of

approximately 0.5 cm between the guard ring and the vertical copper sheets, which are joined with capacitors. The copper sheets have a length of 12.5 cm and their width covers about 80^0. The resonator is tunable to ^{19}F (188.22 MHz) and ^1H (200.16 MHz), and is driven between one copper sheet and one guard ring. The tuning of the resonator was achieved by three variable capacitors C_1, C_2, and C_3, which are V2145H family high Q RF capacitors (Voltronics Corporation, Denville, New Jersey). C_1 and C_2 (NMTM38GE) have a capacitance range of 1.0 ~ 38.0 pF, C_3 (NMTM120CE) has a capacitance range of 2.0 ~ 120.0 pF, and C_M (NMQM22GE) has a capacitance range of 1.0 ~ 22.0 pF. ^{19}F resonance was obtained by adjusting C_1 and ^1H resonance was achieved by adjusting C_1, C_2, and C_3, respectively. The resonator was matched capacitively through C_M.

- **Bench Testing**

The resonator was tuned and matched on the laboratory bench with the help of a frequency analyzer (HP8752A). The resonant frequencies, unloaded Q_0 and loaded Q_L values and Q damping for each of the resonant modes are presented in Table 7. Q_0 is the unloaded Q value measured with the resonator in air, while Q_L is the Q value measured when the phantom was placed centrally inside the resonator. The Q damping is defined as the ratio of Q_0 / Q_L. The results are the means of three measurements.

Table 7. Results of the laboratory bench testing of the slotted tube resonator. Q_0 and Q_L were measured with the 250 ml phantom.

Resonant Mode	Resonant Frequency (MHz)	Unloaded Q_0	Loaded Q_L	Q_0 / Q_L
^{19}F	188.22	97.5	54.2	1.80
^1H	200.16	63.8	53.6	1.19

As can be seen from Table 7, the unloaded Q_0 for ^{19}F is much higher than that for ^1H, and the loaded Q_L for both resonant frequencies is essentially same. The Q damping, Q_0 / Q_L, for ^{19}F is 1.5 times higher than that for ^1H. This means that the RF lossy phantom has a much stronger effect on the ^{19}F resonance than on the ^1H resonance. The high Q values could be the result of several factors, including a relatively small usable volume, minimized length of connecting wires, and a structure without a copper shield. The high Q values guarantee that the resonator has a higher excitation efficiency, *i.e.*, the 90^0 pulse width for a given RF power level is short or the magnitude of the B_1 field generated with a given RF power level is high. The results of the laboratory bench testing also indicated that the resonator was easy to tune and match and both resonant frequencies were stable and immune to external electromagnetic interference.

- **Phantom Imaging**

    Once again, the NMR performance of the slotted tube resonator was tested on the Omega CSI 4.7 T magnet. The *in vitro* resonator sensitivity for proton and fluorine was determined using the 250 ml phantom, which was filled with a solution of TFA (5%v/v) and $CuSO_4$ (1g/liter) in distilled water. Measurements of 90^0 pulse width were performed from a 180^0 null of the whole sample. Typical 90^0 pulse widths were around 170 µs for proton and 110 µs for fluorine. Shimming was performed on the water proton FID of the saline solution with resonator tuned to the ^1H resonance, to a typical spectral linewidth of 32 Hz. The driven equilibrium spin-echo pulse sequence was used for the imaging experiment. Imaging parameters were: TR= 150ms, TE = 8ms, and matrix size =128 x 64 x 8. The field of view (FOV) was 80 mm x 80 mm for transaxial images, 100 mm x 100 mm for coronal, and 200 mm x 200 mm for sagittal images. The images were acquired with one excitation, thus giving a total acquisition time of 1.16 min. The image signal-to-noise ratios (SNRs) were measured as described before. The results of SNR measurements for the proton images are listed in Table 8.

Table 8. Results of SNR measurements for the proton images.

	Upper-Left SNR	Upper-Right SNR	Lower-Left SNR	Lower-Right SNR	Mean SNR	SD
Transaxial Section	389.3	199.5	897.8	666.3	538.2	177.1
Sagittal Section	494.2	517.5	478.8	450.5	485.3	28.1
Coronal Section	190.3	30.2	164.6	22.8	102.0	87.9

Following the ^1H imaging experiment, the resonator was retuned in place to 188.27 MHz and corresponding ^{19}F imaging experiment was carried out. The 90^0 pulse was 108 µs and the spectral linewidth after shimming was 46 Hz. The spin-echo (SE) images were acquired with the imaging parameters: TR = 150 ms, TE = 8 ms, FOV = 100 x 100 mm, NA = 16, and matrix size = 64 x 32. The image SNR measurements were performed in the same way as the proton images and the results are given in Table 9.

Table 9. Results of SNR measurements for the fluorine images.

	Upper-Left SNR	Upper-Right SNR	Lower-Left SNR	Lower-Right SNR	Mean SNR	SD
Transaxial Section	3.1	2.9	2.6	3.0	2.9	0.2
Sagittal Section	4.2	5.1	4.0	4.2	4.4	0.5
Coronal Section	4.2	4.3	4.7	4.6	4.5	0.2

4) Assessment of Hexafluorobenzene (HFB) Distribution
Animal Preparation

Once the tumors reached ~1 cm diameter (~ 0.5 cm^3), corresponding to a typical lower limit of tumor detected in patients, the rats were anesthetized with 200 μl ketamine hydrochloride i.p. (100 mg/ml; Aveco, Fort Dodge, IA) and were maintained under general gaseous anesthesia using a small animal anesthesia unit with air (1.0 dm^3/min) and 1.0% isoflurane (Ohmeda PPD Inc., Fort Dodge, IA). Tumor hair was cut with a pair of surgical scissors for reduction of the NIR light scattering and ease of HFB injection. The rats were placed on their sides in a specially designed NMR bed. The body temperature was maintained at about 37°C by a warm water blanket with a feedback system (K-MOD 100, Baxter Healthcare Co., Deerfield, IL). A fiber optic pulse oximeter (Nonin Medical, Inc., Plymouth, MN) was placed on the hind foot to monitor arterial hemoglobin saturation (s_aO_2) and heart rate (HR), and a thermocouple (Cole-Parmer Instrument Co., Vernon Hills, IL) was inserted rectally to monitor core temperature. 40 μl HFB (99.9%, Aldrich Chemical Co., St. Louis, MO) was injected directly into selected areas of tumor central and peripheral regions at the same plane using a Hamilton syringe with a 32 G needle. The needle was inserted manually to penetrate across the whole tumor and withdrawn ~ 1 mm to reduce the tissue pressure and 2~5 μl HFB injected. The needle was repeatedly withdrawn at a step size 1~2 mm and further HFB injected. A total of 2 ~ 3 tracks of HFB was injected in the form of a fan.
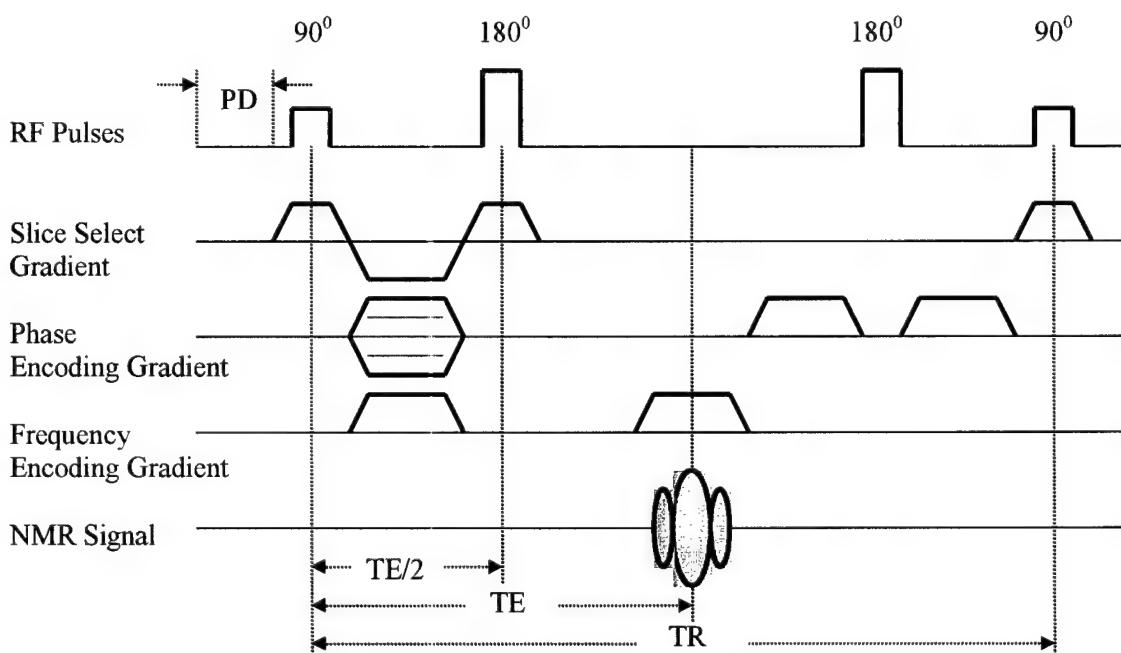

Figure 7. Pulse diagram of the driven equilibrium spin-echo pulse sequence

^{1}H Magnetic Resonance Imaging

For each tumor, high resolution 3-D ^{1}H MR imaging was first performed for anatomical reference. A frequency switchable (^{1}H/^{19}F) RF coil was placed around the tumor with the tumor centered in the coil. The rat was then be placed on its side in the bed and positioned in the isocenter of the magnet, with the coil axis being aligned perpendicular to the direction of the magnet's static magnetic field B_0. The 90^0 pulse width was determined from a 180^0 null of the whole tumor. Shimming was performed on the tumor tissue water proton FID to a typical linewidth of 70 Hz. This was accomplished by adjusting fourteen shim currents on the FID through the system automated shimming utility until a symmetrical and long FID was obtained. The goal was to obtain a B_0 of homogeneous strength over the entire tumor.

Table 10. ^{1}H imaging parameters

| Repetition Time (TR)	1500 ms
Echo Time (TE)	80 ms
Matrix Size	128x64x8
Field of View (FOV)	20x20x20 mm
Digital Resolution	156 μm x 312 μm x 2.5 mm
Number of Acquisitions (NA)	2
Total Acquisition Time	25 min 36 sec

To minimize acquisition time, the driven-equilibrium spin-echo pulse sequence with a short echo time (TE = 80 ms) (Figure 7) was used so that the T_2 dephasing effects was not significant. ^{1}H images were acquired as a 3-D date set. Imaging parameters used are shown in Table 10. These T2-weighted images showed the tumor anatomy and its position relative to the back of the rat. Following the ^{1}H imaging, the corresponding ^{19}F imaging was then performed to show the distribution of HFB in the tumor.

^{19}F MRI and Assessment of HFB Distribution

The magnet frequency was then set on resonance for the CF group of HFB and the coil was retuned in place to 188.273 MHz. Corresponding fluorine density-weighted images was acquired as a 3-D data set using the driven-equilibrium spin-echo pulse sequence. The imaging parameters are shown in Table 11. Gradients were compensated to account for the difference in gyromagnetic ratios. Data were processed using sine-bell apodization to improve SNR and zero-filling in the first phase encoding direction for the execution of fast Fourier transform (FFT). Images were transferred to a PC and further processed off line using a SCION imaging software. Figure 8 shows conventional SE ^{1}H

images (top four) and corresponding ^{19}F SE images of a representative breast tumor. Comparison of the ^{1}H and ^{19}F images reveals that the tumor was centrally labeled in this case.

Table 11. ^{19}F imaging parameters

Repetition Time (**TR**)	150 ms
Echo Time (**TE**)	8 ms
Matrix Size	128x64x8
Field of View (**FOV**)	20x20x20 mm
Digital Resolution	156 μm x 312 μm x 2.5 mm
Number of Acquisitions (**NA**)	8
Total Acquisition Time	10 min 15 sec
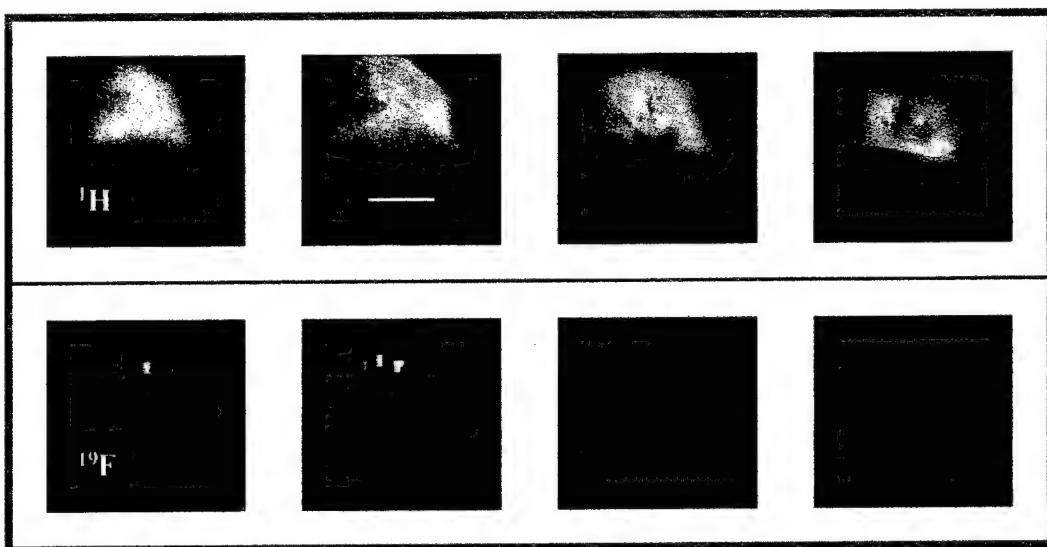
Figure 8. ^{1}H and ^{19}F coronal images of a representative breast tumor. Bar represents 1 cm.

Determination of HFB Redistribution and Clearance

In contrast to traditional perfluorocarbons (PFCs), which exhibit excessive tissue retention, HFB clears from tissue relatively rapidly. To verify that HFB global clearance was not so rapid as to interfere with relaxometry, ^{19}F NMR spectroscopy was performed

interleaved between ^{19}F EPI relaxometry. HFB spectroscopic signal intensity was compared with a benzene-doped standard. In addition, [19]F 3-D MRI was also repeated to determine the global and regional clearance of HFB and to assess any redistribution of signal intensity within the tumor. To compute HFB clearance time (biological halflife), a single parameter exponential decay model was used:

$$Q(t) = Q(0)\exp(-\frac{t}{T})$$ (14)

where $Q(t)$ was the signal intensity at any given time t, $Q(0)$ was the signal intensity at time zero, and T was the clearance time in minute. Since HFB is a non-ionic freely diffusable tracer, clearance provides an indication of relative tumor blood flow (TBF). .
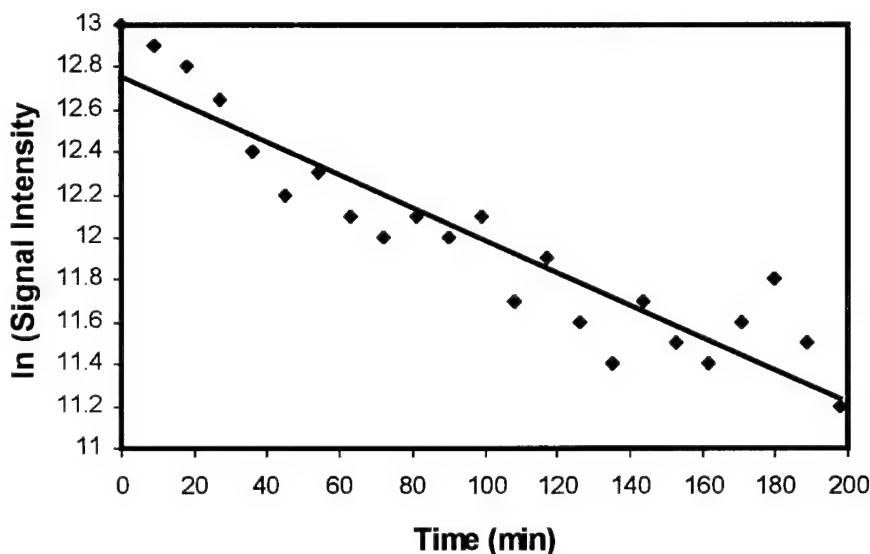
Figure 9. HFB clearance curve of a typical voxel from a 13762NF breast tumor. τ = 160 min.

Figure 9 shows the HFB clearance curve of a representative voxel from a 13762NF breast tumor during the 3 hours period of a typical experiment. For many regions, the HFB signal intensity was found to decay exponentially with a typical biological half-life ranging from $T_{1/2}$ = 700 to 1200 min. Since our ^{19}F MR EPI oximetry experiments lasted about three hours, this means the global and regional clearance and redistribution of HFB within the tumors did not interfere with ^{19}F MR EPI oximetry. By analyzing the clearance of individual voxels, it was found that as a whole ^{19}F signal intensity decreased with time, some voxels, however, showed increases in signal intensity

as shown in Figure 10. This could be due to the inflow of HFB from the surrounding voxels. Since HFB concentration only affects the SNR of ^{19}F signal intensity and does not have a direct impact on relaxation rate $R1$, this local redistribution of HFB will not compromise the quality of our tumor oxygenation studies.
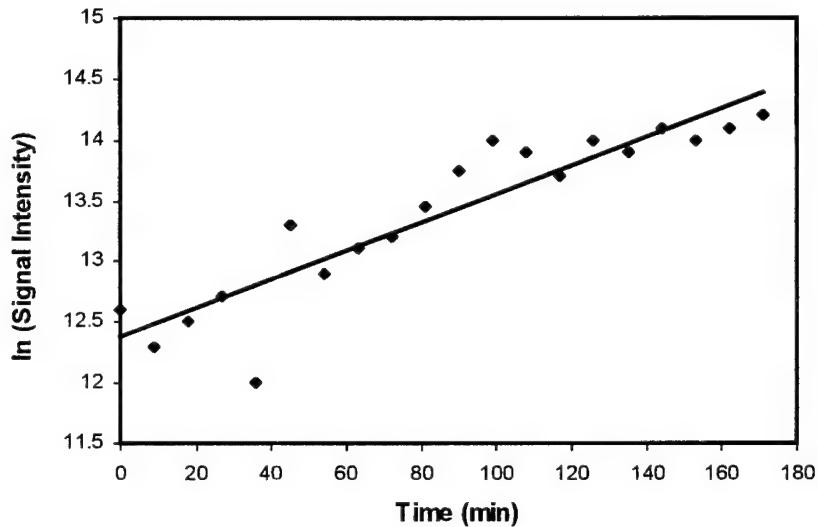

Figure 10. HFB clearance curve of a voxel from a 13762NF breast tumor that showed an increase in signal intensity with time

5) Software Development
A Computer Program to Assess the Goodness of T1 Relaxation Curve Fit

^{19}F EPI was used as a basic building block for ^{19}F MR EPI oximetry. To measure spin-lattice relaxation time (T1) and hence pO_2 maps, a pulse burst saturating (PBSR) pulse train was applied immediately prior to the EPI sequence. This led to some loss of dynamic range in the results, but substantially shortened the time required for a T1 experiment and thus, improved the temporal resolution. Fourteen data sets were acquired with delay time in a geometric progression ranging from 200 ms to 90 sec. Since the longest and shortest delays were alternated during data acquisitions to reduce systematic bias, it was necessary to restore the images to the correct order, *i.e.,* from the shortest to the longest delay (200 ms $\cdots\cdots\rightarrow$ 90 sec) prior to the curve fit

In order to obtain the spatial distribution (map) of pO_2 in breast tumors, we needed to solve for the R1 map of injected HFB first. This was done by fitting the signal intensity in each of the voxels of the fourteen images to a three parameter exponential relaxation model:

30

$$y_n(i,j) = A(i,j) \cdot [1 - (1+W) \cdot \exp(-R1(i,j) \cdot \tau_n)]$$
$$(n = 1, 2, \cdots\cdots, 14)$$
$$(i, j = 1, 2, \cdots\cdots 32)$$
(15)

by the Levenberg-Marquardt least-squares algorithm, where $y_n(i,j)$ was the measured signal intensity corresponding to delay time τ_n (the nth image) of voxel (i,j), $A(i,j)$ was the fully relaxed signal intensity amplitude of voxel (i,j), W was a dimensionless scaling factor allowing for imperfect signal conversion, and $R1(i,j)$ was the relaxation rate of voxel (i,j) in unit of $\sec^{-1}$.
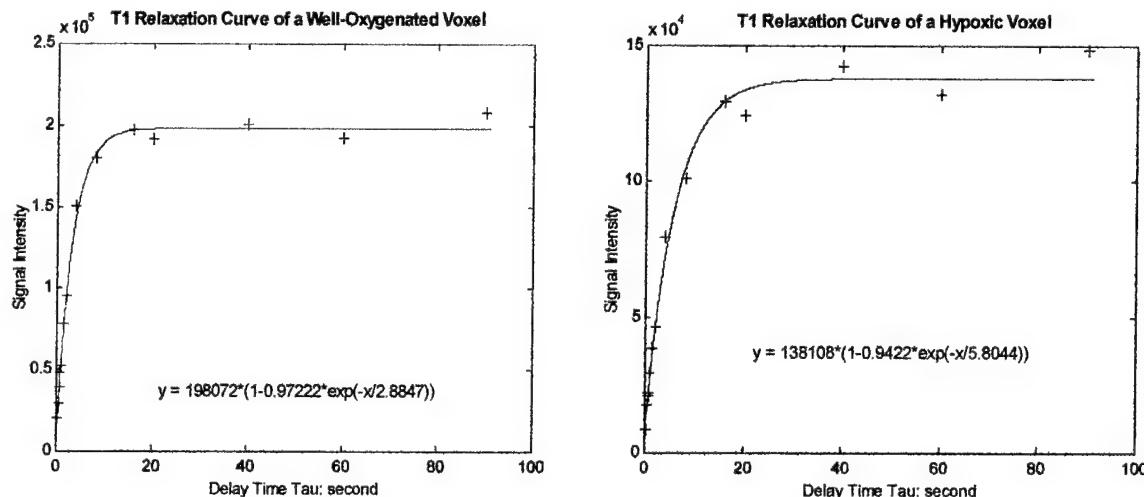
Figure 11. T1 relaxation curves of a well-oxygenated voxel (left) and a hypoxic voxel (right).

Good T1 relaxation curve fit was crucial in ^{19}F PBSR-EPI oximetry. It was relatively easy to obtain excellent curve fits, provided SNR > 10 for most intense signals. To assess the goodness of curve fit, I wrote a Unix based NMR-shell script program to display the T1 relaxation curve of individual voxels of PBSR-EPI images. The graphical representation of the data, relaxation model, and goodness of fit provided a quick and convenient way of assessing the quality of the data. Based on the rms error of fit, the goodness of curve fit could be classified into three categories: good, intermediate, and poor.

For typical good relaxation data, the global least squares minimization was achieved with a very small rms error. These data, related to strong ^{19}F signal, represented those voxels within the region of interest (ROI). For typical intermediate data, the global

least squares minimization was achieved with a relatively large rms error due to a single bad data point, which led to a big T1 error. To improve the relaxation curve fit, a threshold was applied to the raw data, which eliminated those data points $\geq 3\sigma$ from the curve. The remaining data, thus, provided a better curve fit. In applying the threshold, only one data point was eliminated from the raw data per curve. These relaxation data represented those voxels within the ROI, but had relatively strong ^{19}F signals. In general, they gave good T1 values. For poor relaxation data, the global least squares minimization either failed or converged slowly with a very large rms error. These relaxation data, associated with those voxels outside the ROI, represented either very week ^{19}F signals or background noise. They gave unreliable T1 values. Figure 11 shows T1 relaxation curves of a well-oxygenated voxel (left) and a hypoxic voxel (right).

A Computer Program to Compute HFB Clearance Rate

To compute HFB clearance rate (biological halflife), I used a single parameter exponential decay model:

$$Q_{i,j}(t) = Q_{i,j}(0)\exp(-t/T_{i,j}) \tag{16}$$

where $Q_{i,j}(t)$ was the signal intensity of voxel (i, j) at time t, $Q_{i,j}(0)$ was the signal intensity of voxel (i, j) at time zero, and $T_{i,j}$ was the clearance rate of voxel (i, j). Equation (16) was transformed into a logarithmic form:

$$\ln(Q_{i,j}(t)) = \ln(Q_{i,j}(0)) - t/T_{i,j} \tag{17}$$

Based on above theory, I wrote a program to compute the clearance rate $T_{i,j}$ of individual voxels by fitting the signal intensity of PBSR-EPI images to Equation (17). A clearance rate map was then produced by displaying $T_{i,j}$ as a color-coded image. This program is capable of determining the global and regional clearance rate of HFB.

A Computer Program to Process pO_2 Data

A windows-based Visual Basic program was written to process pO_2 data. The program can display and process images in the following formats:

- BMP   Bitmap
- GIP   Graphics Interchange Format
- JPG   Joint Photographic Experts Group
- DIB   Device Independent Bitmap
- WMF   Windows MetaFile
- EMF   Enhanced MetaFile
- ICO   Icons

More functions are being added to the program.

A Computer Program to Process NIRS Data

NIRS signal and biomedical signals in general are commonly contaminated by a number of sources. To reduce the contamination (noise), I employed digital signal processing techniques: averaging and filtering. Averaging was to improve the SNR of the signal and filtering was to remove the unwanted frequency components contained in the signal. Digital filters are mathematical algorithms implemented in hardware and/or software that operate on a digital signal to produce a desired digital output signal. I wrote a LabView^{TM} program to implement these techniques. LabView^{TM} is a graphical programming development environment based on the G-programming language for data acquisition and control, data analysis, and data presentation. It is more powerful and, at the same time, easier to learn and implement than the traditional text-based programming languages, such as C.

- **Averaging**

The first step in processing the NIRS data was averaging. Four adjacent data points were averaged to produce a new data point according to:

$$y(n) = \frac{x(n) + x(n+1) + x(n+2) + x(n+3)}{4} \tag{18}$$

where $x(n)$ represented the nth input data point and $y(n)$ the nth output data point. Since the NIRS data were acquired at relatively high sampling frequency, this averaging operation improved the SNR of the signal but not at the expense of losing detailed information in the data.

- **Digital Filtering**

Following averaging, the data were fed into a high order Butterworth low-pass filter with a cut-off frequency of 1.0 Hz. Butterworth filters are one of the infinite impulse response (IIR) filters. The main characteristics of the IIR filters is that the output depends not only on the current and past input data, but also on the past output data as shown in the following recursive equation [68]:

$$y(n) = \sum_{k=0}^{N} a_k x(n-k) - \sum_{k=1}^{M} b_k y(n-k) \tag{19}$$

where a_k are called the forward coefficients, b_k the reverse coefficients, $x(n)$ and $y(n)$ are the input and output to the filter, and N and M are the number of forward and reverse coefficients, respectively. Given the filter specifications (Table 12), a_k, b_k, N and M were computed using either a standard procedure.

The rationale for me to use a high order low-pass Butterworth filter was two-fold. Firstly, a Butterworth filter requires fewer coefficients. Thus, it executes faster and does not require extra memory. Secondly, a Butterworth filter has no ripple in either the passband or the stopband, and has a smooth, monotonically decreasing frequency response in the transition band.

Table 12. Specifications for the low-pass Butterworth filter

Parameters	Specifications
Passband	0 -1.0 Hz
Stopband	> 2.0 Hz
Stoppband attenuation	> 20 dB
Filter Order	15

6) Investigation of Tumor Oyxgenation during Untreated Growth
Investigation of Tumor Tissue pO_2
- **^{19}F MR EPI Oximetry**

EPI is a high-speed imaging technique first developed by Mansfield [69]. EPI can be divided into single-shot EPI and multiple-shot EPI. For this project, I used a variation of the original single-shot EPI, pulse burst saturation recovery echo-planar imaging (PBSR-EPI). It has been shown to be very effective and efficient in oxygen dynamic studies [70-72]. A typical PBSR-EPI pulse sequence diagram is shown in Figure 12.
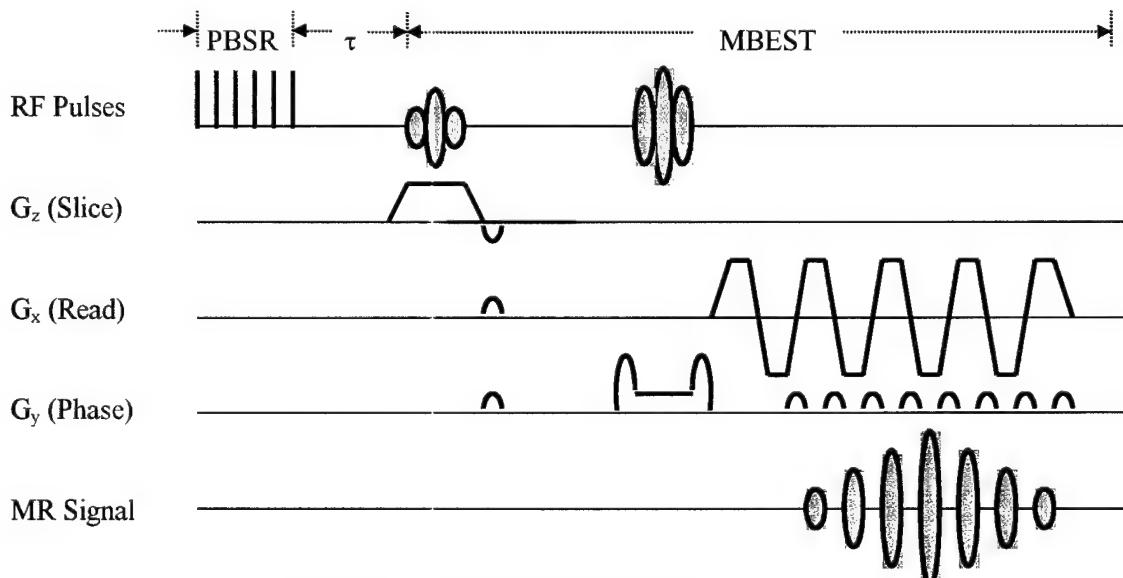
Figure 12. A typical PBSR-EPI pulse sequence diagram.

The PBSR-EPI consists of three basic building blocks: a preparation pulse sequence (PBSR), a variable delay time τ, and a single shot spin-echo EPI with "blipped" phase encoding gradient. The PBSR is a pulse train of 20 non-spatially selective 90^0 pulses with 50 ms spacing to saturate ^{19}F nuclei. Fourteen different τ values, ranging from 200 ms to 90 s, are used to modulate image intensities so that good T1 relaxation curves can be obtained. The function of the brief "blipped" phase encoding gradient between each echo is to increment phase in the k_y direction to form a blipped echo image. Fourteen EPI images are acquired with 32x32 in-plane resolution. PBSR-EPI may result in some loss of dynamic range in signal intensity, but substantially shortens the data acquisition time for a T1 experiment. By incorporating a PBSR preparation pulse sequence into EPI, each R1 (1/T1) map can be produced with a temporal resolution of ~ 6 min, facilitating measurements of dynamic changes in pO_2 accompanying therapeutic interventions and allowing the fate of individual voxels to be traced.
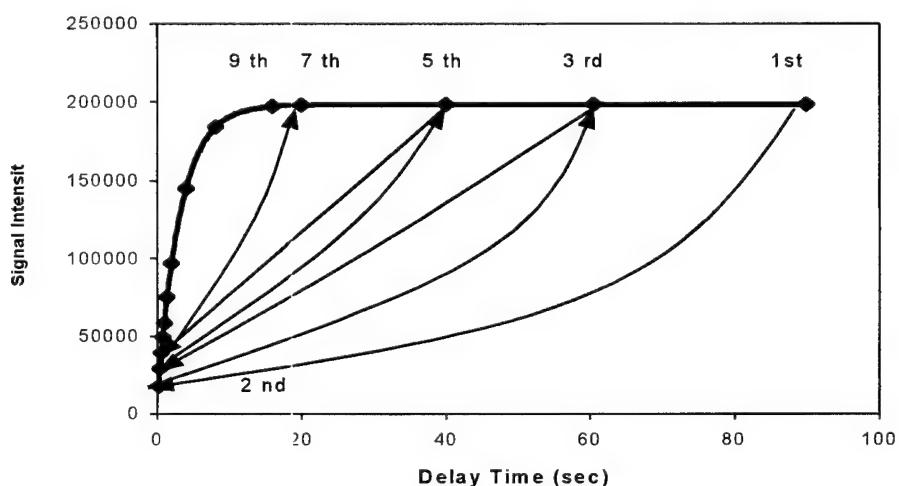
Figure 13. A schematic representation of the ARDVARC protocol.

To enhance SNR of the ^{19}F EPI images, and thus, improve the precision of R1 measurements, I used a novel data acquisition protocol developed in our lab: ARDVARC (**A**lternated **R**1 **D**elays with **V**ariable **A**cquisitions to **R**educe **C**learance effects) (Figure 13). The ARDVARC has two new features in comparison with the traditional approach. Firstly, the number of acquisitions (NA) varies with τ values. This innovation significantly improves the SNR for short delays and provides a better curve fit by additional acquisitions. Data are amplitude-corrected, *i.e.*, divided by the number of acquisitions to maintain correct signal amplitude. Secondly, longest and shortest delays are alternated to reduce bias resulting from HFB clearance or fluctuations in R1 (Table 13).

In order to determine R1, and hence pO_2, signal intensity in each voxel was fitted to a three-parameter exponential relaxation model:

$$y_n(i, j) = A(i, j) \cdot [1 - (1 + W(i, j)) \cdot \exp(-R1(i, j) \cdot \tau_n)]$$
$$(n = 1, 2, \ldots \ldots, 14)$$
$$(i, j = 1, 2, \ldots \ldots 32) \tag{20}$$

by the Levenberg-Marquardt least-squares algorithm, where $y_n(i, j)$ was the measured signal intensity of voxel (i, j) at delay time τ_n (the nth image), $A(i, j)$ was the fully relaxed signal intensity of voxel (i, j), $W(i, j)$ was a dimensionless scaling factor used for imperfect signal conversion, and $R1(i, j)$ is the relaxation rate of voxel (i, j) in unit of $\sec^{-1}$.

Table 13. ARDVARC parameters

Order of Acquisition	Order in Curve Fit (n)	Delay Time τ (sec)	Number of Acquisitions (NA)
1	14	90	1
2	1	0.2	12
3	13	60	1
4	2	0.4	12
5	12	40	1
6	3	0.6	12
7	11	20	1
8	4	0.8	12
9	10	16	2
10	5	1	8
11	9	8	2
12	6	1.5	4
13	8	4	4
14	7	2	4

Regional tumor pO_2 maps were produced by applying the calibration curve to $R1$ maps. It was found that at $37C^0$ and 4.7 T:

$$pO_2(i, j) = \left[\frac{R1(i, j) - 0.0836}{0.00188} \right] \text{(torr)} \tag{21}$$

using PBSR-EPI for HFB.

- **Respiratory Challenge Paradigms**

One of the important issues in radiotherapy is how to manipulate oxygenation in tumors and monitor its dynamic response to various therapeutic interventions noninvasively. Many protocols and techniques have been proposed. A simple intervention is respiratory challenge, *i.e.*, attempting to elevate tumor oxygenation with inhaled gas. For this project, two respiratory challenge paradigms were used to manipulate oxygenation in tumors. ^{19}F MR EPI and NIRS were used to monitor oxygen dynamic response and assess its temporal characteristics and changes in the extent of hypoxia.

(1) $\textbf{\textit{Air}}$ $\rightarrow$ $\textbf{\textit{Carbogen}}$ $\rightarrow$ $\textbf{\textit{Air}}$ $\rightarrow$ $\textbf{\textit{Carbogen}}$ $\rightarrow$ $\textbf{\textit{Air}}$
         (21% O_2)   (95% O_2 + 5% O_2)

(2) $\textbf{\textit{Air}}$ $\rightarrow$ $\textbf{\textit{Carbogen}}$ $\rightarrow$ $\textbf{\textit{Air}}$ $\rightarrow$ $\textbf{\textit{100\% O}}_2$ $\rightarrow$ $\textbf{\textit{Air}}$

Most experiments were performed using paradigm (1). However, in some cases, repeated carbogen interventions were performed sequentially to evaluate the reproducibility of the time course profiles of the tumors.

- **Investigation of Tumor Tissue Oxygen Dynamics by ^{19}F MR EPI**

Following ^{1}H and ^{19}F MRI to determine the tumor anatomy and the distribution of HFB, a series of ^{19}F MR EPI oximetry experiments were performed according to the respiratory challenge paradigms described above. During the imaging sessions, initially, rats inhaled medical grade compressed air (21% O_2) and three measurements were taken for the first phase. Subsequently, five measurements were taken for each gas switch, giving a total of twenty-three measurements. The complete five-phase imaging session took about 2.5 hours.
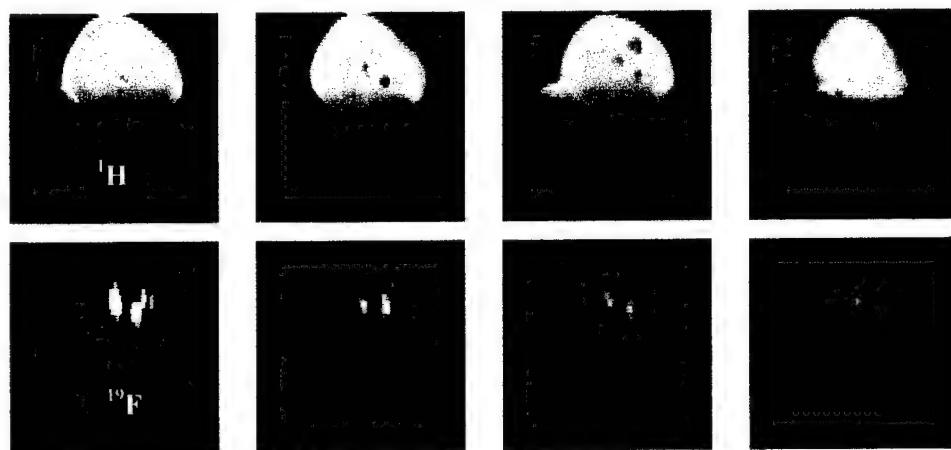

Figure 14. ^{1}H and ^{19}F coronal images of a breast tumor.

Figure 14 shows conventional spin echo (SE) ^1H images (top four) and corresponding ^{19}F SE images of a representative breast tumor. ^1H images were acquired to show the tumor anatomy and ^{19}F images to show the distribution of HFB within the tumor. In this case, the tumor was centrally labeled Figure 15 shows representative pO_2 maps obtained from a rat mammary adenocarcinoma 13762NF using ^{19}F MR EPI oximetry. Each map was acquired in 6.5 min, with (**A**) being rat breathing 33% O_2 and (**B**) carbogen (95% O_2 + 5% CO_2).
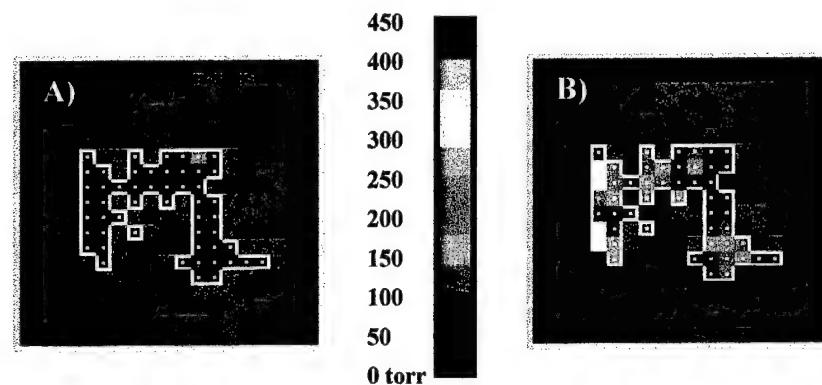
Figure 15. Representative pO_2 maps of a breast tumor.
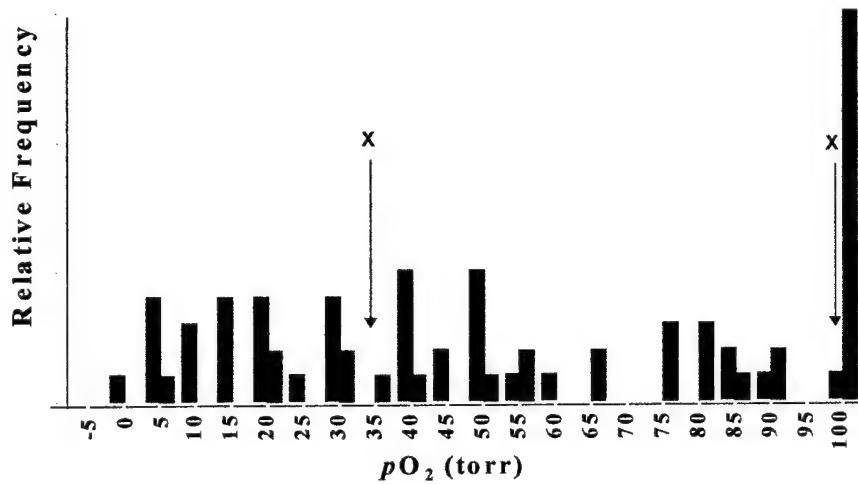
Figure 16. A representative histogram for a breast tumor.

Figure 16 shows histograms of pO_2 distributions in response to respiratory challenge in a rat mammary adenocarcinoma 13762NF. Elevating inspired O_2 (carbogen in this case) caused a substantial change in the pO_2 distribution, resulting in a shift toward

the higher pO_2 values. Arrows indicate mean (x) pO_2. Blue histogram represents baseline 33% O_2, and red histogram carbogen. Figure 17 shows dynamic changes in breast tumor mean pO_2 corresponding to Figure 15. Each data point represents mean $pO_2 \pm$ SD. The mean baseline pO_2 value was 18.1 ± 2.1 torr when the rat was breathing 33% O_2 and was 108 ± 42 torr after the gas was switched to 100% O_2 ($p < 0.009$). The pO_2 dropped to 75 $\pm$ 19 torr after the gas was switched back to 33% O_2. During the second phase of respiratory challenge, the pO_2 increased to 110.9 ± 54 torr ($p<0.02$) when the gas was switched to carbogen and dropped to 32.4 ± 33 torr after the gas was switched back to 33% O_2. As can be seen from Figure 17, ^{19}F MR EPI oximetry showed good reproducibility.
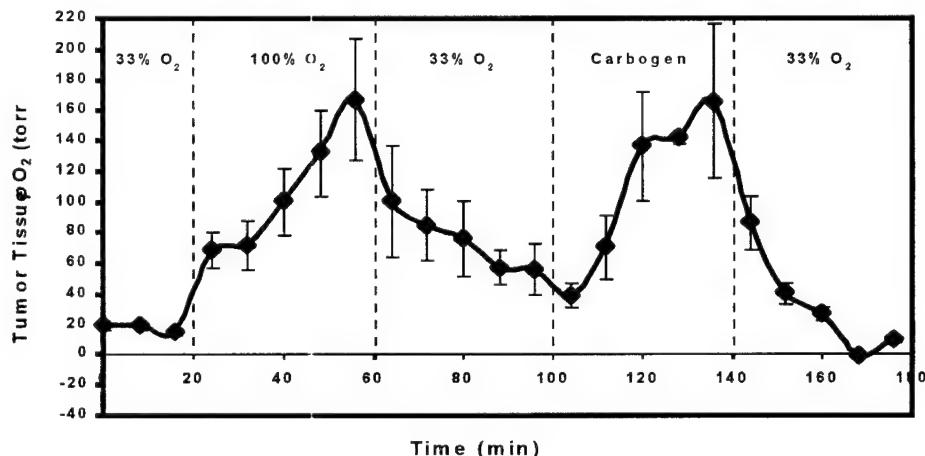
Figure 17. Dynamic response in tumor tissue pO_2.
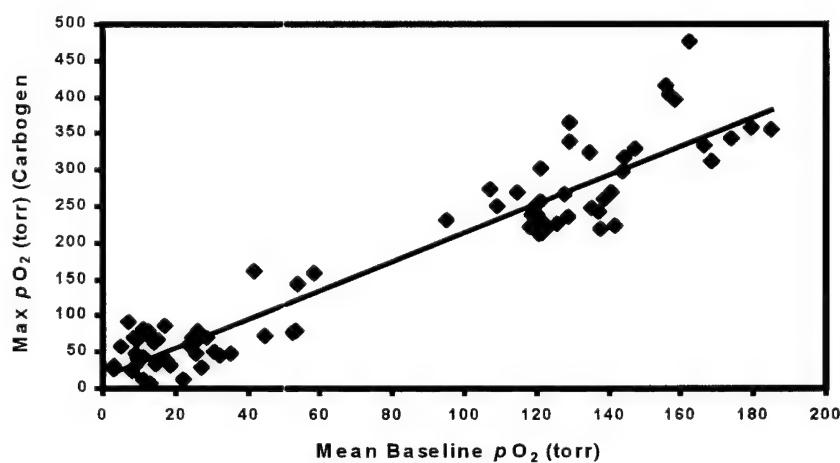
Figure 18. Maximum pO_2 vs. mean baseline pO_2 for a breast tumor

39

A strong linear correlation has been observed in some of 13762NF breast tumors between initial mean baseline pO_2 and the maximum pO_2 for a given group of voxels with respect to carbogen or oxygen breathing. For the breast tumor shown in Figure 18, an ROI of 83 voxels was selected. In this case, the linear coefficient r was found to be 0.95. This observation was of clinical significance and could help us predict tumor response to elevated oxygen breathing based on its initial baseline value. Figure 19 shows a group of 11 voxels of a second breast tumor. Once again, a strong linear correlation was observed and, in this case, r was found to be 0.86.
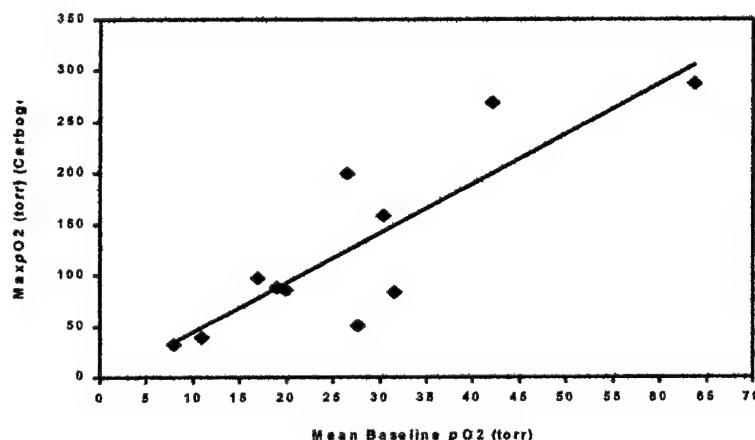
Figure 19. Maximum pO_2 vs. mean baseline pO_2 for a group of 11 voxels of a second breast tumor.
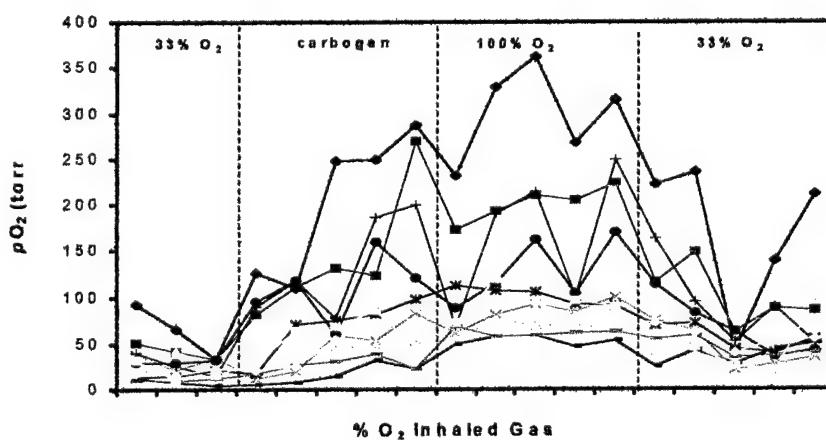
Figure 20. Dynamic changes in pO_2 for a group of 11 voxels of a second breast tumor.

The ^{19}F MR-EPI oximetry of tumor has the distinct advantage over other techniques that subsequent measurements are completely non-invasive. The greatest strength of this method is the ability to trace the fate of individual voxels (regions) with respect to therapeutic interventions. Figure 20 shows dynamic changes in pO_2 of 11 specific voxels of a second breast tumor with respect to different inhaled gases. It is noteworthy that voxels with high baseline pO_2 had significantly different response characteristics from those with initially low pO_2, which showed small changes. To further investigate the temporal response characteristics of individual voxels, we modeled the temporal response in pO_2 using exponential equations:

1) $y = a + b \cdot (1 - e^{-t/\tau})$, for increasing trend

2) $y = a + b \cdot e^{-t/\tau}$, for decreasing trend

where y is pO_2, a and b are two constants, t is time, and τ is the time constant.
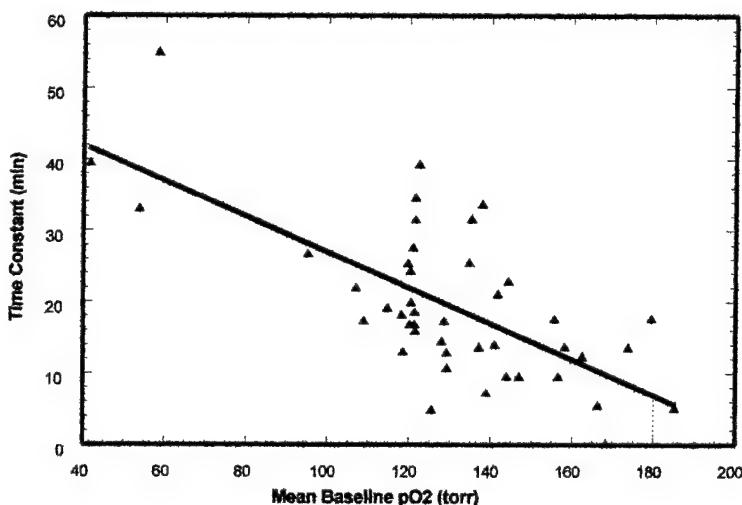
Figure 21. Time constant vs. mean baseline pO_2 of 44 specific voxels of a third breast tumor.

Figure 21 shows the relationship between time constant and mean baseline pO_2 of 44 specific voxels of a third breast tumor ($r = 0.68$). It was found that, in general, the time constants of well-oxygenated voxels ($10 \sim 20$ min) were much shorter than those of hypoxic voxels (> 50 min) and the global pO_2 time constant ($60 \sim 80$ min) was much longer than the vascular hemoglobin saturation (sO_2) time constant ($10 \sim 20$ min). In general, changes in tumor vascular sO_2 preceded tumor tissue pO_2, particularly for smaller tumors.

Investigation of Tumor Vascular [HbO$_2$] or sO$_2$ and [Hb]$_{Total}$
- **Oximetry Based on Near-Infrared Spectroscopy (NIRS)**

Near-Infrared Spectroscopy (NIRS) can be used to measure total hemoglobin concentration [Hb]$_{Total}$, oxyhemoglobin concentration [HbO$_2$], and oxygen saturation (sO$_2$) because of two things: firstly, the absorption of light by deoxyhemoglobin (Hb) and oxyhemoglobin (HbO$_2$) predominates over water and other macromolecules at the selected wavelengths; secondly, the absorption coefficient of deoxyhemoglobin (Hb) differs substantially from that of oxyhemoglobin (HbO$_2$) in the NIR region (700 – 900 nm). The traditional continuous wave spectroscopy (CWS) uses the classical Beer-Lambert's law to determine the absorption coefficient of the sample over a known optical path length and thus the concentration of the sample. Current available CWS techniques include dual-wavelength and multi-wavelength light spectroscopy, pulse oximetry, and CW brain functional imaging systems.

Theoretically speaking, however, Beer-Lambert's law is valid only for homogenous translucent solutions that do not scatter light. In a continuous medium, light photons travel at the speed of light that is dependent only on the refractive index of the medium. If this is a scattering medium, photons travel with the constant speed and direction until they collide elastically with a scatterer, resulting in a change in traveling direction. Depending on the scattering properties of the medium, the scattered photons may travel in a random direction, or in a preferential forward or backward direction. The total distance or optical path length traveled by photons between the source and detector is much longer than the geometric distance between the source and detector. In this case, Beer-Lambert's law is not valid since exact L is not known. In the absence of scatterers, the total optical path length traveled by photons before detection is simply the geometric distance between the source and detector. Thus, L is known and Beer-Lambert's law is valid. Since biological tissues are highly inhomogeneous and optically turbid, it is obvious that we can not directly apply Beer-Lambert's law to biological tissues. Light attenuation results not only from tissue absorption, but also from tissue scattering. Light absorption results mainly from absorption of oxyhemoglobin and deoxyhemoglobin, myoglobin, and cytochrome oxidase. The amount of light absorption depends on the concentrations of these molecules. Light scattering results from mitochondrion, protein, and various ions. Scattering gives rise to distributed path lengths that are significantly longer than the geometric distance between the source and detector used in Beer-Lambert's law, leading to a distorted absorption spectrum of the sample. To take scattering into account, we need to use the photon diffusion approximation theory [73] based on a general mass transfer diffusion equation. This equation allows us to describe photon migration in scattering media and compute both absorption and scattering coefficients. For this study, I used a new dual wavelength, homodyne frequency-domain near-infrared spectroscopy (NIRS) system to measure changes in tumor vascular oxyhemoglobin concentration [HbO$_2$] and total hemoglobin concentration [Hb]$_{Total}$. The theoretical formulation of the system is based on a modified Beer-Lambert's law.

- **In-Phase and Quadrature Phase Detection System**

  The dual wavelength, homodyne NIRS system (wavelengths 758 nm and 782 nm) is based on an In-phase and Quadrature-phase chip (I&Q chip). These wavelengths were chosen because they not only allow the calculation of $[HbO_2]$ and $[Hb]_{Total}$, but also fall into the range of wavelengths compatible with the low cost photo multiplier tube (PMT). The system uses only one RF source to modulate the light emitted by two laser diodes and lets the I&Q chip to determine amplitude and phase changes of light attenuated by the sample [74].
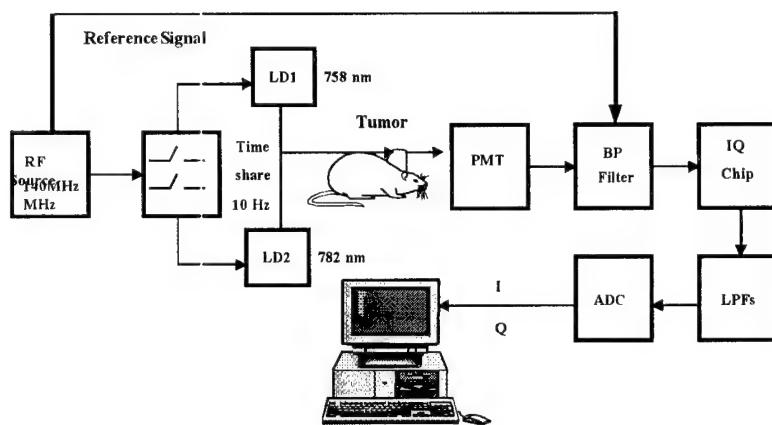
Figure 22. A schematic diagram of the NIRS I&Q system.

  Figure 22 shows a schematic diagram of the NIRS system. An RF source modulates the light from two laser diodes (LD1 and LD2) at 140 MHz through a time-sharing system. The light passes through fiber optic cables, is transmitted through the tumor tissue, and collected by a second fiber bundle. The light is then amplified by a photo multiplier tube (PMT) and filtered by a bandpass (BP) filter to pick up only the signal being modulated at 140 MHz. The signal is demodulated into I and Q components by the I&Q chip and filtered again by two lowpass filters (LPFs) to select the DC components. These final DC signals are digitized by a 12-bit analog to digital converter (ADC) and stored in a computer. Light amplitude and phase changes caused by the tumor attenuation are used to compute changes in tumor vascular oxyhemoglobin concentration $[HbO_2]$ and total hemoglobin concentration $[Hb]_{Total}$. The NIRS system is interfaced to a laptop via a National Instruments data acquisition card (DAQCard-1200) that is fully software-configurable. A National Instruments DAQ driver, NI-DAQ, is used to control the operations of the card. The graphical programming language LabView^{TM} is used to create a graphical user interface (GUI) for controlling data acquisition, processing, and display [75]. The raw data are saved in a text format and can be further processed using a variety of digital signal processing (DSP) techniques.

- **Algorithms for Computing Tumor Vascular [HbO$_2$] and [Hb]$_{Total}$**

To obtain the absorption coefficients of deoxyhemoglobin and oxyhemoglobin, it is assumed that background absorbance is negligible and deoxyhemoglobin and oxyhemoglobin are the predominant light absorbing molecules in the tumor tissue. Therefore, the absorption coefficient of the tumor can be approximated as the product of the extinction coefficients for deoxyhemoglobin and oxyhemoglobin and their respective concentrations:

$$\mu_a'^{\lambda} = \varepsilon_{Hb}^{\lambda}[Hb] + \varepsilon_{HbO_2}^{\lambda}[HbO_2] \tag{22}$$

Equation (22) has two unknowns: [Hb] and [HbO$_2$] and we can not solve for them with only one equation. If we use NIR light at two different wavelengths, then we have two equations and [Hb] and [HbO$_2$] can be obtained by solving following linear systems of equations

$$\mu_a'^{758} = \varepsilon_{Hb}^{758}[Hb] + \varepsilon_{HbO_2}^{758}[HbO_2]$$
$$\mu_a'^{782} = \varepsilon_{Hb}^{782}[Hb] + \varepsilon_{HbO_2}^{782}[HbO_2] \tag{23}$$

where μ_a^{758} and μ_a^{782} are the absorption coefficients, ε_{Hb}^{758} and ε_{Hb}^{782} the extinction coefficients for deoxyhemoglobin, $\varepsilon_{HbO_2}^{758}$ and $\varepsilon_{HbO_2}^{782}$ are the extinction coefficients for oxyhemoglobin at the wavelengths 758 nm and 782 nm, respectively, and [Hb] and [HbO$_2$] are the deoxyhemoglobin and oxyhemoglobin concentrations, respectively. Since $\varepsilon_{Hb}^{758}, \varepsilon_{Hb}^{782}, \varepsilon_{HbO_2}^{758}$, and $\varepsilon_{HbO_2}^{782}$ are physical constants, changes in [HbO$_2$] and [Hb] in tumor tissue vasculature cause changes in μ_a^{758} and μ_a^{782} according to Equations (23). Thus, by measuring changes in μ_a^{758} and μ_a^{782}, we can determine changes in [HbO$_2$] and [Hb]. Combining Equation (23) with modified Beer-Lambert's law yields equations for computing changes in [Hb] and [HbO$_2$][76].

$$\Delta[Hb] = [Hb]_P - [Hb]_B = \frac{\varepsilon_{HbO_2}^{758}\log(\frac{A_B}{A_P})^{782} - \varepsilon_{HbO_2}^{782}\log(\frac{A_B}{A_P})^{758}}{L(\varepsilon_{Hb}^{782}\varepsilon_{HbO_2}^{758} - \varepsilon_{Hb}^{758}\varepsilon_{HbO_2}^{782})} \tag{24}$$

$$\Delta[HbO_2] = [HbO_2]_P - [HbO_2]_B = \frac{\varepsilon_{Hb}^{782}\log(\frac{A_B}{A_P})^{758} - \varepsilon_{Hb}^{758}\log(\frac{A_B}{A_P})^{782}}{L(\varepsilon_{Hb}^{782}\varepsilon_{HbO_2}^{758} - \varepsilon_{Hb}^{758}\varepsilon_{HbO_2}^{782})} \tag{25}$$

where letters P and B stand for perturbation and baseline, respectively, A_B is the baseline light amplitude, A_P is the light amplitude under the physiological perturbation, L is the distance between the source and detector, and $\Delta[]$ represents a change in concentration.

The quantity (A_B / A_P) can be obtained by direct measurement. Given $\varepsilon_{Hb}^{758} = 0.359$ $cm^1 mM^{-1}$, $\varepsilon_{HbO_2}^{758} = 0.1496$ $cm^{-1} mM^{-1}$, $\varepsilon_{Hb}^{782} = 0.265$ $cm^{-1} mM^{-1}$, and $\varepsilon_{HbO_2}^{782} = 0.178$ $cm^{-1} mM^{-1}$ [77], the final expressions for computing changes in [Hb] (mM), [HbO$_2$] (mM), and [Hb]$_{Total}$ (mM) are:

$$\Delta[Hb] = \frac{1}{L}\left[7.34 \cdot \log(\frac{A_B}{A_P})^{758} - 6.17 \cdot \log(\frac{A_B}{A_P})^{782} \right] \tag{26}$$

$$\Delta[HbO_2] = \frac{1}{L}\left[-10.92 \cdot \log(\frac{A_B}{A_P})^{758} + 14.80 \cdot \log(\frac{A_B}{A_P})^{782} \right] \tag{27}$$

$$\Delta[Hb]_{Total} = \Delta\{[HbO_2] + [Hb]\}$$
$$= \frac{1}{L}\left[-3.58 \cdot \log(\frac{A_B}{A_P})^{758} + 8.63 \cdot \log(\frac{A_B}{A_P})^{782} \right] \tag{28}$$

where Equation (28) represents a change in total hemoglobin concentration in the tumor, a physiological parameter that is linearly proportional to a change in blood volume in the tumor.

- **Assessment of Temporal Characteristics of Oxygen Dynamic Response**
    As a first step in trying to quantitatively characterize the temporal response in [HbO$_2$], a simple mono-exponential model was employed to compute the time constant and the amplitude of the response:

$$y = A \cdot \left\{ 1 - \exp[-\frac{(t - t_0)}{\tau}] \right\} \tag{29}$$

where y was measured [HbO$_2$] (mM), A was a constant, representing the amplitude of the response, t (min) was time, t_0 (min) was the beginning time of the exponential response, and τ (min) was the time constant of the exponential response.

This mono-exponential model was based on an implicit assumption that a tumor is composed of a homogenous tissue with a single absorption coefficient μ of light or a single uniform compartment. Therefore, the whole tumor should respond to carbogen intervention in a single mode and this dynamic process can be completely characterized by only two parameters: amplitude A and time constant τ. This simple mono-exponential model, however, did not take into account the important fact that most tumors exhibit substantially spatial heterogeneity in both tissue density and blood vessel distribution. Therefore, a more sophisticated and realistic mathematical model, the bi-exponential

model, was also used. The model assumed that a tumor consists of two distinct homogenous tissue regions, a well-perfused region and a poorly-perfused region. The two tissue regions can be characterized optically by two different absorption coefficients, μ_1 and μ_2 and kinetically by two different time constants, τ_1 and τ_2. The bi-exponential model is

$$y = A_1 \cdot \left\{ 1 - \exp[-\frac{(t-t_0)}{\tau_1}] \right\} + A_2 \cdot \left\{ 1 - \exp[-\frac{(t-t_0)}{\tau_2}] \right\} \tag{30}$$

where t_0 (min) was the beginning time of the fast and slow exponential response, and τ_1 and τ_2 (min) were the fast and slow time constants, respectively. The parameters in the two models were obtained by fitting the data to Equations (29) and (30), respectively, using KaleidaGraph.

- **Investigation of Tumor Vascular [HbO$_2$] and [Hb]$_{Total}$ by NIRS**
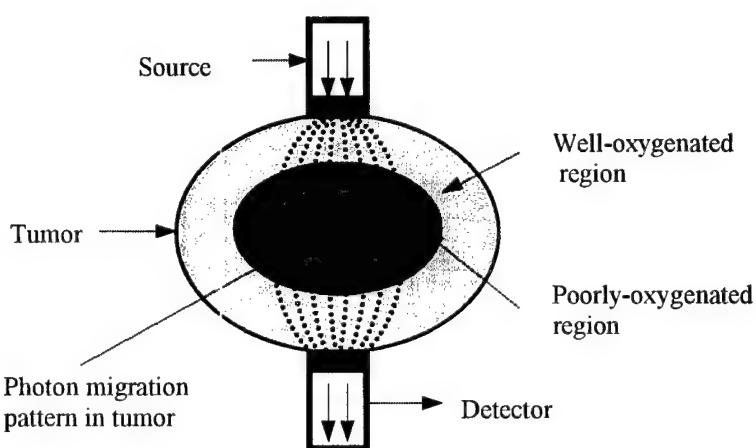

Figure 23. A schematic diagram of transmittance optical mode

Animal preparation was similar to ^{19}F MR EPI studies. The experiments were performed in transmittance optical mode. In this configuration, the light source and detector were positioned on opposite sides of the tumor and stabilized by a mechanical mechanism. The light passed through and was attenuated by the tumor. The transmitted light was then picked up by the detector. In this way, the NIR spectroscopy measured Δ[HbO$_2$] and Δ[Hb]$_{Total}$ in both peripheral and central regions of the tumor, yielding an average Δ[HbO$_2$] and Δ[Hb]$_{Total}$ (Figure 23). It was important to position the light source

and detector in such a way that they made very good optical contact with the tumor but did not exert excessive force on it. This was because excessive pressure on the tumor could hinder the tumor blood flow and thus, affect $\Delta[HbO_2]$ and $\Delta[Hb]_{Total}$. To avoid instrument drift, the NIRS system was first warmed up for about 30 minutes. Then, 5 ~ 10 minute test data were acquired to check the stability of the system using a tissue equivalent phantom with stable optical properties [78]. Once the system reached a steady state, a series of NIRS experiments were performed according to the respiratory challenge paradigms described earlier.
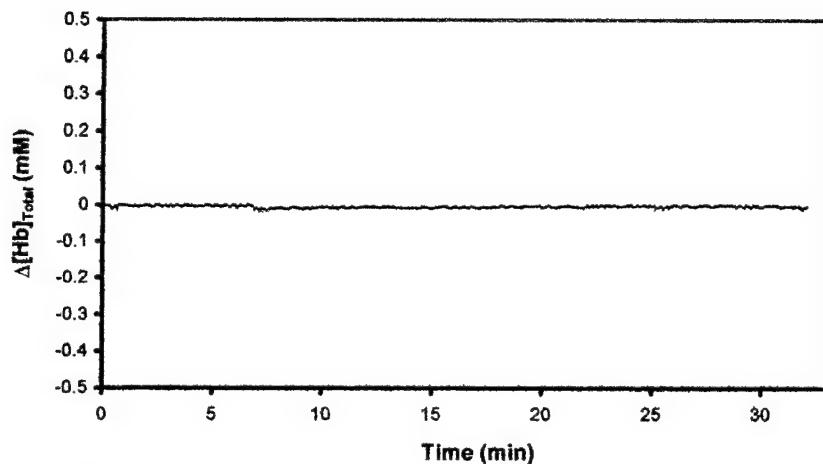

Figure 24. Result of a typical routine NIRS system drift test for $\Delta[Hb]_{Total}$ which was obtained by using Equation (28).

Table 14. Summery of five system drift tests obtained using a tissue phantom

NO	SD of $[HbO_2]$ (mM)	SD of $[Hb]_{Total}$ (mM)
1	0.0053	0.0037
2	0.0043	0.0025
3	0.0056	0.0034
4	0.0066	0.0032
5	0.0046	0.0023

Figure 24 shows the results of a typical routine system drift test for $\Delta[Hb]_{Total}$ over a period of 33 minutes. The test was performed using a tissue equivalent phantom with a source-to-detector separation of 5.0 cm. The result was obtained using Equation (28). For

this particular drift test, the standard deviation (SD) for $\Delta[Hb]_{Total}$ was 0.0034 (mM), indicating that the NIRS system had a superior stability. Table 14 is a summery of five system drift tests obtained under identical experimental conditions, but at different dates. As can be seen from Table 14, the standard deviations for all tests were of the same order, suggesting the NIRS system was very stable in terms of variability. In addition, I also used a chunk of fresh red port meat ($3 \times 3 \times 4$ cm^3) to further evaluate the system stability. In this case, the source-to-detector separation was 3.0 cm and the drift tests were repeated for four times, with a time interval of one hour between the tests. Table 15 summarizes the results.

Table 15. Summery of four system drift tests obtained using a chunk of fresh port meat ($3 \times 3 \times 4$ cm^3).

| NO	SD of [HbO$_2$] (mM)	SD of [Hb]$_{Total}$ (mM)
1	0.0047	0.0018
2	0.0048	0.0019
3	0.0053	0.0023
4	0.0043	0.0016
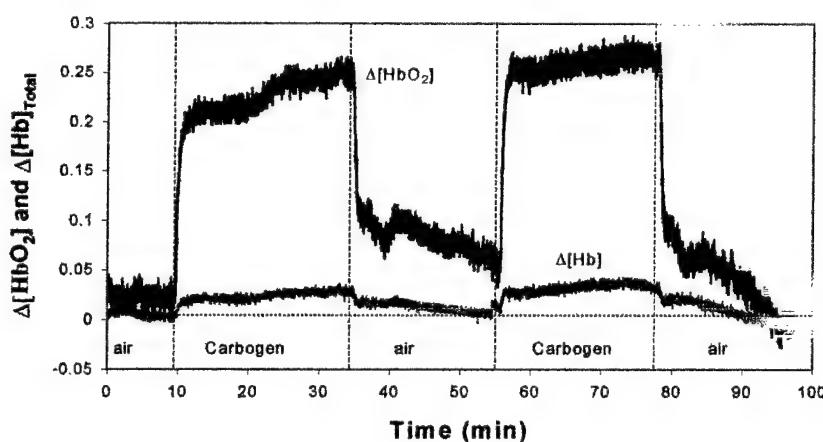
Figure 25. Time course profile of $\Delta[HbO_2]$ and $\Delta[Hb]_{Total}$ in response to carbogen intervention for a representative 13762NF breast tumor (14.8 cm^3).

Figure 25 shows the time course impacts of inhaled gases on changes in tumor vascular $\Delta[HbO_2]$ and $\Delta[Hb]_{Total}$ for a representative 13762NF breast tumor (14.8 cm^3). Repeated carbogen interventions were performed sequentially to evaluate the

reproducibility of the time course profile of the tumor. The data were acquired in transmittance mode with a source-to-detector distance of 2.0 cm. To show the quality of the raw data, averaging and filtering were not applied to the curve. The vertical dotted lines mark the beginning of each gas switch. The measurement uncertainties in $\Delta[HbO_2]$ and $\Delta[Hb]_{Total}$ were estimated using baseline data based on error propagation theory and were only labeled at representative locations. The initial baseline $\Delta[HbO_2]$ value was about 0 mM when the rat was breathing air over a period of 10 minutes. Immediately following a gas switch from air to carbogen, $\Delta[HbO_2]$ rose momentarily and significantly ($p < 0.0001$) from 0 mM to about 0.2 mM within the first 70 second and then increased further at a slower, but still significant rate ($p < 0.0001$) to about 0.25 mM for the next 20 minutes until an apparent saturation was reached. After the gas was switched back to air, $\Delta[HbO_2]$ did not decrease until about 30 – 40 seconds later when a sudden and significant drop occurred, followed by a gradual return to the baseline. Note that there was a small overshoot in $\Delta[HbO_2]$ as it was returning to the baseline and this overshoot also appeared in the second carbogen intervention. It was found that, for some tumors, this final baseline value was little bit higher than the initial baseline value. Detailed analysis also revealed that $\Delta[Hb]_{Total}$ showed a similar time course profile, but at a much less dramatic and significant level in terms of both time constant and amplitude. It is important to point out that similar time course response patterns were observed in all 13762NF breast tumors, though the time constants and amplitudes of $\Delta[HbO_2]$ and $\Delta[Hb]_{Total}$ varied with tumor size.
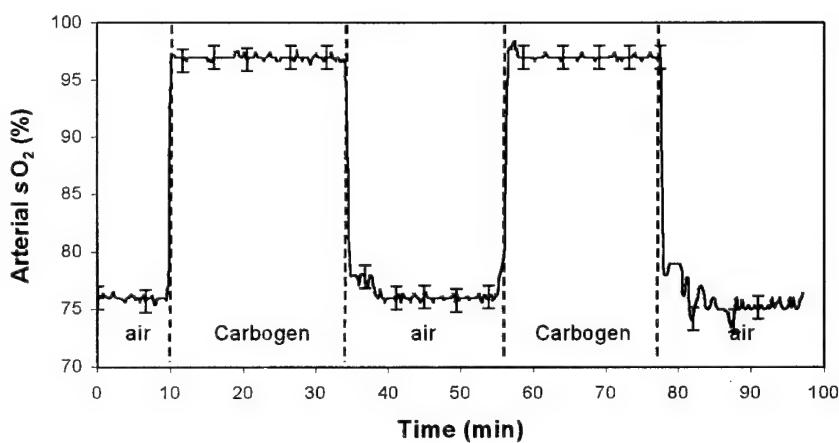

Figure 26. Time course profile of the systemic arterial s_aO_2 obtained with a pulse oximeter in response to carbogen intervention. The error bars represent standard deviation estimated using the baseline data

The systemic arterial hemoglobin oxygen saturation s_aO_2 of the rat was also monitored using a pulse oximeter placed on the hind foot. This was designed to

investigate s_aO_2 response to carbogen intervention and determine the relationship between s_aO_2 and $\Delta[HbO_2]$. Figure 26 shows s_aO_2 time course profile of the same rat in response to carbogen intervention. The data were acquired simultaneously with $\Delta[HbO_2]$ and $\Delta[Hb]_{Total}$ data and smoothed during postprocessing. In comparison to $\Delta[HbO_2]$ response, s_aO_2 rose almost immediately from 76% to 97% in about 20 seconds following the onset of carbogen breathing, indicating a much shorter time constant than that of $\Delta[HbO_2]$. s_aO_2 remained at 97% during the course of carbogen administration over the next 20 minutes until the cessation of carbogen breathing. Then s_aO_2 dropped very rapidly to its baseline value of 76%. Twenty minutes later, the second cycle of carbogen intervention was initiated and s_aO_2 showed an almost identical response profile.
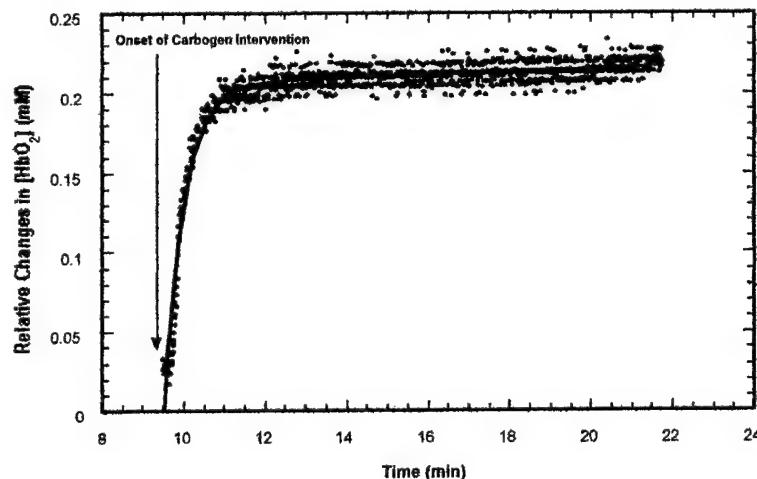

Figure 27. The best bi-exponential fit gave: $0.031 + 0.177\{1\text{-}exp[-(t-9.6)/0.293]\}$ $+0.23\{1\text{-}exp[-(t-11.43)/3.985]\}$, with $r = 0.991$, whereas the best mono-exponential fit gave: $0.033 + 0.179\{1 - exp[-(t - 9.61)/0.53]\}$, with $r = 0.971$.

To quantitatively characterize the dynamic features of $\Delta[HbO_2]$, we computed the time constants of $\Delta[HbO_2]$ response using two different mathematical models: a mono-exponential model and a bi-exponential model. The models were fit to the rising portion of the raw data corresponding to the first carbogen intervention. Figure 27 shows only the bi-exponential curve fit. The bi-exponential model gave two time constants: $\tau_1 = 0.293 \pm 0.023$ (min) and $\tau_2 = 3.985 \pm 0.056$ (min) ($r = 0.991$), representing the two phases of a bi-modal response: the fast phase and the slow phase. In terms of tumor perfusion based on the tumor model depicted in Figure 23, the former could be a physiological indicator of tumor blood perfusion in well-oxygenated regions and the latter in poorly-oxygenated regions. The mono-exponential model yielded only one time constant: $\tau = 0.530 \pm 0.015$ (min) ($r = 0.971$), a possible physiological indicator of tumor blood

perfusion for a homogeneous tumor model. The bi-exponential model gave a better curve fit than the mono-exponential model, as is manifested by their respective r values. This was true for all tumors, especially for larger tumors.
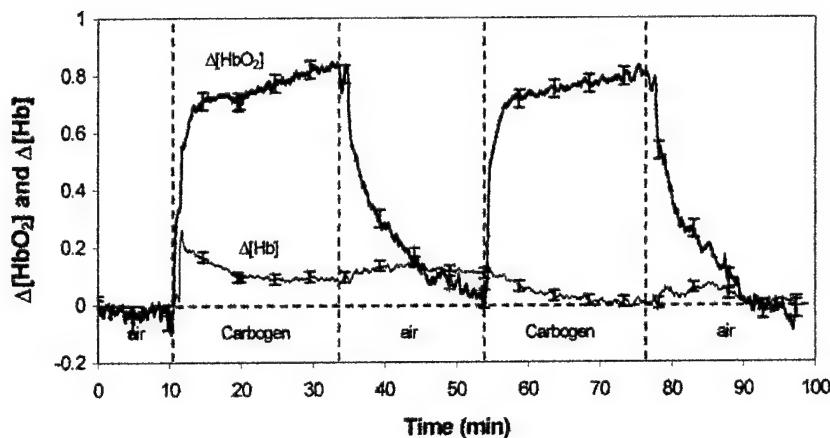

Figure 28. Time course profile of $\Delta[HbO_2]$ and $\Delta[Hb]_{Total}$ in response to carbogen intervention for a second breast tumor (9.9 cm^3).

Figure 28 shows the time course profile of $\Delta[HbO_2]$ and $\Delta[Hb]_{Total}$ in response to carbogen intervention for a second breast tumor (9.9 cm^3). The data were also acquired in transmittance mode with a source-to-detector distance of 1.9 cm. Again, we saw a similar response pattern here. After the gas was switched from air to carbogen, $\Delta[HbO_2]$ rose sharply and significantly ($p < 0.0001$) from 0 mM to about 0.7 mM within the first 2.5 minutes. This was a three-fold increase in amplitude as compared to the first tumor, suggesting that this is a better-perfused tumor. $\Delta[HbO_2]$ continued to increase further at a slower rate for the rest duration of carbogen administration. After the gas was switched back to air, $\Delta[HbO_2]$ decreased monotonically and exponentially back to the baseline. Here, we did not observe the small overshoot as seen in the first tumor during the course of air breathing. Interestingly, in this case, $\Delta[Hb]_{Total}$ responded differently to carbogen intervention from the first tumor. It did not exhibit a regular response pattern. Initially, $\Delta[Hb]_{Total}$ increased sharply in response to carbogen intervention, but showed very little changes for the subsequent gas switches. Again, the dynamic response in $\Delta[HbO_2]$ was analyzed using the two exponential models. The bi-exponential model gave: $\tau_1 = 0.853 \pm 0.0079$ (min) and $\tau_2 = 7.555 \pm 0.089$ (min) ($r = 0.991$), whereas the mono-exponential model gave: $\tau = 1.655 \pm 0.022$ (min) ($r = 0.938$). As in the first case, the bi-exponential model provided a better curve fit.

We found that there was a strong linear relationship ($r = 0.843$) between $\Delta[Hb]_{Total}$ and maximum $\Delta[HbO_2]$ for a group of 38 breast tumors as shown in Figure 29. This suggests that an increase in $\Delta[HbO_2]$ was caused in part by an increase in $\Delta[Hb]_{Total}$, *i.e.*, an increase in total blood volume in tumors. This means that breathing carbogen can increase tumor blood flow and, thus, improve tumor oxygenation.
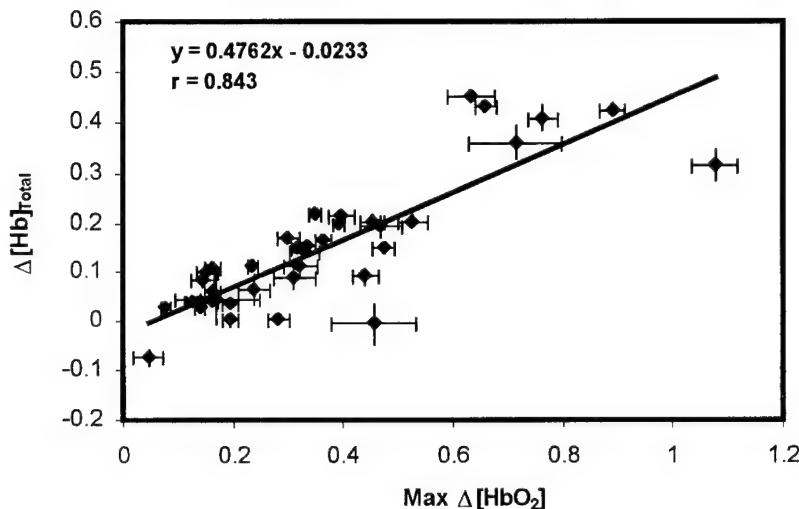
**Figure 29.** Relationship between $\Delta[Hb]_{Total}$ and $\Delta[HbO_2]$ for a group of 38 breast tumors.
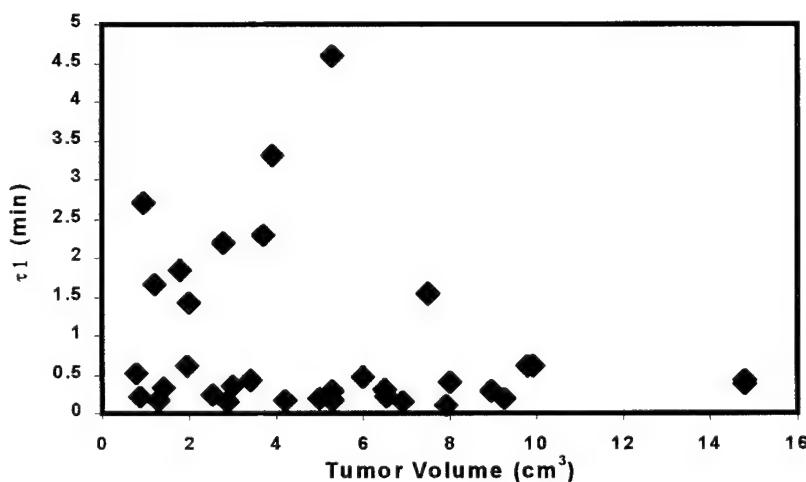
Figure 30. Relationship between fast time constant $\tau 1$ and tumor volume.

We also systematically investigated the relationships between time constants and tumor volume. Figure 30 shows the correlation between fast time constant $\tau 1$ and tumor volume and Figure 31 shows the correlation between slow time constant $\tau 2$ and tumor

volume for a group of 31 tumors. As can be seen from Figures 30 and 31, there were no clear relationships between time constants and tumor volume.
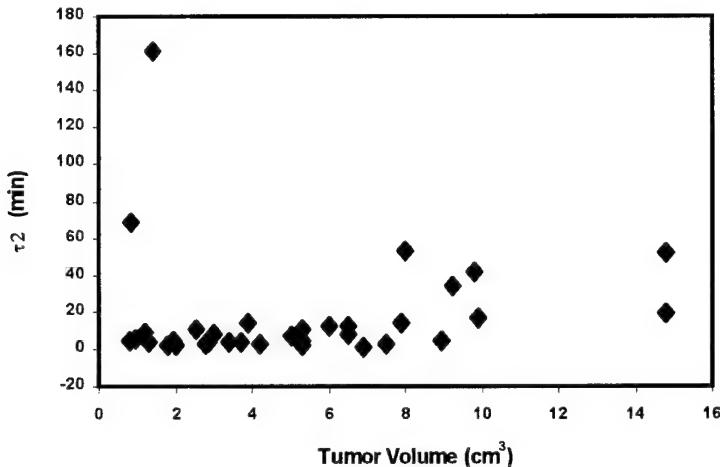

Figure 31. Relationship between slow time constant τ2 and tumor volume.

To Investigate Tumor Physiology in Response to Irradiation

One of the reasons for the birth of modern fractionated radiotherapy was to exploit tumor reoxygenation that had been found to occur following each irradiation. Since early 1980s, many new fractionation protocols have been designed, including hyperfractionation and accelerated fractionation. Currently, however, the timing of successive doses is not optimized for individual patients/tumors, but rather is based on experience with cell culture, animal tumor model systems, and clinical trials. The possibility of monitoring changes in tumor oxygenation following radiotherapy would of great significance in predicting the optimal time for delivering sequential radiation doses during a course of fractionated radiotherapy.

- **Irradiation**

Mammary adenocarcinomas 13762NF were implanted in pedicles as described earlier. When tumors reached about 1 cm in diameter, they were irradiated using a Varian CLINAC 4-100 (4 MeV photon beam) in the Department of Radiation Oncology outside normal business hours. Rats were anesthetized with 200 μl ketamine hydrochloride i.p. and maintained under general gaseous anesthesia with air (1.0 dm³/min) and 1.0% isoflurane for 1 hour prior to irradiation to stabilize tumor oxygenation. Tissue equivalent bolus material was placed around the tumors to ensure uniformity of dose to the tumors. A treatment plan was computed based on a source-to-axis distance (SAD) of 100 cm and a field size of 5 × 5 cm. Tumors were irradiated with a 4 MeV photon beam from both sides with 10 Gy delivered from each side at a rate of 2 Gy/min, giving a total dose of 20

Gy. Prior to irradiation, baseline tumor oximetry was performed and then, the measurements were repeated again following irradiation in order to examine the extent and time course of tumor hypoxiation and reoxygenation. Tumor size was measured once every two day following irradiation.
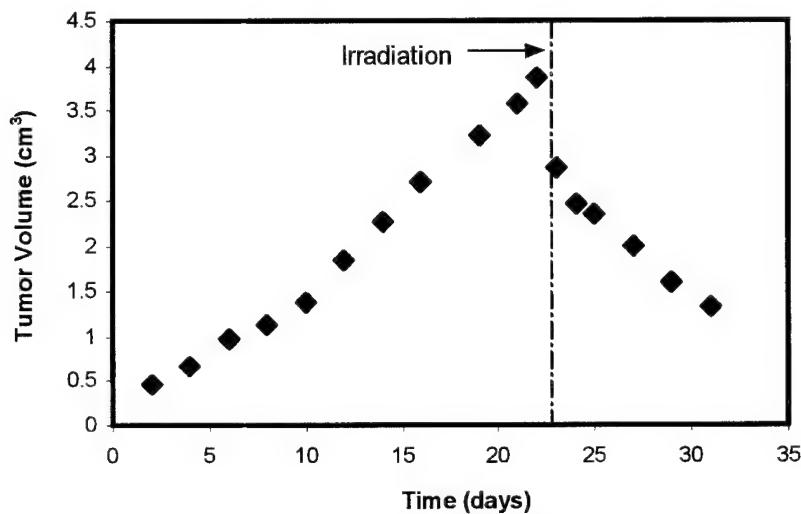

Figure 32. Tumor volume as a function of time following a single dose irradiation (20 Gy).

Figure 32 shows the growth curve of a representative mammary adenocarcinoma 13762NF before and after a single dose irradiation (20 Gy). Irradiation caused a significant decrease in tumor volume ($p < 0.007$). Changes in tumor vascular oxyhemoglobin concentration $\Delta[HbO_2]$ were measured at 2 hours, 24 hours, 48 hours, and 96 hours following radiotherapy and the results, obtained by fitting the raw data to the bi-exponential model, are listed in Table 16.

Table 16. Results of tumor oxygenation following radiotherapy

	Vol (cm³)	A1(mM)	τ1(min)	A2 (mM)	τ2 (min)	A1/A2	(A1/A2)/(t1/t2)	r
Pre_Irradiation	3.85 cm³	0.471	0.241	0.161	5.357	2.932	65.184	0.947
2 Hrs Post-Irradia	2.86 cm³	1.024	0.256	0.304	61.305	3.365	806.494	0.951
24 Hrs Post-Irradia	2.45 cm³	0.140	0.071	0.348	4.157	0.401	23.358	0.957
48 Hrs Post-Irradia	2.36 cm³	0.032	0.113	0.080	4.185	0.399	14.817	0.987
96 Hrs Post-Irradia	1.99 cm³	0.117	4.871	0.086	4.886	1.355	1.360	0.944

7) Dissertation

The studies described in this report constitute a part of my dissertation, which will be completed by the end of the year.

4. KEY RESEARCH ACCOMPLISHMENTS

- The pedicle tumor model was proven to be ideally suited for *in vivo* NIRS and MRI studies, therapy, and manipulation.

- The pedicle tumor model allowed accurate measurement of tumor size and had no significant difference from the traditional subcutaneous site in the thigh in terms of growth.

- Mammary adenocarcinomas 13762NF were found to have a viable, well-oxygenated peripheral region, and a necrotic, poorly-oxygenated central region.

- Mammary adenocarcinomas 13762NF were found to have a silent phase ranging from 2 to 3 weeks and a mean volume doubling time (VDT) of 4 days.

- The first order, autonomous differential equation was proven to be a good tumor growth model at least for a short period of growth for mammary adenocarcinomas 13762NF.

- For the birdcage resonator, laboratory bench testing indicated that the unloaded Qs for both proton and fluorine resonant modes were similar and relatively low. The loaded Q dropped by about 36% for fluorine and 39% for proton. Phantom imaging found that the B_1 fields were somewhat heterogeneous across usable volume of the resonator for both resonant modes.

- The slotted tube resonator had the capability of being continuously tuned in the frequency range of 150 MHz ~ 220 MHz. The resonator had high Q values and short 90^0 pulse widths for both proton and fluorine. In addition, the B_1 field homogeneity was found to be excellent for proton resonance and reasonably good for fluorine resonance.

- Both resonant frequencies of the slotted tube resonator were stable and immune to external electromagnetic interference.

- The copper shield not only lowered the Q value of the resonator, but also increased the RF pulse width.

- For the slotted tube resonator, NMR samples had a much stronger effect on the ^{19}F resonance than on the ^1H resonance.

- The HFB signal intensity was found to decay exponentially with a typical biological half-life ranging from $T_{1/2} = 700$ to 1200 min, which, we believe, would provide an indication of relative tumor blood flow (TBF).

- The global and regional clearance and redistribution of HFB within the tumors did not interfere with ^{19}F MR EPI oximetry.

- Tumor voxels with high baseline pO_2 had significantly different response characteristics from those with initially low pO_2, with voxels of high baseline pO_2 showing significant changes in pO_2 while voxles of low baseline pO_2 showing small changes.

- Time constants (τ) of well-oxygenated voxels (10 ~ 20 min) were much shorter than those of hypoxic voxels (> 50 min). The global pO_2 time constant (60 ~ 80 min) was much longer than the blood hemoglobin saturation (sO_2) time constant (10 ~ 20 min).

- NIR spectroscopy showed significant changes in tumor vascular oxygenation (sO_2) accompanying respiratory interventions. ^{19}F MR-EPI showed significant changes in tumor tissue pO_2, with considerable regional heterogeneity in both absolute values and rate of change accompanying interventions. Changes in tumor vascular sO_2 preceded tumor tissue pO_2, particularly for smaller tumors.

- Strong correlation existed between the maximum pO_2 value attained during the course of an experiment and mean baseline pO_2 and between mean pO_2 and mean baseline pO_2.

- ^{19}F EPI oximetry of HFB was proven to be a useful technique for measuring tumor oxygenation.

- pO_2 and the distribution of pO_2 in breast adenocarcinomas 13762 NF changed with tumor growth and there existed heterogeneity in pO_2 distribution.

- Tumor oxygenation could be manipulated by inhaling different gases.

- We found that breathing elevated FO_2 had a significant effect on arterial s_aO_2, tumor vascular [HO_2], and tumor tissue pO_2. s_aO_2 had the fastest response, followed by [HO_2], and pO_2.

- NIR spectroscopy is completely non-invasive, inexpensive, portable, and amenable to real-time measurements.

- We found that there was a strong linear relationship between $\Delta Hb]_{Total}$ and maximum $\Delta[HbO_2]$ following carbogen intervention.

- We found that there was no clear relationship between time constants, as determined by NIRS, and tumor volume.

- Irradiation caused a significant decrease in tumor volume ($p < 0.007$).

- Tumor vascular oxyhemoglobin concentration $\Delta[HbO_2]$ changed following radiotherapy.

5. REPORTABLE OUTCOMES

----PUBLICATIONS:

Manuscripts

1) **"Tumor Oximetry: A Comparison between Near-infrared Frequency-Domain Spectroscopy of Hemoglobin Saturation and ^{19}F MRI of Hexafluorobenzene"**
Katherine L. Worden, **Yulin Song**, Xin Jiang, Anca Constantinescu, Ralph P. Mason, and Hanli Liu, SPIE Vol. 3597:601-610, 1999.
(Presented in part at the International Symposium on Biomedical Optics, sponsored by the Society of Photo-Optical Instrumentation Engineers (**SPIE**), 1998).

2) **"Tumor Oxygen Dynamics: Comparison of ^{19}F MR EPI and Frequency Domain NIR Spectroscopy"**
Yulin Song, Kate L. Worden, Xin Jiang, Dawen Zhao, Anca Constantinescu, Hanli Liu, and Ralph P. Mason, **ISOTT**, 1999.

3) **"Tumor Oximetry: Comparison of ^{19}F MR EPI and Electrodes"**
Ralph P. Mason, Sandeep Hunjan, Anca Constantinescu, **Yulin Song**, Dawen Zhao, Eric W. Hahn, Peter P. Antich, and Peter Peschke, **ISOTT**, 1999.

4) **"Noninvasive Investigation of Blood Oxygenation Dynamics of Tumors by Near-Infrared Spectroscopy"**
Hanli Liu, **Yulin Song**, Katherine L. Worden, Xin Jiang, Anca Constantinescu, and Ralph P.Mason, Applied Optics, October, 2000.

Abstracts

1) **"Regional Tumor Oxygen Tension and Blood Flow: Correlation Studies Using 19F PBSR-EPI of Hexafluorobenzene"**
Yulin Song, Ralph P. Mason, Sandeep Hunjan, Anca Constantinescu, Eric Hahn, and Peter Antich.
(Presented at the Workshop on Magnetic Resonance in Experimental and Clinical Cancer Research, sponsored by the International Society for Magnetic Resonance in Medicine (**ISMRM**), St. Louis, November, 1998).

2) **"Tumor Oxygen Dynamics: Comparison between ^{19}F MR-EPI of Hexafluorobenzene and Frequency Domain NIR Spectroscopy"**
Yulin Song, Kate L. Worden, Xin Jiang, Dawen Zhao, Anca Constantinescu, Hanli Liu, and Ralph P. Mason.
(Presented at the 27th Annual Meeting of International Society on Oxygen Transport to Tissue (**ISOTT**), Proc 27th, **ISOTT**, Dartmouth, NH, August, 1999).

3) **"Tumor Oximetry: Comparison of ^{19}F MR EPI and Electrodes"**
Ralph P. Mason, Sandeep Hunjan, Anca Constantinescu, **Yulin Song**, Dawen Zhao, Eric W. Hahn, Peter P. Antich, and Peter Peschke.
(Presented at the 27th Annual Meeting of International Society on Oxygen Transport to Tissue (**ISOTT**), Proc 27th, **ISOTT**, Dartmouth, NH, August, 1999).

4) **"Tumor Oxygenation and Measurement of Regional Dynamic Changes"**

Ralph P. Mason, Sandeep Hunjan, Anca Constantinescu, **Yulin Song**, Eric W. Hahn, Peter P. Antich, Christian Blum, and Peter Peschke.
(Presented at International Conference on Molecular Determinants of Sensitivity to Antitumor Agents, sponsored by American Association for Cancer Research (**AACR**), Whistler, Canada, March, 1999).

5) **"Regional Tumor Tissue pO_2 and Blood sO_2 : Comparison of ^{19}F MR EPI and Frequency Domain NIR Spectroscopy"**
Yulin Song, Xin. Jiang, Dawen. Zhao, Anca Constantinescu, Hanli. Liu, and Ralph. P. Mason.
(Presented at the Eighth Scientific Meeting and Exhibition of the **ISMRM**, Denver, Colorado, April, 2000).

6) **"Noninvasive Measurement of Tumor Hemoglobin Dynamics Using Near-Infrared Spectroscopy"**
Hanli Liu, **Yulin Song**, Katherine L. Worden, Anca Constantinescu, and Ralph P.Mason.
(Presented at the Biomedcal Topical Meetings of Optical Society of America (**OSA**), Miami Beach, FL, April 2-5, 2000)

7) **"Tumor Oximetry: An Enhanced Dynamic Mapping Procedure Using ^{19}F Echo Planar MRI"**
Dawen Zhao, Sandeep Hunjan, Anca Constantinescu, **Yulin Song**, Eric W. Hahn, Peter P. Antich, and Ralph P. Mason.
(Presented at Radiation Research Meeting, Albuquerque, May 2000).

8) **"Regional Tumor Oxygen Dynamics: Relating Tissue $_pO_2$ to the Vasculature"**
Yulin Song, Xin Jiang, Dawen Zhao, Anca Constantinescu, Hanli Liu, and Ralph P. Mason.
(Presented at the Era of Hope Meeting sponsored by the Department of Defense, Atlanta, GA, June 8-11, 2000).

9) **"FREDOM (Fluorine Relaxometry using Echo planar imaging for Dynamic Oxygen Mapping): a contextual review"**
Ralph P. Mason, Dawen Zhao, Anca Constantinescu, **Yulin Song**, Lan Jiang and Eric W. Hahn
(Presentated at ISMRM Workshop on MR in Experimental and Clinical Cancer Research in the New Millennium).

10) **"Diverse Approaches to Monitoring Oxygen Dynamics in Rat Breast and Prostate Tumors"**
Dawen. Zhao, **Yulin Song**, Han Liu, Amca. Constantinescu, Eric W. Hahn, and Ralph. P. Mason,
(Presented at the Conference on Chemical Modifiers of Cancer Treatment, Banff, Canada, Oct. 2000).

----DEGREE OBTAINED THAT IS SUPPORTED BY THIS AWARD
Ph.D. in Biomedical Engineering

----EMPLOYMENT OR RESEARCH OPPORTUNITIES RECEIVED ON TRAINING SUPPORTED BY THIS AWARD
Post-doctoral fellow in the Department of Radiation Oncology, School of Medicine, Stanford University (will start on March 1, 2001)

6. CONCLUSIONS

Regional tumor tissue pO_2, vascular $[HbO_2]$ or sO_2, and $[Hb]_{Total}$ are critical physiological parameters in radiotherapy and some forms of chemotherapy. The capability to measure and manipulate them will provide insight into progressive physiological changes in a tumor accompanying interventions and enhance therapeutic outcomes. NIRS has the advantages of being entirely noninvasive, inexpensive, portable, and real-time. But the ^{19}F MR EPI approach clearly reveals detailed oxygenation heterogeneity. The correlation of NIRS and ^{19}F MR EPI technologies will help us understand issues of oxygen transport, perfusion, and consumption. I believe that synergistic application of multiple approaches to tumor oxygenation can lead to optimized tumor therapy.

7. REFERENCES

1. Vaupel, P., Thews, O, Kelleher, D. K., and Höckel, M., "Current status of knowledge and critical issues in tumor oxygenation", *In*: Hudetz and Bruley (eds), *Oxygen Transport to Tissue XX*, Plenum Press: New York, 591-602 (1998).

2. Vaupel, P., "Vascularization, blood flow, oxygenation, tissue *p*H, and bioenergetic status of human breast cancer", *In*: Nemoto and LaManna (eds), *Oxygen Transport to Tissue XVIII*, Plenum Press: New York, 243-253 (1997).

3. Vaupel, P., "Oxygen transport in tumors: Characteristics and clinical implications", *Adv. Exp. Med. Biol.*, **388**:341-351 (1996).

4. Hirst, D. G., "Anemia: A problem or an opportunity in radiotherapy?", *Int. J. Radiat. Oncol. Biol. Phys.*, **12**:2009-2017 (1986).

5. Busch, O. R., Hop, W. C., Hoynck van Papendrecht, M. A., Marquet, R. L., Jeekel, J., "Blood transfusions and prognosis in colorectal cancer", *N. Engl. J. Med.*, **328**:1372-1376 (1993).

6. Lavey, R. S., Dempsey, W. H., "Erythropoietin increases hemoglobin in cancer patients during radiation therapy", *Int. J. Radiat. Oncol. Biol. Phys.*, **27**:1147-1152 (1993).

7. Thomlinson, R. H., and Gray, L. H., "The histological structure of some human lung cancers and the possible implications for radiotherapy", *Br. J. Cancer*, **9**:539-549 (1955).

8. Brizel, D. M, Sibley, G. S., Prosnitz, L. R., Scher, R. L, and Dewhirst, M.W., "Tumor hypoxia adversely affects the prognosis of carcinoma of the head and neck", *Int. J. Radiat. Oncol. Biol. Phys.*, **38**:285-289 (1997).

9. Höckel, M., Knoop, C., Schlenger, K., "Intratumoral pO_2 predicts survival in advanced cancer of the utertine cervix", *Radiother. Oncol.*, **26**:45-50 (1993).

10. Fyles, A. W., Milosevic, M., Wng, R., Kavanagh, M. C., Pintile, M., Sun, A., Chapman, W., Levin, W., Manchul, L., Keane, T. J., and Hill, R. P., "Oxygenation predicts radiation response and survival in patients with cervix cancer", *Radiother. Oncol.*, **48**:149-156 (1998).

11. Teicher, B., Lazo, J., and Sartorelli, A., "Classification of antineoplastic agents by their selective toxicities toward oxygenated and hypoxic tumor cells", *Cancer Res.*, **41**:73-81 (1981).

12. Siemann, D. W., "Potentiation of chemotherapy by hypoxic cell radiation sensitizers – a review", *Int. J. Radiat. Oncol. Biol. Phys.*, **8**:1029-1034 (1982).

13. Chapman, J. D., Stobbe, C. C., Arnfield, M. R., Santus, R., Lee, J., and McPhee, M. S., "Oxygen dependency of tumor cell killing *in vitro* by light activated photofrin II", *Radiat. Res.*, **126**:73-79 (1991).

14. Pötgens, A. J. G., Westphal, H. R., de Waal, R. M. W, and Ruiter, D. J., "The role of vascular permeability factor and basic fibroblast growth factor in tumor angiogenesis", *Biol. Chem.*, Hopper-Seyler, **376**:57-70 (1995).

15. Blancher, C., and Harris, A. L., "The molecular basis of the hypoxia response pathway: tumor hypoxia as a therapy target", *Cancer Metastasis Rev.*, **17**:187-194 (1998).

16. Höckel, M., Schlenger, K., Aral, B., Mitze, M., Schäffer, U., and Vaupel, P., "Association between tumor hypoxia and malignant progression in advanced cancer of the uterine cervix", *Cancer Res.*, **56**:4509-15 (1996).

17. Brizel, D. M., Scully, S. P., Harrelson, J. M., "Tumor oxygenation predicts for the likelihood of distant metastases in human soft tissue sarcoma", *Cancer Res.*, **56**:941-943 (1996).

18. Sundfor, K., Lyng, Rofstad, E. K., "Tumor hypoxia and vascular density as predictors of metastasis in squamous cell carcinoma of the uterine cervix", *Br. J. Cancer*, **78**:822-827 (1998).

19. Young, S. D., Marshall, R. S., and Hill, R. P., "Hypoxia induces DNA overreplication and enhances metastatic potential of murine tumor cells", *Proc. Natl. Acad. Sci. USA*, **85**:9533-9537 (1988).

20. Reynolds, T. Y., Rockwell, S., and Glazer, P. M., "Genetic instability induced by the tumor microenvironment", *Cancer Res.*, **56**:5754-5757 (1996).

21. Graeber, T. G., Osmanian, C., and Jacks, T., "Hypoxia-mediated selection of cells with diminished apoptotic potential in solid tumors", *Nature*, **379**:88-91 (1996).

22. Nordsmark, M., Overgaard, M., and Overgaard, J., "Pretreatment oxygenation predicts radiation response in advanced squamous cell carcinoma of the head and neck", *Radiother. Oncol.*, **41**:31-39 (1996).

23. Stadler, P., Becker, A., Feldmann, H. J., Hansgen, G., Dunst, J., Wurschmid, F., Molls, M., "Influence of the hypoxic subvolume on the survival of patients with head and neck cancer," *Int. J. Radiat. Oncol. Biol. Phys.*, **44**:749-754 (1999).

24. Dusenbery, K. E., McGuire, W. A., Holt, P. J., Carson, L. F., Fowler, J. M, Twiggs, L. B., Potish, R. A., "Erythropoietin increases hemoglobin during radiation therapy for cervical cancer", *Int. J. Radiat. Oncol. Biol. Phys.*, **29**:1079-1084 (1994).

25. Henke, M., Guttenberger, R., Baker, A., Pajonk, F., Pötter, R., Frommhold, H., "Erythropoietin for patients undergoing radiotherapy: A pilot study", *Radiother. Oncol.*, **50**:185-190 (1999).

26. Overgaard, J., Horsman, M., "Modification of hypoxia-induced radioresistance in tumors by the use of oxygen and sensitizers", *Semin. Radiat. Oncol.*, **6**:10-21 (1996).

27. Guttenberger, R., Lutterbach, J., Roth, A., Röser, S., Schindler, R., Henke, M., Frommhold, H., "Hemoglobin levels predict local regional control after postoperative radiotherapy for advanced head and neck cancer", *Eur. J. Cancer,* **33** (suppl):102-103 (1997).

28. Vaupel, P., Kelleher, D. K., and Thews, O, "Modulation of tumor oxygenation ", *Int. J. Radiat. Oncol. Biol. Phys.*, **42**:843-848 (1998).

29. Pederson, D., Sogaard, H., and Overgaard, J., "Prognostic value of pretreatment factors in patients with locally advanced carcinoma of the uterine cervix treated by radiotherapy alone", *Acta Oncol.*, **34**:787-795 (1995).

30. Ludwig, H., and Pecorelli, S., "Suboptimal hemoglobin levels: Do they impact patients and their therapy? Audience responses", *Semin. Oncol.*, **27**(suppl):18-19 (2000).

31. Vaupel, P., Schlenger, K., Knoop, C., and Höckel, M., "Oxygenation of human tumors: evaluation of tissue distribution in breast cancers by computerized O_2 tension measurements", *Cancer Res.*, **51**:3316-22 (1991).

32. Collingridge, D. R., Young, W. K., Vojnovic, B., Wardman, P., Lynch, E. M., Hill, S. A., and Chaplin, D. J., "Measurement of tumor oxygenation: a comparison between polarographic needle electrodes and a time-resolved luminescence-based optical sensor", *Radiat. Res.*, **147**:329-34 (1997).

33. Swartz, H. M., Bacic, G., Friedman, B., Goda, F., Grinberg, O., Hoopes, P. J., Jiang, J., Liu, K. J., Nakashima, T., O'Hara, J. A., and Walczak, T., "Measurement of pO_2 *in vivo*, including human subjects by electron paramagnetic resonance", *In*: P. Wagner (ed), *Oxygen Transport to Tissue XIV*, P. Plenum Press: New York, 221-223 (1994).

34. O'Hara, J. A., Goda, F., Liu, K. J., Bacic, G., Hoopes, P. J., and Swartz, H. M., "The pO_2 in a murine tumor after irradiation: an *in vivo* electron paramagnetic resonance oximetry study", *Radiat. Res.*, **144**:222-229 (1995).

35. Olive, P. L., and Durand, R. E., "Detection of hypoxic cells in a murine tumor with the use of the comet assay", *J. Natl. Cancer Inst.*, **84**:707-711 (1992).

36. Helmlinger, G., F., Yuan, F., Dellian, M., and Jain, R. K., "Interstitial pH and pO_2 gradients in solid tumors *in vivo*: high resolution measurements reveal lack of correlation", *Nature Medicine*, **3**(**2**):177-182 (1997).

37. Kavanagh, M. C., Sun, A., Hu, Q., and Hill, R. P., "Comparing techniques of measuring tumor hypoxia in different murine tumors: Eppendorf pO_2 histograph, [^{3}H] nitroimidazole binding and paired survival assays", *Radiat. Res.*, **145**:491-500.

38. Vaupel, P., Okunieff, P., Kallinowski, F., and Neuringer, L. J., "Correlation between ^{31}P NMR and tumor pO_2 in a murine fibrosarcoma", *Radiat. Res.*, **120**:477-493.

39. Mason, R. P., Constantinescu, A., Hunjan, S., Le, D., Hahn, E. W., Antich, P. P., Blum, C., and Peschke, P., "Regional tumor oxygenation and measurement of dynamic change", *Radiat. Res.*, **152**:239-245 (1999).

40. Hunjan, S., Mason, R. P., Constantinescu, A., Peschke, P., Hahn, E. W., and Antich, P. P., "Regional tumor oximetry: ^{19}F NMR spectroscopy of hexafluorobenzene", *Int. J. Radiat. Oncol. Biol. Phys.*, **41**:161-171 (1998).

41. Steen, R., "Characterization of tumor hypoxia by ^{31}P spectroscopy", *Am. J. Roentgenol*, **157**:243-248 (1991).

42. Lee, A. T., Glover, G. H., and Meyer, C. H., "Discrimination of large venous vessels in time-course spiral blood-oxygen-level-dependent magnetic resonance functional neuroimaging", *Magn. Reson. Med.*, **33**:745-754 (1995).

43. Ogawa, S., Menon, R. S., Tank, D. W., Kim, S., Ellermann, J. M., and Ugurbil, K., "Functional brain mapping by blood oxygenation level-dependent magnetic resonance imaging", *Biophys. J.*, **64**:803-812 (1993).

44. Mason, R. P., "Non-invasive physiology: ^{19}F NMR of perfluorocarbon", *Art. Cell Blood Sub. & Immob. Biotech.*, **22**:1141-1153 (1994).

45. Mason, R. P., Constantinescu, A., Hunjan, S., Le, D., Hahn, E. W., Antich, P. P., Blum, C., Peschke, P., "Regional tumor oxygenation and measurement of dynamic change", *Radiat. Res.*, **152**:239-245 (1999).

46. Hunjan, S., Mason, R. P., Constantinescu, A., Peschke, P., Hahn, E. W., Antich, P. P., "Regional tumor oximetry: ^{19}F NMR spectroscopy of hexafluorobenzene", *Int. J. Radiat. Oncol. Biol. Phys.*, **41**:161-171 (1998).

47. Chance, B., Nioka, S., Kent, J., McCully, K., Fountain, M., Greenfield, R., and Holtom, G., "Time resolved spectroscopy of hemoglobin and myoglobin in resting and ischemic muscle", *Anal. Biochem.*, **174**:698-707 (1988).

48. Homma, S., Fukunaga, T., and Kagaya, A., "Influence of adipose tissue thickness on near infrared spectroscopic signals in the measurement of human muscle", *J. Biomed. Opt.*, **1**(4): 418-424 (1996).

49. Ferrari, M., Wei, Q., Carraresi, L., De Blasi, R. A., and Zaccanti, G., "Time-resolved spectroscopy of the human forearm", *J. Photochem. Photobiol. B: Biol.* **16**:141-153 (1992).

50. Chance, B., Anday, E., Nioka, S., Zhou, S., Hong, L., Worden, K., Li, C., Murray, T., Ovetsky, Y., Pidikiti, D., and Thomas, R., "A novel method for fast imaging of brain function non-invasively with light", *Optics Express*, **2**(10): 411-423 (1998).

51. Wenzel, R., Obrig, H., Ruben, J., Villringer, K., Thiel, A., Bernarding, J., Dirnagl, U., and Villringer, A., "Cerebral blood oxygenation changes induced by visual stimulation in humans", *J. Biomed. Opt.*, **1**(4):399-404 (1996).

52. Cope, M., and Delpy, D. T., "A system for long term measurement of cerebral blood and tissue oxygenation in newborn infants by near infrared transillumination", *Med. Biol. Eng. Comp.*, **26**:289-294 (1988).

53. Steen, R. G., Wilson, D. A., Bowser, C., Rajan, S. S., Wehrle, J. P., and Glickson, J. D., "^{31}P NMR spectroscopic and near-infrared spectrophotometric studies of effects of anesthetics on *in vivo* RIF-1 tumors: relationship to tumor radiosensitivity", *NMR in Biomed.*, **2**:87-92 (1989).

54. Steen, R. G., Kitagishi, K., and Morgan, K., "*In vivo* measurement of tumor blood oxygenation by near-infrared spectroscopy: immediate effects of pentobarbital overdose or carmustine treatment", *J. Neuro-Oncol.*, **22**:209-220 (1994).

55. Sostman, H. D., Rockwell, S., Sylvia, A. L., Madwed, D., Cofer, G., Charles, H. C., Negro-Vilar, R., and Moore, D., "Evaluation of BA1112 rhabdomyosarcoma oxygenation with microelectrodes, optical spectrophotometry, radiosensitivity, and magnetic resonance spectroscopy", *Magn. Reson. Med.*, **20**:253-267 (1991).

56. Mariya, Y., Seinberg, F., Streffer, C., Fuhrmann, C., and Abe, Y., "Oxygenation status and tumor response during fractionated irradiation in two murine tumor cell lines of same origin but different intrinsic radiosensitivities", *Radiat. Med.*, **17**(2):175-179 (1999).

57. Hoon, D. B. S., "Circulating immune complexes in rats bearing 6-thioguanine-resistant variants of the 13762 mammary adenocarcinoma", *Cancer Res.* **44**:2406-2409 (1984).

58. Hahn, E. W., Peschke, P., Mason, R. P., Babcock, E. E., and Antich, P. P., "Isolated Tumor Growth in a Surgically Formed Skin Pedicle in the Rat: A New Tumor Model for NMR Studies", *Magn. Reson. Imaging*, **11**:1007-1017 (1993).

59. Adam, J. A., "General aspects of modeling tumor growth and immune response" in *A Survey of Models for Tumor-Immune System Dynamics*, Adam, J. A. and Bellomo, N., eds., *Birkhä user* (1996).

60. Steel, G. G., "Growth Kinetics of Tumors", *Clarendon Press, Oxford*, (1977).

61. Bassukas, I. D., "Comparative Gompertzian analysis of alterations of tumor growth patterns", *Cancer Res.*, **54**:4385-4392 (1994).

62. Hayes, C. E., Edelstein, W. A., Schenck, J. F., Mueller, O. M., and Eash, M., "An efficient, highly homogeneous radiofrequency coil for whole-body NMR imaging at 1.5 T", *J. Magn. Reson.*, **63**:622 - 628 (1985).

63. Pascone, R., Vullo, T., Farrelly, J., and Cahill, P. T., "Explicit treatment of mutual inductance in eight-column birdcage resonators", *Magn. Reson. Imag.*, **10**:401 - 410 (1992).

64. Cross, T. A., Muller, S., and Aue, W. P., "Radiofrequency resonators for high-field imaging and double-resonance spectroscopy", *J. Magn. Reson.*, **62**: 87 - 98 (1985).

65. Press, W. H., Teukolsky, S. A., Vetterling, W. T., and Flannery, B. P., *Numerical Recipes in C*, Cambridge University Press, 683 - 688 (1994).

66. Schneider, H. J., Dullenkopf, P., "Slotted tube resonator: a new NMR probe head at high observing frequencies", *Rev. Sci. Instrum.*, **48**:68 - 73 (1977).

67. Alderman, W., and Grant, D. M., "An efficient decoupler coil design which reduces heating in conductive samples in superconducting spectrometers", *J. Mag. Reson.*, **36**:447 - 451 (1979).

68. Ifeachor, E. C., Jervis, B. W., "Digital Signal Processing - A Practical Approach", *Addison-Wesley Publishing Company*, 374-483 (1993).

69. Mansfield, P., Pykett, I. L., "Biomedical and medical imaging by NMR", *J. Magn. Reson.*, **29**:355-373 (1978).

70. Barker, B. R., Mason, R. P., Peshock, R. M., "Echo planar imaging of perfluorocarbons", *Magn. Reson. Imaging*, **11**:1165-1173 (1993).

71. Barker, B. R., Mason, R. P., Bansal, N., Peshock, R. M., "Oxygen tension mapping by ^{19}F echo planar NMR imaging of sequestered perfluorocarbons", *JMRI*, **4**:595-602 (1994).

72. Le, D., Mason, R. P., Hunjan, S., Constantinescu, A., Barker, B. R., Antich, P. P., "Regional Tumor Oxygen Dynamics: ^{19}F PBSR EPI of Hexafluorobenzene", *Magn. Reson. Imaging*, **15**:971-981 (1997).

73. Sevick, E. M., Chance, B., Leigh, J., Nioka, S., and Maris, M., "Quantitation of time- and frequency-resolved optical spectra for the determination of tissue oxygenation", *Anal. Biochem.*, **195**:330-351 (1991).

74. Yunsong, Y., Liu, H., Li, X., and Chance, B., "Low-Cost Frequency-Domain Photon Migration Instrument for Tissue Spectroscopy, Oximetry, and Imaging", *Opt. Eng.*, **36(5)**:1562-1569 (1997).

75. "Data Acquisition Basics Manual", *National Instruments*, (1998).

76. Liu, H., Hielscher, A. H., Tittel, F. K., Jacques, S. L., Chance, B., "Influence of blood vessels on the measurement of hemoglobin oxygenation as determined by time-resolved reflectance spectroscopy", *Med. Phys.* **22**:1209-1217 (1995).

77. Zijlstra, W. G., Buursma, A., Meeuwsen-van der Roest, W. P., "Absorption spectra of human fetal and adult oxyhemoglobin, deoxyhemoglobin, carboxyhemoglobin, and methemoglobin", *Clin. Chem.*, **37(9)**:1 633-1638 (1991).

78. Liu, H., Matson, C. L., Lau, K., and Mapakshi, R. R., "Expeirmental validation of a backpropagation algorithm for three-dimensional breast tumor localization", *IEEE J. Select. Top. Quan. Elect.*, **5(4)**:1049-1057 (1999).

8. APPENDICES

----COPIES OF MANUSCRIPTS AND ABSTRACTS

Noninvasive investigation of blood oxygenation dynamics of tumors by near-infrared spectroscopy

Hanli Liu, Yulin Song, Katherine L. Worden, Xin Jiang, Anca Constantinescu, and Ralph P. Mason

The measurement of dynamic changes in the blood oxygenation of tumor vasculature could be valuable for tumor prognosis and optimizing tumor treatment plans. In this study we employed near-infrared spectroscopy (NIRS) to measure changes in the total hemoglobin concentration together with the degree of hemoglobin oxygenation in the vascular bed of breast and prostate tumors implanted in rats. Measurements were made while inhaled gas was alternated between 33% oxygen and carbogen (95% O_2, 5% CO_2). Significant dynamic changes in tumor oxygenation were observed to accompany respiratory challenge, and these changes could be modeled with two exponential components, yielding two time constants. Following the Fick principle, we derived a simplified model to relate the time constants to tumor blood-perfusion rates. This study demonstrates that the NIRS technology can provide an efficient, real-time, noninvasive means of monitoring the vascular oxygenation dynamics of tumors and facilitate investigations of tumor vascular perfusion. This may have prognostic value and promises insight into tumor vascular development. © 2000 Optical Society of America

OCIS codes: 170.1470, 170.3660, 170.4580, 170.5280, 290.1990, 290.7050.

1. Introduction

The presence and the significance of tumor hypoxia have been recognized since the 1950's. There is increasing evidence that tumor oxygenation is clinically important in predicting tumor response to radiation, tumor response to chemotherapy, overall prognosis, or all three. Hypoxic cells *in vitro* and in animal tumors *in vivo* are documented to be 3 times more resistant to radiation-induced killing compared with aerobic cells.[1] Recent studies show that hypoxia may have a profound impact on malignant progression and on responsiveness to therapy.[2,3] Numerous studies on tumor oxygen tension (pO_2) measurements have been conducted in recent years by use of a variety of methods, such as microelectrodes,[2] phosphors,[4] electron paramagnetic resonance,[5] or magnetic resonance imaging[6] (MRI).

Comparing needle-based, oxygen-sensitive electrodes or electron paramagnetic resonance and MRI for measuring pO_2 shows that the latter two offer the advantage of facilitating multiple repeated measurements to map pO_2 noninvasively. However, magnets are large, and the methods are not readily portable. A versatile method for monitoring intratumor oxygenation rapidly and noninvasively is therefore very desirable for tumor prognosis and tumor treatment planning.

In the near-infrared (NIR) region (700–900 nm) the major chromophores in tissue are oxygenated hemoglobin and deoxygenated hemoglobin, which differ in their light absorption. Measurements of the absorption of light travelling through the tissue under study allow us to evaluate or quantify blood oxygenation, such as the concentrations of oxygenated hemoglobin (HbO_2), and deoxygenated hemoglobin (Hb) and the hemoglobin saturation SO_2. In the past decade, three forms of NIR spectroscopy (NIRS) that use pulsed-laser light in the time domain, amplitude-modulated laser light in the frequency domain, and cw light in a dc form were developed for blood oxygenation quantification in tissue.[7] Significant investigations in both laboratory and clinical settings by use of NIRS were conducted for noninvasive, quantitative measurements and imaging of cerebral oxygenation[8–12] and blood oxygenation of exercised

muscle[13-17] *in vivo*. Although NIR techniques were used extensively in conjunction with cryospectrophotometry to investigate tumor blood-vessel oxygenation in biopsies,[18] only a few reports[19-22] were published on using the NIR techniques for monitoring tumor oxygenation *in vivo*. In principle, the theoretical model, i.e., the diffusion approximation to the photon transport theory, works well for only large and homogeneous media.[23,24] Accurate quantification of tumor oxygenation by use of the NIR approach is limited because of the considerable heterogeneity and the finite sizes of tumors.

It is understood and documented[25] that the NIR technique used for blood oxygenation monitoring is sensitive to vascular absorption in the measured organ. The NIR method is not limited to measurements of blood oxygenation in arteries (c.f., pulse oximetry) or in veins but interrogates blood in the entire vascular compartment, including capillaries, arterioles, and venules, i.e., the vascular bed. A variety of terms like cerebral oxygenation, tissue hemoglobin oxygenation, and mean hemoglobin oxygenation are used in the literature[7,24,26] to indicate this concept. Although tissue hemoglobin oxygenation is not rigorous because hemoglobin molecules are located in only blood, the term is used specifically to differentiate between the hemoglobin saturation in the tissue vascular bed, as measured by the NIR method, and the arterial hemoglobin saturation S_aO_2, as measured by a pulse oximeter.

The goal of this paper is to demonstrate the NIR technique as a real-time, noninvasive means of monitoring hemoglobin oxygenation dynamics, i.e., changes in the concentrations of total hemoglobin (Hb_t) and oxygenated hemoglobin (HbO_2), in the vascular bed of breast and prostate rat tumors in response to respiratory challenge. Compared with previous NIR studies of tumors *in vivo*, our approach has the following features: (1) The transmission mode, as opposed to the reflectance mode used by Hull *et al.*,[22] interrogates deeper regions (central parts) of the tumor. (2) Only two wavelengths, as opposed to the spectrum of 300–1100 nm used by Steen *et al.*,[21] are employed and provide a fast and low-cost instrument. (3) A source–detector separation of 1–2 cm interrogates a large tumor noninvasively, as opposed to the needlelike probe used by Steinberg *et al.*[20] More innovatively, on the basis of the experimental observation of tumor hemoglobin oxygenation dynamics, we developed a tumor hemoperfusion model that provides important insight into tumor blood perfusion.

This paper is organized as follows: In Section 2, we describe our animal model, the NIR instrument, and the algorithm for calculations of tumor blood oxygenation. In Section 3, we show experimental results measured from both breast and prostate tumors under respiratory interventions and calculate time constants for the hemoglobin oxygenation dynamics of the tumors. In Section 4, we develop a tumor hemoperfusion model to interpret the experimental data obtained in the tumor-intervention studies and to relate the time constants to tumor blood perfusion. Finally, in Section 5, we discuss the results, the future extensions, and the potential uses of the NIR technique as a novel diagnostic–prognostic tool for tumor therapy and cancer research.

2. Materials and Methods

A. Animal Model and Measurement Geometry

NF13762 breast tumor was implanted in adult female Fisher rats, and Dunning prostate adenocarcinoma R3327-AT1 was implanted in adult male Copenhagen rats. The tumors were grown in pedicles[27] on the forebacks of the rats until the tumors were approximately 1–2 cm in diameter. Rats were anesthetized with 200-μl ketamine hydrochloride (100 mg/ml) and maintained under general gaseous anesthesia with 33% inhaled O_2 (0.3 dm^3/min O_2, 0.6 dm^3/min N_2O, and 0.5% methoxyflurane) through a mask placed over the mouth and nose. Tumors were shaved to improve the optical contact for transmitting light. Body temperature was maintained with a warm-water blanket. In some cases, a fiber-optic pulse oximeter (Nonin, Inc., Model 8600V) that was manufacturer calibrated was placed on the hind foot to monitor arterial oxygenation S_aO_2, and a fiber-optic probe was inserted rectally to measure temperature. The tumor volume V (in centimeters cubed) was estimated as $V = (4\pi/3)[(L + W + H)/6]^3$, where L, W, and H are the three respective orthogonal dimensions.

Most measurements were performed with 33% oxygen as inhaled gas to achieve a stable baseline for a period of 5 to 15 min. The inhaled gas was then switched to carbogen (95% oxygen, 5% carbon dioxide) for at least 20 min and then switched back to 33% O_2 for approximately 15 min. The complete cycle lasted 1 hour. Sometimes repeated carbogen interventions were performed sequentially to evaluate the reproducibility of the time profiles of the tumors. In certain cases alternative gases were used, as defined in the results and figures, and some rats were sacrificed by KCl-induced cardiac arrest.

Figure 1 shows the measurement geometry: Horizontally, the delivering and the detecting fiber bundles were face to face in the transmittance mode, and both were in contact with the tumor surface without hard compression. The separation of the two bundle surfaces was between 1.0 and 2.5 cm, depending on the tumor size. Vertically, the two bundle tips (with diameters of 0.5 cm) were placed around the middle of the tumor. Thus the current setup of the probes provides an optimal geometry for the NIR light to interrogate deep tumor tissue with minimal interference from the foreback of the rat.

B. Near-Infrared Instrument and Data Analysis

As shown in Fig. 1, we used a homodyne frequency-domain photon-migration system[28,29] that was capable of determining the amplitude and the phase changes of amplitude-modulated light passing through tumors. In this setup a rf source modulates
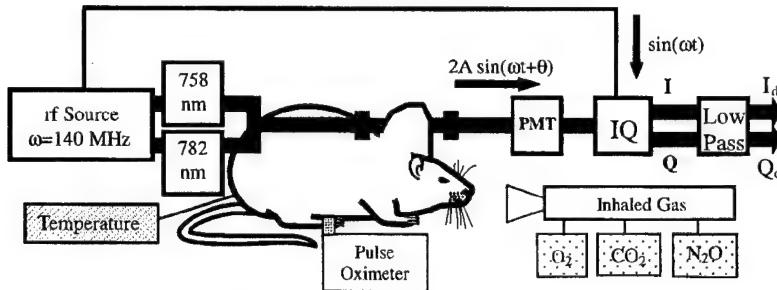
Fig. 1. Experimental setup of a one-channel, NIR, frequency-domain IQ instrument for tumor oxygenation measurement. PMT, photomultiplier tube for detecting light; IQ, in-phase and quadrature demodulator for retrieving amplitude and phase information; Low Pass, low-pass filter. The 5-mm-diameter fiber bundles deliver and detect the laser light through the tumor in transmittance geometry.

the light from two laser diodes (wavelengths of 758 and 782 nm) at 140 MHz. The laser light passes through a combined fiber-optic bundle, is transmitted through the tumor tissue, and is collected by a second fiber bundle. The light is then detected by a photomultiplier tube and demodulated with a commercially available in-phase and quadrature (IQ) demodulator chip into its I and Q components. After these components are put through a low-pass filter they can be used to calculate the amplitude and the phase changes caused by the tumor. These steps are expressed mathematically by

$$I(t) = 2A \sin(\omega t + \theta)\sin(\omega t)$$

$$= A \cos(\theta) - A \cos(\omega t + \theta) \xrightarrow[\text{pass}]{\text{low}} I_{\text{dc}}$$

$$= A \cos(\theta), \qquad (1)$$

$$Q(t) = 2A \sin(\omega t + \theta)\cos(\omega t)$$

$$= A \sin(\theta) + A \sin(\omega t + \theta) \xrightarrow[\text{pass}]{\text{low}} Q_{\text{dc}}$$

$$= A \sin(\theta), \qquad (2)$$

$$\theta = \tan^{-1}(Q_{\text{dc}}/I_{\text{dc}}), \qquad (3)$$

$$A = (I_{\text{dc}}^2 + Q_{\text{dc}}^2)^{1/2}, \qquad (4)$$

where A and θ are the amplitude and the phase of the detected light, respectively, and ω is the angular modulation frequency ($=2\pi \times 140$ MHz).

The two laser lights were time shared, and the controlling process and the data acquisition both interfaced through a 12-bit analog-to-digital board (Real Time Devices, Inc., Model AD2100) with a maximum sampling rate of 4 Hz.[28] However, slower sampling rates were used in measurements to compensate for experimental noise. Simple time averaging among a few adjacent data points was performed during data analysis to further decrease the noise. However, data smoothing was not applied for (1) calculating the experimental uncertainty (error bars) or (2) fitting the time constants to prevent the fast-changing component from being oversmoothed and overlooked. The pulse-oximeter data were not averaged because they were recorded manually and appear discrete compared

with the NIR data. The experimental uncertainties for arterial saturation and changes in hemoglobin concentrations were calculated by use of the baseline data taken over 5–10 min without respiratory perturbation to the rat. Nonlinear curve fitting based on the Marquardt algorithm[30,31] was performed by use of KaleidaGraph.[32] The software also provided the errors (or uncertainties) for each fitted parameter, the optimized χ^2 values, and the fitting correlation coefficient R, together with the goodness of the fit R^2.[33] The significance of changes was assessed on the basis of Fisher protected-least-significant-difference analysis of variance by use of Statview software.

C. Calculation for Changes in the Hemoglobin Concentration

It is well known that the NIRS of tissue can be used to determine the total hemoglobin concentration Hb_t and the hemoglobin oxygen saturation SO_2 of an organ *in vivo*.[7] When two NIR wavelengths are used (758 and 782 nm, in this case) it is assumed that tissue background absorbance is negligible and that the major chromophores in organs are oxygenated and deoxygenated hemoglobin molecules. In principle, because the IQ system can give both phase and amplitude values, we should be able to obtain absolute calculations of HbO_2, Hb, and SO_2.[7,28] However, given the tumor's small size and large spatial heterogeneity, it is very difficult to obtain such absolute quantification accurately with conventional algorithms[34] that are based on the diffusion approximation. Instead, on the basis of the modified Beer–Lambert law, we can use the amplitude of the light transmitted through the tumor to calculate concentration changes in HbO_2, Hb, and Hb_t (expressed as ΔHbO_2, ΔHb, ΔHb_t, respectively) of the tumor that are caused by respiratory intervention. These changes can be derived[25] and expressed as (see Appendix A for derivations and justifications)

$$\Delta\text{Hb} = \text{Hb(transient)} - \text{Hb(baseline)}$$

$$= \frac{\epsilon_{\text{HbO}_2}^{\lambda_1} \log\left(\dfrac{A_b}{A_t}\right)^{\lambda_2} - \epsilon_{\text{HbO}_2}^{\lambda_2} \log\left(\dfrac{A_b}{A_t}\right)^{\lambda_1}}{L(\epsilon_{\text{Hb}}^{\lambda_2} \epsilon_{\text{HbO}_2}^{\lambda_1} - \epsilon_{\text{Hb}}^{\lambda_1} \epsilon_{\text{HbO}_2}^{\lambda_2})}, \qquad (5)$$

$$\Delta HbO_2 = HbO_2(\text{transient}) - HbO_2(\text{baseline})$$

$$= \frac{\epsilon_{Hb}^{\lambda_2} \log\left(\frac{A_b}{A_t}\right)^{\lambda_1} - \epsilon_{Hb}^{\lambda_1} \log\left(\frac{A_b}{A_t}\right)^{\lambda_2}}{L(\epsilon_{Hb}^{\lambda_2} \epsilon_{HbO_2}^{\lambda_1} - \epsilon_{Hb}^{\lambda_1} \epsilon_{HbO_2}^{\lambda_2})}, \quad (6)$$

where ϵ_{Hb}^{λ} and $\epsilon_{HbO_2}^{\lambda}$ are extinction coefficients[35] of deoxygenated and oxygenated hemoglobin, respectively, at wavelength λ; the variable A_b is a constant amplitude of baseline; A_t is the transient amplitude under measurement; and L is the optical path length between the source and the detector.

Using the approach suggested by Cope and Delpy,[10] we can express L as $L = DPF \times d$, where d is the direct source–detector separation in centimeters and DPF is the ratio between the optical path length and the physical separation and is tissue dependent. The DPF for tumors has not been well studied; for simplicity, we assume the DPF to be 1 in our calculations. The justification for this simplification is given in Section 5. After substituting the extinction coefficients[35] at 758 and 782 nm in Eqs. (5) and (6) with values of $\epsilon_{Hb}^{758} = 0.359$, $\epsilon_{HbO_2}^{758} = 0.1496$, $\epsilon_{Hb}^{782} = 0.265$ and $\epsilon_{HbO_2}^{782} = 0.178$, respectively, in units of inverse millimoles times inverse centimeters, we arrive at

$$\Delta Hb = \frac{[7.34 \log(A_b/A_t)^{758} - 6.17 \log(A_b/A_t)^{782}]}{L},$$

$$(7)$$

$$\Delta HbO_2 =$$

$$\frac{[-10.92 \log(A_b/A_t)^{758} + 14.80 \log(A_b/A_t)^{782}]}{L},$$

$$(8)$$

$$\Delta Hb_t = \Delta(HbO_2 + Hb)$$

$$= \frac{[-3.58 \log(A_b/A_t)^{758} + 8.63 \log(A_b/A_t)^{782}]}{L},$$

$$(9)$$

where the units are in millimoles. Equations (7) and (8) permit the calculation of changes in Hb and HbO_2 that are due to respiratory challenge, respectively, whereas Eq. (9) quantifies a relative increase in the total hemoglobin concentration that is caused by the intervention. The last quantity also reflects a change in blood volume because it is proportional to the total Hb concentration.

3. Results

A. Instrument Drift Tests

The stability of the NIR instrument was tested in terms of baseline drift after a warm-up period of 30 min by use of a tissue phantom[25,36] with stable optical properties. Figure 2 shows an example of a phantom measurement that displays the variation of relative changes in apparent HbO_2 and Hb_t con-
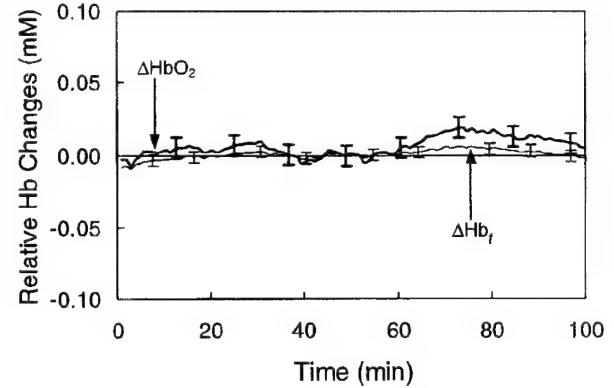
Fig. 2. Results of a drift test of the NIR instrument by use of a tissue phantom. The thicker solid curve represents relative changes in the oxygenated hemoglobin concentration, i.e., ΔHbO_2, and the thinner solid curve represents relative changes in the total hemoglobin concentration, i.e., ΔHb_t. ΔHbO_2 and ΔHb_t were calculated by use of Eqs. (8) and (9), respectively.

centrations, as calculated from Eqs. (8) and (9). In this example, the standard deviations over the entire period of 100 min were less than 0.007 and 0.004 mM, respectively, for ΔHbO_2 and ΔHb_t. Furthermore, we calculated uncertainties for both of these quantities on the basis of the propagation of errors, and the results are consistent with those shown in Fig. 2.

B. Breast Tumors

Figure 3(a) shows the results taken from a breast tumor (4.5 cm^3) with a source–detector separation of 1.8 cm. The data were smoothed, and the measurement uncertainties are shown at only discrete locations. The figure shows the relative changes in total hemoglobin concentration ΔHb_t and oxygenated hemoglobin concentration ΔHbO_2. The arterial Hb saturation was also obtained to show a relatively rapid change in arterial signals when the inhaled gas was switched from 33% O_2 to carbogen. Respiratory challenge caused a sharp rise in ΔHbO_2 ($p < 0.01$ after 1 min, $p < 0.0001$ by 1.5 min) that was followed by a further slow, gradual, but significant, increase over the next 25 min ($p < 0.001$). ΔHb_t also changed significantly ($p < 0.001$) within the first minute, but the total change was only approximately 10% of that of ΔHbO_2. Given the exponential appearance of the rising part of ΔHbO_2, we used single-exponential and double-exponential expressions to fit the data in the rising portion to better understand and quantify the dynamic features of ΔHbO_2. The unsmoothed data and the fitted curves are shown in Figure 3(b). The double exponential appears to give a much better fit, as is confirmed by the respective R values (0.98 versus 0.81). Time constants of 0.18 ± 0.02 min and 27.8 ± 3.9 min were obtained for fast and slow dynamic changes, respectively, in the tumor HbO_2 concentration.

Figure 4(a) was obtained from a second breast tumor (5.9 cm^3) with a source–detector separation of 1.6 cm. Here ΔHbO_2 increased rapidly after the ini-
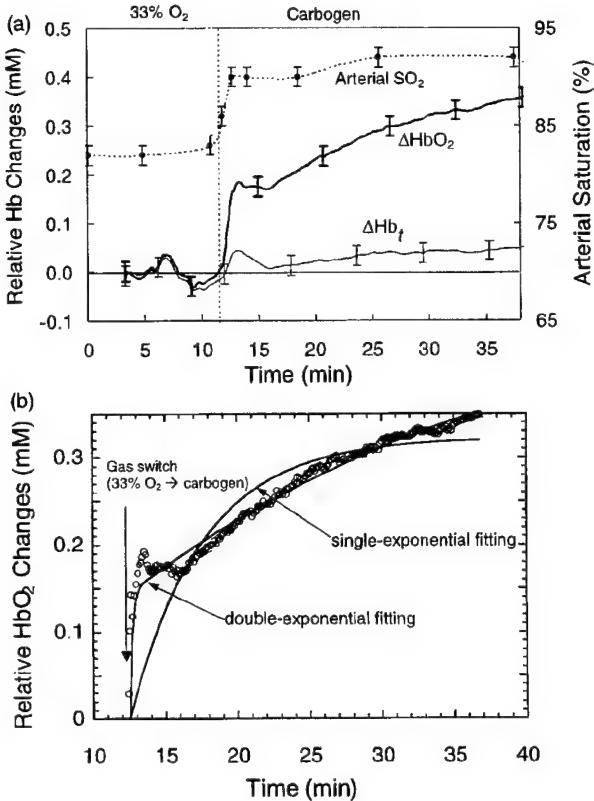
Fig. 3. (a) Results obtained with the NIR instrument from a 4.5-cm^3 rat breast tumor while the breathing gas was switched from 33% O_2 to carbogen. The thicker solid curve represents ΔHbO_2, the thinner solid curve represents ΔHb_t, and the dashed curve with the filled circles represents arterial saturation. (b) The unsmoothed data and the fitted curves: The solid curves represent the best fits to the ΔHbO_2 data at the rising portion. The best fit to the two exponential terms is $0.143\{1 - \exp[-(t - 12.5)/0.18]\} + 0.36\{1 - \exp[-(t - 12.5)/27.8]\}$, with $R = 0.98$, whereas the best fit with one exponential term is expressed as $0.322\{1 - \exp[-(t - 12.5)/5.1]\}$, with $R = 0.81$.

Fig. 4. (a) Results obtained with the NIR instrument from a 5.9-cm^3 rat breast tumor while the breathing gas was switched from 33% O_2 to carbogen. (b) The solid curves show the best fits to the HbO_2 data at the rising portion. In this case a double exponential with values of $0.09\{1 - \exp[-(t - 9.8)/0.8]\} + 0.16\{1 - \exp[-(t - 9.8)/3.0]\}$, with $R = 0.98$, and a single exponential with a value of $0.250\{1 - \exp[-(t - 9.8)/2.00]\}$, with $R = 0.97$, provided similarly good fits.

tial gas switch but did not exhibit the continued slow rise afterward. ΔHb_t was found to increase with carbogen inhalation, although the magnitude was smaller than that of ΔHbO_2 during the period of the intervention. Again, changes in ΔHbO_2 were modeled by a single-exponential term that yielded a time constant of 2.00 ± 0.04 min ($R = 0.97$) and by a double-exponential formula with two time constants of 0.8 ± 0.2 min and 3.0 ± 0.3 min ($R = 0.98$). In this case both expressions fit the data well, as shown in Fig. 4(b).

To demonstrate the reproducibility of the dynamic changes in response to respiratory challenge, we subjected one animal to repeat carbogen inhalation. Figure 5(a) shows measurements taken from a breast tumor (6.7 cm^3) with a source–detector separation of 2 cm. In this case air with 1.2% isoflurane (anesthetic) was used as the baseline instead of 33% O_2. This figure shows a very consistent pattern in two repeated time responses with a fast and a slow increase in ΔHbO_2. Here ΔHb_t shows a similar dy-

namic pattern, i.e., a rapid rise followed by a slow continuation. Figures 5(b) and 5(c) show the unsmoothed data together with the fitted curves for the rising portions of the two repeated increases in ΔHbO_2. Again, the double-exponential expression with two time constants produced much better fits than did the single-exponential term in both processes with two averaged time constants of τ_1 (mean) = 0.26 ± 0.11 min and τ_2 (mean) = 8.2 ± 1.8 min. Individual, respective time constants and coefficients are summarized in Table 1. Furthermore, single-exponential and double-exponential expressions were fitted to obtain time constants for the decay processes after the inhaled gas was switched repeatedly back to the baseline conditions. Similarly, the double-exponential expression fits the data better with two mean time constants of τ_1^{decay} (mean) = 0.17 ± 0.07 min and τ_2^{decay} (mean) = 12.2 ± 0.7 min for the two decay processes.

To further validate our experimental observations, we subjected some rats to cardiac arrest (with KCl) to observe the changes in HbO_2 and Hb_t on death. Figure 6 shows an example of cardiac arrest on a rat with
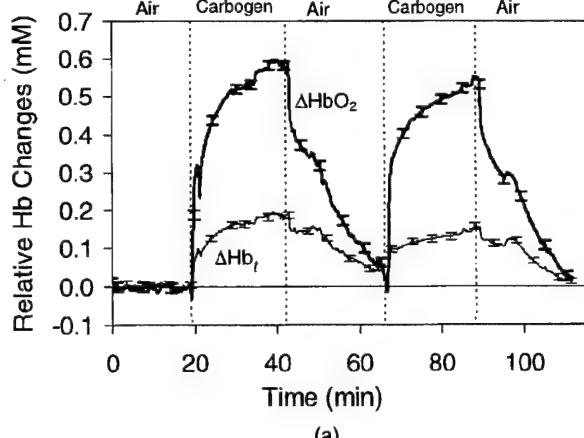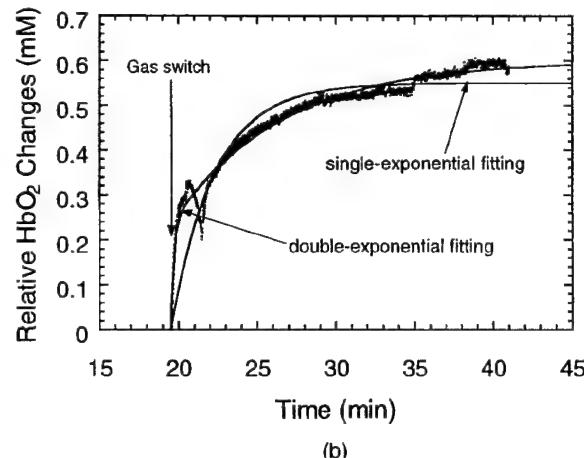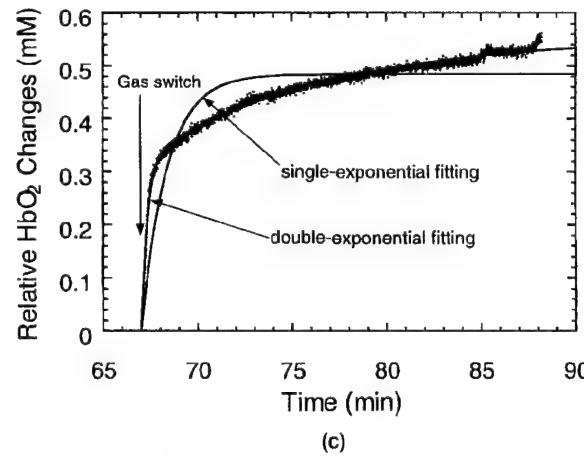
Fig. 5. (a) Relative changes in the HbO_2 detected with the NIR instrument from a rat breast tumor (6.7 cm³) while the breathing gas was alternated between air (21% O_2) and carbogen. The best fits to the HbO_2 data by use of both the double-exponential and the single-exponential expressions for (b) the first and (c) the second respiratory challenges are shown. The fitted equations that were obtained from (b) are $0.232\{1 - \exp[-(t - 19.5)/0.18]\} + 0.368\{1 - \exp[-(t - 19.5)/6.93]\}$, with $R = 0.98$, and $0.550\{1 - \exp[-(t - 19.5)/2.80]\}$, with $R = 0.89$, respectively. The fitted equations that were obtained from (c) were $0.321\{1 - \exp[-(t - 67)/0.332]\} + 0.233\{1 - \exp[-(t - 67)/9.47]\}$, with $R = 0.99$, and $0.485\{1 - \exp[-(t - 67)/1.38]\}$, with $R = 0.81$, respectively.

Table 1. Summary of the Vascular Oxygen Dynamics

| Tumor		Double-Exponential Fitting $\Delta HbO_2 = A_1[1 - \exp(-t/\tau_2)] + A_2[1 - \exp(-t/\tau_2)]$								Single-Exponential Fitting $\Delta HbO_2 = A_1[1 - \exp(-t/\tau)]$		
Type	Volume (cm³)	τ_1 (min)	τ_2 (min)	A_1 (mM)	A_2 (mM)	R^2	τ_1/τ_2	$\dfrac{\gamma_1}{\gamma_2} = \dfrac{A_1}{A_2}$	$f_1 = \dfrac{A_1/A_2}{\tau_1/\tau_2}$	τ (min)	A (mM)	R^2
Breast (Fig. 3)	4.5	1.8 ± 0.02	27.8 ± 3.9	0.143 ± 0.003	0.36 ± 0.03	0.96	0.006 ± 0.001	0.40 ± 0.03	61.35 ± 0.01	5.1 ± 0.3	0.322 ± 0.005	0.66
Breast (Fig. 4)	5.9	0.8 ± 0.2	3.0 ± 0.3	0.09 ± 0.02	0.16 ± 0.02	0.96	0.27 ± 0.07	0.56 ± 0.14	2.11 ± 0.18	2.00 ± 0.04	0.250 ± 0.001	0.94
Breast (Fig. 5)	6.7	0.18 ± 0.01	6.93 ± 0.09	0.232 ± 0.002	0.368 ± 0.002	0.97	0.026 ± 0.001	0.63 ± 0.01	24.27 ± 0.01	2.80 ± 0.03	0.550 ± 0.001	0.80
	6.7	0.332 ± 0.003	9.47 ± 0.12	0.321 ± 0.001	0.233 ± 0.001	0.99	0.035 ± 0.001	1.38 ± 0.01	39.30 ± 0.01	1.38 ± 0.02	0.485 ± 0.001	0.66
Prostate (Fig. 7)	8.2	0.265 ± 0.007	6.02 ± 0.15	0.090 ± 0.001	0.064 ± 0.001	0.93	0.044 ± 0.001	1.41 ± 0.03	31.95 ± 0.01	1.13 ± 0.02	0.140 ± 0.001	0.67
Prostate (Fig. 8)	10.8	0.3 ± 4.5	15.6 ± 3.1	0.004 ± 0.01	0.38 ± 0.03	0.94	0.02 ± 0.20	0.01 ± 0.03	0.6 ± 1.2	14.8 ± 1.6	0.37 ± 0.02	0.94
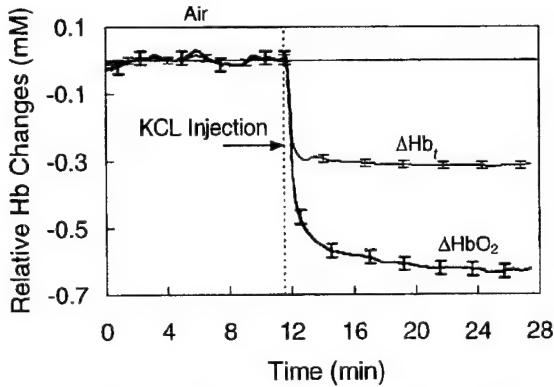
Fig. 6. Influence of KCl-induced cardiac arrest on the values of HbO_2 and Hb_t of a breast tumor (5.3 cm^3), while the rat was breathing air.

a breast tumor (5.3 cm^3). Both ΔHb_t and ΔHbO_2 dropped significantly, immediately after KCL was admitted intravenously. Within 1 min ΔHb_t reached a plateau, whereas ΔHbO_2 decreased rapidly within the first 30 s and then was followed by a slow prolongation.

C. Prostate Tumors

Figure 7(a) was obtained from a large prostate tumor (8.2 cm^3). In common with the breast tumors, ΔHbO_2 showed a rapid initial increase that was followed by a slower continuation. ΔHb_t increased rapidly and then reached a plateau. Figure 7(b) shows that the double-exponential equation fits the unsmoothed data better ($R = 0.96$) than does the single-exponential term ($R = 0.82$). Here the fast and the slow time constants are 0.265 ± 0.007 min and 6.02 ± 0.15 min, respectively.

Figure 8(a) was obtained from another large prostate tumor (10.8 cm^3 with a source–detector separation of 2.5 cm). Here ΔHbO_2 displayed a gradual increase throughout the entire period of carbogen inhalation, whereas the increase in ΔHb_t was considerably delayed. Variations in arterial hemoglobin saturation S_aO_2 are also shown and were very rapid in comparison with ΔHbO_2, in common with Fig. 3. ΔHbO_2 dropped rapidly when the inhaled gas was switched back from carbogen to 33% O_2. Both the single-exponential and the double-exponential expressions were used to obtain time constants for the rising portion of ΔHbO_2 that was due to carbogen intervention. In this case both expressions gave equally good fits, as shown in Fig. 8(b) and Table 1. For the decay process, we obtained $\tau_1^{decay} = 0.6 ± 0.2$ min and $\tau_2^{decay} = 6.6 ± 1.7$ min with $R = 0.94$ for the double-exponential fitting, whereas the single-exponential fitting resulted in $\tau = 2.8 ± 0.4$ min with $R = 0.88$. For comparison the rat was also challenged with 100% O_2.

In summary, we observed dynamic changes in HbO_2 that were due to carbogen intervention for both breast and prostate tumors. In most cases these changes were modeled better by a double-exponential
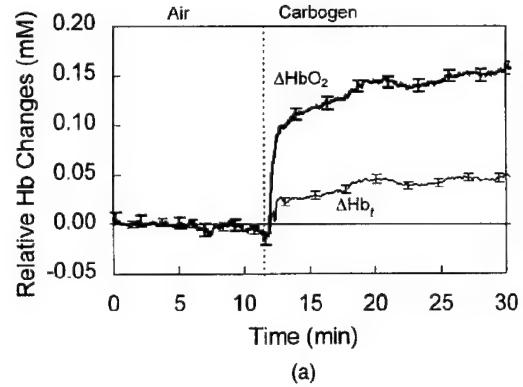

(a)
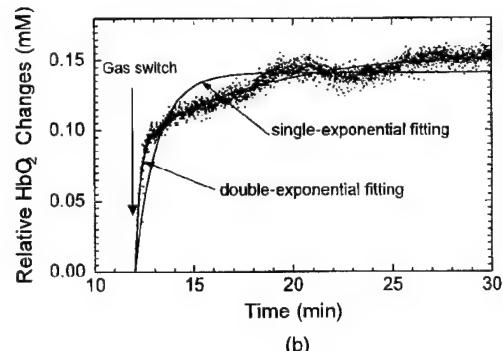
(b)

Fig. 7. (a) Influence of respiratory challenges (switching from air to carbogen) on the values of HbO_2 and Hb_t of a large rat prostate tumor (8.2 cm^3). (b) The best-fitted equations are $0.090\{1 - \exp[-(t - 12)/0.265]\} + 0.064\{1 - \exp[-(t - 12)/6.02]\}$, with $R = 0.96$, and $0.140\{1 - \exp[-(t - 12)/1.13]\}$, with $R = 0.82$, for the double-exponential and the single-exponential expressions, respectively.

expression with a fast and a slow time constant than they were by a single-exponential fitting. Dynamic changes in arterial saturation preceded those in HbO_2. The detailed parameters regarding tumor size, fitted time constants, corresponding magnitudes, and R^2 are listed in Table 1.

4. Model for the Blood Oxygenation Dynamics of Tumors

As was shown in Section 3, the temporal changes in HbO_2 caused by respiratory challenge can be fitted with an exponential equation that has either one or two time constants (fast and slow). In this section, we further derive and simplify a hemoperfusion model to interpret these time constants and to correlate the experimental findings with the physiology of the tumors.

To develop the model, we follow an approach used to measure regional cerebral blood flow (rCBF) with diffusible radiotracers, as originally developed by Kety[37] in the 1950's. The basic model was modified in a variety of ways to adapt it to positron emission tomography studies.[38,39] By analogy, we can evaluate tumor hemodynamics such as tumor blood flow (perfusion) by using the respiratory-intervention gas as a tracer.
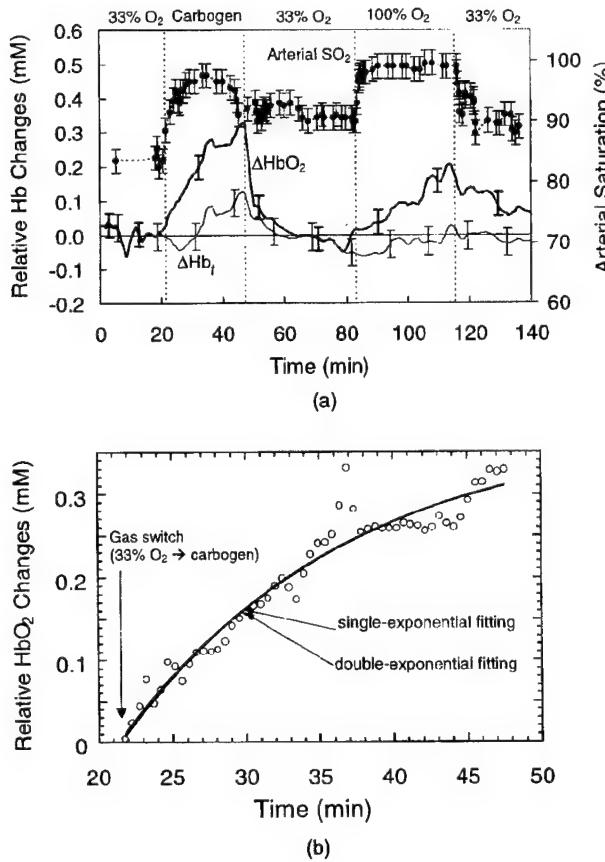
Fig. 8. (a) Variations in S_aO_2, ΔHbO_2, and Hb_t of which the latter two were detected with the NIR instrument, from a large rat prostate tumor (10.8 cm³) during respiratory challenge. (b) The solid curves represent the best fits to the ΔHbO_2 data at the rising portion during carbogen inhalation. The fitted equations are $0.004\{1 - \exp[-(t - 21.5)/0.3]\} + 0.38\{1 - \exp[-(t - 21.5)/15.6]\}$ and $0.37\{1 - \exp[-(t - 21.5)/14.8]\}$ for the double-exponential and the single-exponential expressions, respectively, with $R = 0.97$ for both.

In general, the Fick principle can be stated as follows[38]: The rate of change of tracer concentration in a regional area of an organ equals the rate at which the tracer is transported to the organ in the arterial circulation minus the rate at which it is carried away into the venous drainage, i.e.,

$$\frac{dC_t}{dt} = f(C_a - C_v), \qquad (10a)$$

where f is the blood flow (or perfusion rate), C_t is the tracer concentration in tissue, and C_a and C_v are the time-varying tracer concentrations in the arterial input and the venous drainage, respectively. C_a can be measured from a peripheral artery, but C_v is relatively difficult to obtain regionally. Therefore a brain–blood partition coefficient, $\lambda = C_t/C_v$, was developed by Kety, and Eq. (10a) becomes[37]

$$\frac{dC_t}{dt} = f\left(C_a - \frac{C_t}{\lambda}\right). \qquad (10b)$$

In Eq. (10b), f and λ are constants, whereas C_t is a time-dependent variable that is written as $C_t(t)$. In principle, the arterial-tracer concentration C_a is a time-varying quantity. If a certain concentration of the arterial tracer is administrated continuously starting at time 0, C_a can be expressed mathematically as a constant value of $C_a(0)$ after time 0. Then Eq. (10b) can be solved as

$$C_t(t) = \lambda C_a(0)[1 - \exp(-ft/\lambda)]. \qquad (11)$$

Equation (11) indicates that, at time t after the onset of tracer administration, the local tissue (traditionally brain) $C_t(t)$ concentration depends on the blood flow f, the arterial time–activity curve $C_a(0)$, and the partition coefficient λ.

In response to respiratory intervention, a sudden small change is introduced into the arterial O_2 saturation S_aO_2, and the resulting increase in arterial HbO_2 concentration (ΔHbO_2^{artery}) can be considered as an intravascular tracer.[40] Following Kety's method and assuming that changes in dissolved O_2 are negligible,[40] we have

$$\frac{d}{dt}(\Delta HbO_2^{vasculature}) =$$

$$f\left(\Delta HbO_2^{artery} - \frac{\Delta HbO_2^{vasculature}}{\gamma}\right).$$

$$(12)$$

where f still represents blood flow (or perfusion rate) and γ is defined as a vasculature coefficient of the tumor. The coefficient γ is the ratio of the HbO_2 concentration change in the vascular bed to that in veins and equals $(\Delta HbO_2^{vasculature})/(\Delta HbO_2^{vein})$. This definition implies that a change in the venous blood oxygenation ΔHbO_2^{vein} is proportional to a change in the Hb oxygenation in the vascular bed, $\Delta HbO_2^{vasculature}$.

In Eq. (12), f and γ are constants, whereas $\Delta HbO_2^{vasculature}$ is a time-dependent variable. By analogy to Eq. (11), $\Delta HbO_2^{vasculature}$ can be solved rigorously given a constant input H_0 for ΔHbO_2^{artery} after time 0. Our data (Figs. 3 and 8) demonstrate that changes in the arterial HbO_2 (S_aO_2) are much faster than in the vascular bed. Then solving Eq. (12) leads to

$$\Delta HbO_2^{vasculature}(t) = \gamma H_0[1 - \exp(-ft/\gamma)]. \qquad (13)$$

Equation (13) indicates that, at time t after the onset of respiratory intervention, the change in oxygenated hemoglobin concentration in the tumor vasculature $\Delta HbO_2^{vasculature}(t)$ depends on the blood perfusion rate f, the arterial oxygenation input H_0, and the vasculature coefficient of the tumor γ.

As indicated by Eq. (8), our NIR instrument is able to measure an increase in the vascular HbO_2 concentration $\Delta HbO_2^{vasculature}$. Equation (13) gives an exponential of the same form as that used to fit our experimental data, indicating that the measured
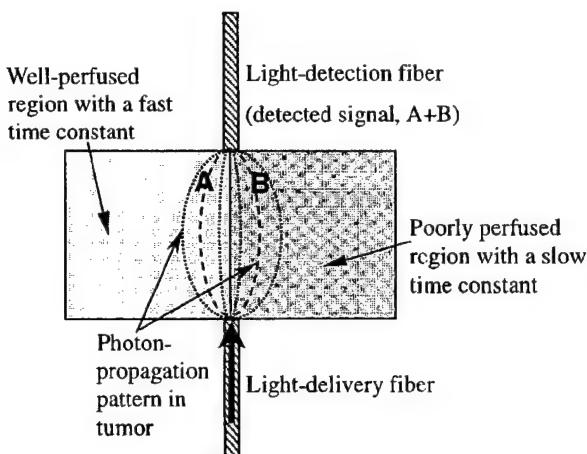
Fig. 9. Schematic diagram showing (1) a tumor model with two vascular perfusion regions, (2) the source and the detector fibers and their geometry with respect to the tumor model, and (3) the light patterns that propagate in the tumor tissue. A represents a portion of the detected signal, which interrogates the well-perfused region, and B represents another portion of the detected signal, which passes mainly through the poorly perfused region. We have assumed that the total detected signal is the sum of A and B.

time constant is associated with the blood perfusion rate f and the vasculature coefficient γ of the tumor in the measured area. If the measured volume involves two distinct regions, we then involve with two different blood-perfusion rates f_1 and f_2, two different vasculature coefficients γ_1 and γ_2, or all four. Here it is reasonable to assume that the measured signal results from both regions, as illustrated in Fig. 9. Consequently, Eq. (13) can be modified with a double-exponential expression and two time constants as

$$
\begin{aligned}
\Delta HbO_2{}^{\text{vasculature}}(t) &= \gamma_1 H_0[1 - \exp(-f_1 t/\gamma_1)] \\
&\quad + \gamma_2 H_0[1 - \exp(-f_2 t/\gamma_2)] \\
&= A_1[1 - \exp(-f_1 t/\gamma_1)] \\
&\quad + A_2[1 - \exp(-f_1 t/\gamma_2)], \quad (14)
\end{aligned}
$$

where f_1 and γ_1 are the blood-perfusion rate and the vasculature coefficient, respectively, in region 1, f_2 and γ_2 are the same for region 2, $A_1 = \gamma_1 H_0$, and $A_2 = \gamma_2 H_0$. The two time constants are equal to $\tau_1 = \gamma_1/f_1$ and $\tau_1 = \gamma_2/f_2$. Then, if A_1, A_2, and the two time constants are determined from our measurements, we arrive at the ratios for the two vasculature coefficients and the two blood-perfusion rates:

$$
\frac{\gamma_1}{\gamma_2} = \frac{A_1}{A_2}, \qquad \frac{f_1}{f_2} = \frac{A_1/A_2}{\tau_1/\tau_2}. \quad (15)
$$

With these two ratios, we can obtain insight into the tumor vasculature and blood perfusion. For example, a ratio of γ_1/γ_2 near 1 from a measurement implies that the vascular structure of the measured tumor volume is rather uniform. Then the coexistence of two time constants reveals two mechanisms of regional blood perfusion in the tumor. A large time constant implies slow perfusion through a poorly perfused area, whereas a small time constant indicates fast perfusion through a well-perfused area. In the meantime, the ratio of the perfusion rates in these two areas can also be obtained quantitatively. Furthermore, a ratio of $\gamma_1/\gamma_2 > 1$ (i.e., $A_1/A_2 > 1$) means that the measured signal results more from region 1 than from region 2 within the measured tumor volume. Therefore, by studying tumor blood oxygenation dynamics and obtaining time constants together with their amplitudes, we can gain important information on regional blood perfusion and vascular structures of the tumor within the measured volume.

Our experimental data (Table 1) reveal that all the measurements can be fitted with the double-exponential model equivalently to or better than the single-exponential fitting. Ratios of τ_1/τ_2, γ_1/γ_2, and f_1/f_2 are also shown in Table 1 for respective cases.

5. Discussion

Using NIRS, we have measured relative changes in Hb_t and HbO_2 in breast and prostate rat tumors in response to respiratory intervention. We have observed that respiratory challenge caused the HbO_2 concentration to rise promptly and significantly in both breast and prostate tumors but that the total concentration of hemoglobin sometimes increased and sometimes remained unchanged. The dynamic changes of tumor oxygenation can be modeled by either one exponential term with a slow time constant or two exponential terms with fast and slow time constants. This relation suggests that there may be two vascular mechanisms in the tumor that are detected by the NIRS measurement. As indicated by Eqs. (13) and (14), these time constants are inversely proportional to the blood-perfusion rates of the measured volumes of the tumors. Based on the double-exponential model, determination of the two time constants and their corresponding amplitudes allows us to determine the relations between the two perfusion rates and between the vascular structures, as expressed in Eq. (15). Further investigation with more measured quantities may lead to quantification of each parameter individually by use of the NIR technique.

To develop a model for interpreting the NIR data taken during carbogen inhalation, we have defined a vasculature coefficient γ. It is a proportionality factor between $\Delta HbO_2{}^{\text{vein}}$ and $\Delta HbO_2{}^{\text{vasculature}}$, i.e., $\Delta HbO_2{}^{\text{vein}} = \Delta HbO_2{}^{\text{vasculature}}/\gamma$. We expect that γ depends on (1) the oxygen consumption and (2) the capillary density of the tumor. If the oxygen consumption, the capillary density, or both of the tumor are large, changes in the venous HbO_2 concentration will be small; if the oxygen consumption, the capillary density, or both of the tumor are small, changes in the venous HbO_2 concentration will be large. Further studies are necessary to learn more about this coefficient and to confirm our speculation.

Our current NIR system allows us to quantify the

ratio of γ/f by using the single-exponential model or to quantify the ratios of γ_1/γ_2 and f_1/f_2 by using the double-exponential model. We can obtain important information on the blood perfusion of the tumor: a large time constant usually represents slow blood perfusion, whereas a small time constant indicates fast blood perfusion. The coexistence of two time constants implies a combination of well-perfused and poorly perfused mechanisms of blood perfusion. Indeed, some tumor lines have only 20% to 85% of vessels perfused.[41] Furthermore, tumor structures and oxygen distribution[6,42] are highly heterogeneous. Therefore it is likely that our measurement detects a well-perfused region, or a poorly perfused region, or a mixture of both in the tumor, depending on the position or the location of the source and the detector of the NIR instrument.

Hull et al.[22] reported carbogen-induced changes in rat mammary tumor oxygenation by using spatially resolved NIRS. To compare our results to theirs, we applied our curve-fitting procedure to their published hemoglobin saturation curve and obtained a time constant of 0.27 min (or 16 s) for the rising edge, which is consistent with our fast component. Their data do not show a slow component, suggesting that their measurement was dominated by active tumor vasculature. This difference may be explained as follows:

(1) The tumor volume mentioned in the paper by Hull et al.[22] was approximately 1.5 cm^3, much smaller than the volumes of the tumors that we measured (in Figs. 3 to 8, the largest tumor was 10.8 cm^3, whereas the smallest tumor was 4.5 cm^3).

(2) Their measurement was in reflectance geometry with multiple detectors located at distances 1 to 20 mm away from the source, and in the calculation the tumor was assumed to be homogenous in order to use diffusion theory. Thus their measurement was more sensitive to the superficial area of the tumor, emphasizing the tumor periphery, which is often better vascularized than the central part of the tumor.[42,43]

The fast component observed in our tumors is consistent with the rapid changes detected in S_aO_2 in the leg as measured by use of the pulse oximeter, providing further evidence that this relates to the well-vascularized, highly perfused region of the tumor.

The data shown in Fig. 8 in this paper are representative of the measurement of a poorly perfused region in which the measured tumor was large and the portion for the fast oxygenation response was small. The data given in Figs. 3–5 and 7 resulted from a mixture of well-perfused and poorly perfused areas in the tumors and exhibited a mixture of fast and slow oxygenation responses to hyperoxygen conditions. It is reasonable to expect that larger tumors have more poorly perfused regions than do smaller tumors. The time constant of the slow component observed here approaches that observed previously for changes in tissue pO$_2$ in an AT1 prostate tumor

measured by use of ^{19}F nuclear magnetic resonance spectroscopy to interrogate interstitial oxygenation.[44] In general, well-oxygenated tumor regions had a large and rapid response to respiratory challenge, whereas poorly oxygenated regions were much more sluggish.[45] One would indeed expect changes in vascular oxygenation to precede changes in the tissue, and combined investigations by NIRS and nuclear magnetic resonance spectroscopy in the future will provide further insight into the delivery of oxygen to tumors.

Dynamic changes in vascular oxygenation have been assessed previously by several other techniques. Following the infusion of Green 2W dye intravenously into EMT-6 tumor-bearing mice, Vinogradov et al.[4] were able to image changes in the surface vascular pO$_2$. On switching from air to carbogen inhalation, they observed a very rapid increase in pO$_2$ with a rate similar to the fast component, which we have seen here. Although the phosphorescence method provides vascular pO$_2$, NIR methods generally provide HbO$_2$ or SO$_2$ because there is some uncertainty in the local affinity of hemoglobin for tumor oxygen: the pO$_2$–SO$_2$ dissociation curve is subject to pH, temperature, and other allosteric effectors, such as 2,3-diphosphoglycerate in the immediate milieu. A promising new approach is the blood-oxygen-level–dependent (BOLD) contrast ^{1}H MRI, which is sensitive to vascular perturbations. Robinson et al.[46] explored the response to respiratory challenge in various tumors and showed reversible regional changes on switching from air to carbogen inhalation. In common with our NIR data, their changes were often biphasic with a large change occurring within the first 2 min and followed by slower increases.[46] However, interpreting the BOLD MRI results is complicated by variations in vascular volume and flow, and there is no direct measure of HbO$_2$ in tumors.

The time constants are not source–detector separation sensitive. Equations (8) and (9) have demonstrated that ΔHbO_2 and ΔHb_t are proportional to $1/d$, where d is the source–detector separation. This relation indicates that a different d value will only stretch or compress the entire temporal profile of ΔHbO_2, but it does not change the transient behavior of the time response. The same argument can apply to the DPF. In this study, we have assumed a DPF ratio of 1 for simplicity. If the DPF value is larger than 1, the values of ΔHbO_2 and ΔHb_t will decrease by a factor of DPF. But this modification does not affect the time constants τ_1 and τ_2, which constitute the dynamic responses of ΔHbO_2 of the tumors to respiratory intervention.

Given the evidence for intratumoral heterogeneity from MRI[6,46] and histology,[47] we believe it will be important to advance our NIR system to have multiple sources, multiple detectors, or both to study not only dynamic but also spatial aspects of blood oxygenation in tumor vasculature. Nonetheless, we believe the preliminary results described here are a proof of principle for the technique, laying a foundation for more extensive tests to correlate tumor size

where d is the source–detector separation and μ_a and μ_s' are the absorption and the reduced scattering coefficients, respectively. Because in the NIR region the μ_s' of tissue is not sensitive to either wavelength or perturbation, we assume that a change in L results from only a change in μ_a, which is both wavelength and perturbation dependent. With this assumption, Eq. (A7) leads to

$$\frac{\Delta L}{L} = -\frac{1}{2}\frac{\Delta\mu_a}{\mu_a}. \tag{A8}$$

Equation (A8) allows us to determine the relative errors of $\Delta L/L$ that are caused by (a) the wavelength dependence of μ_a and (b) the perturbation dependence of μ_a in the tumor. For case (a), we calculated this error by using

$$\frac{\mu_a^{758} - \mu_a^{782}}{2\mu_a^{758}}$$

under the baseline and the perturbed conditions; for case (b), we employed

$$\frac{\mu_a^\lambda \text{ (transient)} - \mu_a^\lambda \text{ (baseline)}}{2\mu_a^\lambda \text{ (baseline)}}$$

at both $\lambda = 758$ nm and $\lambda = 782$ nm for the error calculation. The μ_a values used here were taken from Hull et al.[22] Although the rat tumor used in their study was different from ours, the absorption coefficients of the tumors should be in a similar order and follow a similar dynamic trend. The calculation shows that, with 758 and 782 nm under carbogen perturbation, the maximum value of $\Delta L/L$ is 12%. This result implies that the assumption of a constant path length that was used for Eqs. (5) and (6) gives rise to a maximal relative error of 12% in L.

On the basis of Eqs. (5) and (6) [or Eqs. (7) and (8)], we arrive at $\Delta X/X = -\Delta L/L$, where X can be ΔHbO_2, ΔHb, or ΔHb_t. Thus the assumption of a constant path length leads to a maximal relative error of 12% for the magnitude of the changes that we detected with regard to respiratory challenge. Although 12% is not completely negligible, the measurement and the calculation with the assumption of a constant path length are still worthwhile. Such an approach makes it possible, as a first-order approximation, to quantify the ΔHb_t and the ΔHbO_2 of tumors under respiratory intervention, providing deep insight into tumor vascular phenomena and mechanisms of modulating tumor physiology for therapeutic enhancement.

References

1. L. Gray, A. Conger, M. Ebert, S. Hornsey, and O. Scott, "The concentration of oxygen dissolved in tissues at time of irradiation as a factor in radio-therapy," Br. J. Radiol. **26**, 638–648 (1953).
2. M. Höckel, K. Schlenger, B. Aral, M. Mitze, U. Schaffer, and P. Vaupel, "Association between tumor hypoxia and malignant progression in advanced cancer of the uterine cervix," Cancer Res. **56**, 4509–4515 (1996).
3. T. Y. Reynolds, S. Rockwell, and P. M. Glazer, "Genetic instability induced by the tumor microenvironment," Cancer Res. **56**, 5754–5757 (1996).
4. S. A. Vinogradov, L.-W. Lo, W. T. Jenkins, S. M. Evans, C. Koch, and D. F. Wilson, "Noninvasive imaging of the distribution of oxygen in tissues in vivo using near-infrared phosphors," Biophys. J. **70**, 1609–1617 (1996).
5. J. A. O'Hara, F. Goda, K. J. Liu, G. Bacic, P. J. Hoopes, and H. M. Swartz, "The pO$_2$ in a murine tumor after irradiation: an in vivo electron paramagnetic resonance oximetry study," Radiat. Res. **144**, 222–229 (1995).
6. R. P. Mason, A. Constantinescu, S. Hunjan, D. Le, E. W. Hahn, P. P. Antich, C. Blum, and P. Peschke, "Regional tumor oxygenation and measurement of dynamic changes," Radiat. Res. **152**, 239–245 (1999).
7. D. T. Delpy and M. Cope, "Quantification in tissue near-infrared spectroscopy," Philos. Trans. R. Soc. London B **952**, 649–659 (1997).
8. M. Fabiani, G. Gratton, and P. M. Corballis, "Noninvasive near-infrared optical imaging of human brain function with subsecond temporal resolution," J. Biomed. Opt. **1**, 387–398 (1996).
9. R. Wenzel, H. Obrig, J. Ruben, K. Villringer, A. Thiel, J. Bernarding, U. Dirnagl, and A. Villringer, "Cerebral blood oxygenation changes induced by visual stimulation in humans," J. Biomed. Opt. **1**, 399–404 (1996).
10. M. Cope and D. T. Delpy, "A system for long-term measurement of cerebral blood and tissue oxygenation in newborn infants by near-infrared transillumination," Med. Biol. Eng. Comput. **26**, 289–294 (1988).
11. B. Chance, E. Anday, S. Nioka, S. Zhou, L. Hong, K. Worden, C. Li, T. Murray, Y. Ovetsky, D. Pidikiti, and R. Thomas, "A novel method for fast imaging of brain function, noninvasively, with light," Opt. Express **2**, 411–423 (1998), http://www.epubs.osa.org/opticsexpress.
12. A. M. Siegel, J. A. Marota, J. Mandeville, B. Rosen, and D. A. Boas, "Diffuse optical tomography of rat brain function," in Optical Tomography and Spectroscopy of Tissue III, B. Chance, R. R. Alfano, and B. J. Tromberg, eds., Proc. SPIE **3597**, 252–261 (1999).
13. S. Homma, T. Fukunaga, and A. Kagaya, "Influence of adipose tissue thickness on near-infrared spectroscopic signals in the measurement of human muscle," J. Biomed. Opt. **1**, 418–424 (1996).
14. M. Ferrari, Q. Wei, L. Carraresi, R. A. De Blasi, and G. Zaccanti, "Time-resolved spectroscopy of the human forearm," J. Photochem. Photobiol. B: Biol. **16**, 141–153 (1992).
15. M. Ferrari, R. A. De Blasi, S. Fantini, M. A. Franceschini, B. Barbieri, V. Quaresima, and E. Gratton, "Cerebral and muscle oxygen saturation measurement by a frequency-domain near-infrared spectroscopic technique," in Optical Tomography, Photon Migration, and Spectroscopy of Tissue and Model Media: Theory, Human Studies, and Instrumentation, B. Chance and R. R. Alfano, eds., Proc. SPIE **2389**, 868–874 (1995).
16. H. Long, G. Lech, S. Nioka, S. Zhou, and B. Chance, "CW imaging of human muscle using near-infrared spectroscopy," in Advances in Optical Imaging and Photon Migration, J. G. Fujimoto and M. S. Patterson, eds., Vol. 21 of OSA Trends in

Optics and Photonics Series (Optical Society of America, Washington, D.C., 1998), pp. 256–259.

17. B. Chance, S. Nioka, J. Kent, K. McCully, M. Fountain, R. Greenfield, and G. Holtom, "Time-resolved spectroscopy of hemoglobin and myoglobin in resting and ischemic muscle," Anal. Biochem. **174,** 698–707 (1988).

18. B. M. Fenton, S. F. Paoni, J. Lee, C. J. Koch, and E. M. Lord, "Quantification of tumor vasculature and hypoxia by immuno-histochemical staining and HbO_2 saturation measurements," Br. J. Cancer **79,** 464–471 (1999).

19. H. D. Sostman, S. Rockwell, A. L. Sylva, D. Madwed, G. Cofer, H. C. Charles, R. Negro-Villar, and D. Moore, "Evaluation of BA 1112 rhabdomyosarcoma oxygenation with microelectrodes, optical spectrometry, radiosensitivity, and MRS," Magn. Reson. Med. **20,** 253–267 (1991).

20. F. Steinberg, H. J. Röhrborn, T. Otto, K. M. Scheufler, and C. Streffer, "NIR reflection measurements of hemoglobin and cytochrome aa_3 in healthy tissue and tumors," Adv. Exp. Med. Biol. **428,** 69–77 (1997).

21. R. G. Steen, K. Kitagishi, and K. Morgan. "*In vivo* measurement of tumor blood oxygenation by near-infrared spectroscopy: immediate effects of pentobarbital overdose or carmustine treatment," J. Neuro-Oncol. **22,** 209–220 (1994).

22. E. L. Hull, D. L. Conover, and T. H. Foster, "Carbogen-induced changes in rat mammary tumor oxygenation reported by near-infrared spectroscopy," Br. J. Cancer **79,** 1709–1716 (1999).

23. M. S. Patterson, B. Chance, and B. C. Wilson, "Time-resolved reflectance and transmittance for the noninvasive measurement of tissue optical properties," Appl. Opt. **28,** 2331–2336 (1989).

24. E. M. Sevick, B. Chance, J. Leigh, S. Nioka, and M. Maris, "Quantitation of time- and frequency-resolved optical spectra for the determination of tissue oxygenation," Anal. Biochem. **195,** 330–351 (1991).

25. H. Liu, A. H. Hielscher, F. K. Tittel, S. L. Jacques, and B. Chance, "Influence of blood vessels on the measurement of hemoglobin oxygenation as determined by time-resolved reflectance spectroscopy," Med. Phys. **22,** 1209–1217 (1995).

26. S. J. Matcher, M. Cope, and D. T. Delpy. "*In vivo* measurements of the wavelength dependence of tissue-scattering coefficients between 760 and 900 nm measured with time-resolved spectroscopy," Appl. Opt. **36,** 386–396 (1997).

27. E. W. Hahn, P. Peschke, R. P. Mason, E. E. Babcock, and P. P. Antich, "Isolated tumor growth in a surgically formed skin pedicle in the rat: a new tumor model for NMR studies," Magn. Reson. Imaging. **11,** 1007–1017 (1993).

28. Y. Yang, H. Liu, X. Li, and B. Chance, "Low-cost frequency-domain photon migration instrument for tissue spectroscopy, oximetry, and imaging," Opt. Eng. **36,** 1562–1569 (1997).

29. H. Y. Ma, Q. Xu, J. R. Ballesteros, V. Ntziachristors, Q. Zhang, and B. Chance, "Quantitative study of hypoxia stress in piglet brain by IQ phase modulation oximetry," in *Optical Tomography and Spectroscopy of Tissue III*, B. Chance, R. R. Alfano, and B. J. Tromberg, eds., Proc. SPIE **3597,** 642–649 (1999).

30. P. R. Bevington, *Data Reduction and Error Analysis for the Physical Sciences* (McGraw-Hill, New York, 1969).

31. W. H. Press, B. P. Flannery, S. A. Teukolsky, and W. T. Vetterling, *Numerical Recipes* (Cambridge U. Press, Cambridge, 1988).

32. KaleidaGraph, Version 3.08 (Synergy Software, 2457 Perkiomen Avenue, Reading, Pa. 19606, 1996).

33. J. L. Hintze, *NCSS, Version 6.0, User's Guide II: Statistical System for Windows* (Number Cruncher Statistical Systems, Kaysville, Utah, 1996).

34. J. B. Fishkin and E. Gratton, "Propagation of photon-density waves in strongly scattering media containing an absorbing semi-infinite plane bounded by a straight edge," J. Opt. Soc. Am. A **10,** 127–140 (1993).

35. W. G. Zijlstra, A. Buursma, and W. P. Meeuwsen-van der Roest, "Absorption spectra of human fetal and adult oxyhemoglobin, deoxyhemoglobin, carboxyhemoglobin, and methemoglobin," Clin. Chem. **37,** 1633–1638 (1991).

36. H. Liu, C. L. Matson, K. Lau, and R. R. Mapakshi, "Experimental validation of a backpropagation algorithm for three-dimensional breast tumor localization," IEEE J. Select. Top. Quantum Electron. **5,** 1049–1057 (1999).

37. S. S. Kety, "The theory and applications of the exchange of inert gas at the lungs and tissue," Pharmacol. Rev. **3,** 1–41 (1951).

38. H. Watabe, M. Itoh, V. Cunningham, A. A. Lammertsma, P. Bloomfield, M. Mejia, T. Fujiwara, A. K. P. Johes, T. Johes, and T. Nakamura, "Noninvasive quantification of rCBF using positron emission tomography," J. Cerebr. Blood Flow Metab. **16,** 311–319 (1996).

39. S. S. Kety, "Cerebral circulation and its measurement by inert diffusible racers," Israel J. Med. Sci. **23,** 3–7 (1987).

40. A. D. Edwards, C. Richardson, P. Van Der Zee, C. Elwell, J. S. Wyatt, M. Cope, D. T. Delpy, and E. O. R. Reynolds, "Measurement of hemoglobin flow and blood flow by near-infrared spectroscopy," J. Appl. Physiol. **75,** 1884–1889 (1993).

41. H. J. J. A. Bernsen, P. F. J. W. Rijken, T. Oostendorp, and A. J. van der Kogel, "Vascularity and perfusion of human gliomas xenografted in the athymic nude mouse," Br. J. Cancer **71,** 721–726 (1995).

42. R. P. Mason, P. P. Antich, E. E. Babcock, A. Constantinescu, P. Peschke, and E. W. Hahn, "Noninvasive determination of tumor oxygen tension and local variation with growth," Int. J. Radiat. Oncol. Biol. Phys. **29,** 95–103 (1994).

43. B. P. J. van der Sanden, A. Heerschap, A. W. Simonetti, P. J. F. W. Rijken, H. P. W. Peters, G. Stuben, and A. J. van der Kogel, "Characterization and validation on noninvasive oxygen tension measurements in human glioma xenografts by 19F-MR relaxometry," Int. J. Radiat. Oncol. Biol. Phys. **44,** 649–658 (1999).

44. S. Hunjan, R. P. Mason, A. Constantinescu, P. Pescheke, E. W. Hahn, and P. P. Antich, "Regional tumor oximetry: ^{19}F NMR spectroscopy of hexafluorobenzene," Int. J. Radiat. Oncol. Biol. Phys. **41,** 161–171 (1998).

45. S. Hunjan, D. Zhao, A. Constantinescu, E. W. Hahn, P. P. Antich, and R. P. Mason, "Tumor oximetry: an enhanced dynamic mapping procedure using fluorine-19 echo planar magnetic resonance imaging," Int. J. Radiat. Oncol. Biol. Phys. (to be published).

46. S. P. Robinson, F. A. Howe, L. M. Rodrigues, M. Stubbs, and J. R. Griffiths, "Magnetic resonance imaging techniques for monitoring changes in tumor oxygenation and blood flow," Semin. Radiat. Oncol. **8,** 198–207 (1998).

47. B. M. Fenton, "Effects of carbogen plus fractionated irradiation on KHT tumor oxygenation," Radiother. Oncol. **44,** 183–190 (1997).

Tumor Oxygen Dynamics: Comparison of 19F MR EPI and Frequency Domain NIR Spectroscopy

Yulin Song[1,2]; Kate L. Worden[1]; Xin Jiang[1]; Dawen Zhao[2]; Anca Constantinescu[2]; Hanli Liu[1]; and Ralph P. Mason[2]

[1]*Joint Graduate Program in Biomedical Engineering,*
[2]*Department of Radiology, UT Southwestern Medical Center, Dallas, TX 75235, USA*

ABSTRCT

Oxygen plays a key role in tumor therapy and may be related to tumor development: e.g., angiogenesis and metastasis. Using noninvasive techniques to accurately measure tumor oxygenation could assist in developing novel therapies. Here, we have used the FREDOM (Fluorocarbon Relaxometry using Echo planar imaging for Dynamic Oxygen Mapping) approach based on hexafluorobenzene (HFB) to monitor tissue oxygen tension (pO_2) of rat breast and prostate tumors and compared the results with changes in tumor vascular hemoglobin saturation (sO_2) and concentration observed using a new dual wavelength homodyne near-infrared (NIR) system. The dynamic changes in pO_2 and sO_2 were assessed while rats were breathing various gases. NIR showed significant changes in vascular oxygenation accompanying respiratory interventions. 19F MR-EPI also showed significant changes in tissue pO_2 and revealed considerable regional heterogeneity in both absolute values and rate of change accompanying interventions. Generally, changes in vascular sO_2 preceded tissue pO_2, particularly for smaller tumors.

Keywords: Oxygen tension, Echo planar imaging, MRI, Tumor, NIR spectroscopy

INTRODUCTION

The growth and development of tumors are greatly influenced by oxygen tension (pO_2), e.g., tumor hypoxia leads to increased expression of vascular endothelial growth factor (VEGF), and thus, angiogenesis [1]. Hypoxia reduces radiosensitivity [2], but chemotherapeutic approaches have been proposed to exploit the tumor hypoxia based on selective cytotoxicity of bioreductive drugs [3, 4]. In addition, increasing evidence from clinical trials has revealed that poorly oxygenated tumors have poor prognosis for patients [5, 6]. Therefore, accurate measurements of oxygenation could enhance cancer treatment planning. Here, we present two methods of measuring tumor oxygenation: the FREDOM approach to measure tumor tissue oxygen tension (pO_2) and NIR spectroscopy to measure changes in tumor vascular hemoglobin saturation (sO_2) and concentration [Hb]. By comparing these two techniques, we can examine the relationship between tumor tissue pO_2 and vascular sO_2.

The FREDOM approach is based on 19F PBSR-EPI of hexafluorobenzene (HFB). It has been shown that the spin-lattice relaxation rate, $R1$ (1/T1), is linearly proportional to dissolved oxygen concentration [7]. HFB offers exceptional sensitivity to changes in pO_2 while having little response to temperature [8]. Because of structural symmetry, HFB has a single resonance and thus, is free from chemical shift artifact, providing an optimal signal-to-noise ratio (SNR). Maps of the tumor tissue pO_2 were obtained in 8 minutes with millimeter resolution, allowing the fate of individual voxels to be traced. NIR spectroscopy can be used to measure tumor vascular sO_2 because the absorption coefficients of deoxy-hemoglobin differ from those of oxy-hemoglobin at the wavelengths selected (758 nm and 782 nm) [9]. The system has many attractive features: completely non-invasive, inexpensive, portable, and real-time.

METHODS

Tumor Model

NF 13762 breast and Dunning prostate R3327-AT1 adenocarcinomas were implanted in skin pedicles on the forebacks of adult female Fischer and male Copenhagen rats (~250 g), respectively, as described

previously [10]. Once the tumors reached ~1 cm diameter, the rats were anesthetized with 200 µl ketamine hydrochloride (100 mg/ml) and maintained under general gaseous anesthesia (33% O_2, 66% N_2O and 0.5%) through a mask placed over the mouth and nose. Body temperature was maintained at 37°C by a thermal blanket. A fiber optic pulse oximeter was placed on the hind foot to monitor arterial hemoglobin saturation and heart rate, and a fiber optic probe was inserted rectally to monitor core temperature. NIR spectroscopy and ^{19}F PBSR-EPI measurements were then performed sequentially, while inhaled gas was alternated between 33% O_2, carbogen (95% O_2 + 5% CO_2), and 100% O_2.

NIR Spectroscopy

The tumor vascular sO_2 was assessed by NIR spectroscopy using a new dual wavelength, homodyne system (wavelengths 758 nm and 782 nm). These wavelengths were selected because they not only allow the calculation of sO_2, but also fall into the range of wavelengths compatible with the low cost photo multiplier tube (PMT). The system uses only one RF source to determine amplitude and phase changes of light. Figure 1 shows a schematic diagram of the system. An RF source modulates the light from two laser diodes at 140 MHz. The light passes through fiber optic cables, is transmitted through the tumor tissue, and is collected by a second fiber bundle. The light is then detected, amplified, filtered, and demodulated into I and Q components. Amplitude and phase changes caused by the tumor are related to changes in hemoglobin concentration [Hb] and hemoglobin saturation [HbO_2], i.e., sO_2.
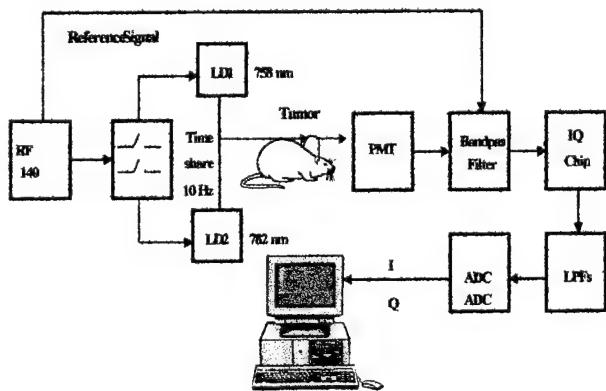
Figure 1. A schematic diagram of the NIR IQ system

To obtain the absorption coefficients of deoxy-hemoglobin and oxy-hemoglobin, we have assumed background absorbance to be negligible and estimated

the absorption coefficients by multiplying the extinction coefficients for deoxy-hemoglobin and oxy-hemoglobin with their respective concentrations.

$$\mu_a^{758} = \varepsilon_{Hb}^{758}[Hb] + \varepsilon_{HbO2}^{758}[HbO_2] \qquad (1)$$
$$\mu_a^{782} = \varepsilon_{Hb}^{782}[Hb] + \varepsilon_{HbO2}^{782}[HbO_2] \qquad (2)$$

where μ_a^{758} and μ_a^{782} are the absorption coefficients, ε_{Hb}^{758} and ε_{Hb}^{782} the extinction coefficients for deoxy-hemoglobin, ε_{HbO2}^{758} and ε_{HbO2}^{782} the extinction coefficients for oxy-hemoglobin at the wavelengths 758 nm and 782 nm, respectively, and [Hb] and [HbO_2] are the deoxy-hemoglobin and oxy-hemoglobin concentrations, respectively.

Although the IQ system does give both phase and amplitude values, given the tumors' small sizes and our fiber configuration, conventional diffusion theory doesn't hold. To overcome this difficulty, we modified Beer-Lambert's law and used the amplitude values to find trends in the changing absorption coefficients.

$$\mu_{aC} - \mu_{aI} = (1/L)*\log (A_I/A_C) \qquad (3)$$

where A_I is the initial amplitude (amplitude of baseline), A_C the current amplitude, and L the optical pathlength between source and detector.

By manipulating equations 1-3, we can compute changes in blood volume and saturation between the initial state and the intervention state from the transmitted amplitude of the light through the tumor.

$$\Delta[Hb]_{total} = -(3.63/L)* \log (A_I/A_C)^{758} + (8.68/L)* \log (A_I/A_C)^{782} \qquad (4)$$

$$\Delta[HbO_2] - \Delta[Hb] = -(18.49/L)* \log (A_I/A_C)^{758} + (21.20/L)* \log (A_I/A_C)^{782} \qquad (5)$$

where $\Delta[\,]$ represents change in concentration. The constants were computed with extinction coefficients for oxy- and deoxy-hemoglobin at the two wavelengths used.

Once stable baseline measurements were achieved, the inhaled gas was altered to pure oxygen or carbogen and dynamic changes were observed over a period of two hours. Both the magnitude and rate of change of sO_2 were examined. Following the NIR experiments, the MRI experiments were performed.

[19]F MR-EPI

All MRI experiments were performed on an Omega CSI 4.7 T 40 cm system with actively shielded

gradients. A tunable 2 cm $^1H/^{19}F$ single turn solenoid coil was placed around the tumor and 40 µl HFB were injected directly into both central and peripheral regions of the tumor using a 32 G needle. Shimming was performed on the ^1H signal of the tissue water to a typical linewidth of 50 Hz. 3D spin-echo (SE) ^1H images were acquired for anatomical reference and corresponding ^{19}F images were then obtained to show the distribution of HFB in the tumor. Regional tumor pO_2 maps were generated using ^{19}F PBSR-EPI based on the relationship: $pO_2 (torr) = [R1 - 0.074]/0.0016$, where $R1$ is the spin lattice relaxation rate of HFB, as described in detail previously [11]. Twenty-three pO_2 maps were produced in 3 hours with respect to respiratory challenge.

Figure 2. Hemoglobin saturation and concentration change in a 4.0 cm³ breast tumor.

RESULTS

NIR Results

Figure 2 shows the time course of changes in tumor vascular hemoglobin saturation and concentration accompanying alterations in inhaled gases for a breast tumor and Figure 3 shows the result for a prostate tumor. Hemoglobin saturation and concentration are presented as relative millimolar changes. Both tumors show significant changes in vascular oxygenation accompanying respiratory interventions. Hemoglobin saturation increased almost immediately after a gas switch from baseline (33% O_2) to either carbogen or 100% O_2 and increased steadily for several minutes, and then gradually returned to baseline after the gas was switched back to baseline. In contrast, total hemoglobin change is insignificant, indicating relatively constant blood volume in the tumor.

Figure 3. Hemoglobin saturation and concentration change in a 4.0 cm³ prostate tumor.
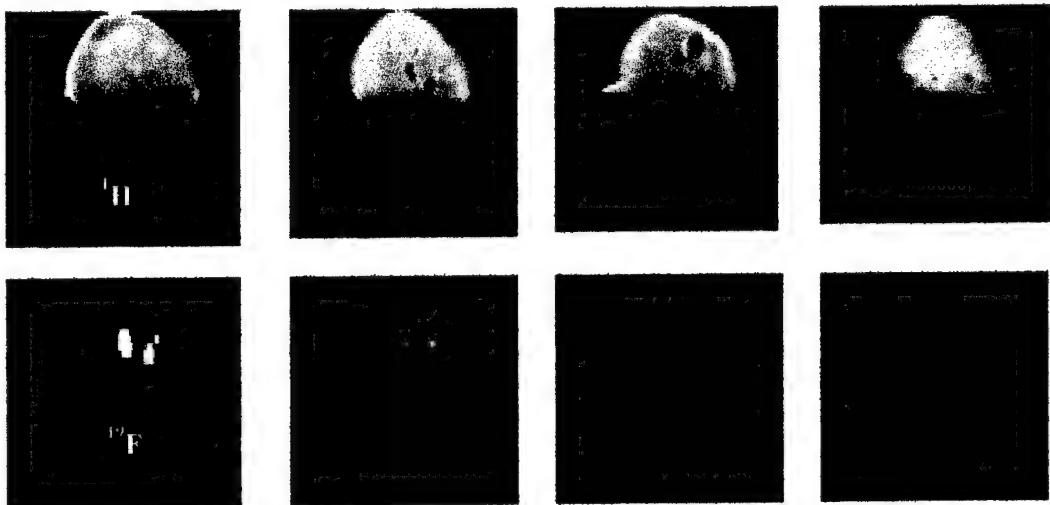
Figure 4. ^1H and ^{19}F coronal images of a breast tumor. FOV = 48 x 48 mm, matrix size = 128 x 64, and slice thickness = 4 mm.

3

MRI Results

Figure 4 shows conventional spin echo (SE) ^1H images (upper) and corresponding ^{19}F images of a representative breast tumor. Figure 5a shows a ^{19}F PBSR-EPI projection image obtained from the tumor shown in Figure 4 in a single acquisition ($\tau = 90$ s) and Figure 5b shows corresponding pO_2 map (expanded).

a)

b)

100
80
60
40
20
0
torr
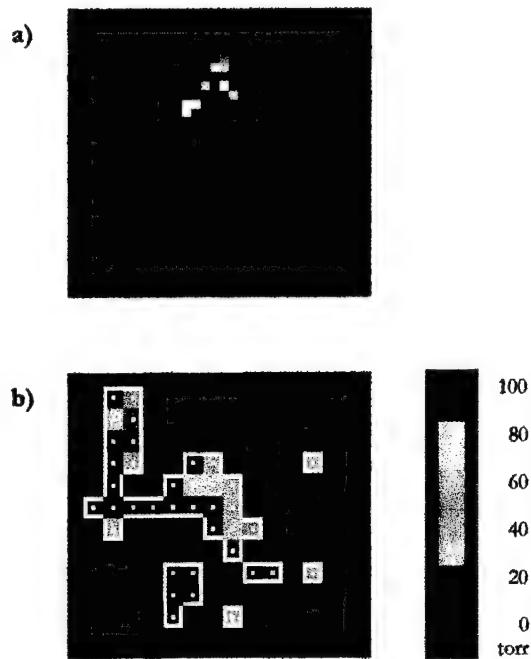
Figure 5. (a) A ^{19}F PBSR-EPI projection image obtained from the tumor shown in Figure 4 in a single acquisition = 90 s). Fourteen images were acquired with variable relaxation delays (τ) ranging from 200 ms to 90 sec and 1.5 mm in plane resolution. (b) Corresponding pO_2 map (expanded).

The ^{19}F MR-EPI oximetry of tumor has the distinct advantage over other techniques that subsequent measurements are completely non-invasive. The greatest strength of this method is the ability to trace the fate of individual voxels (regions) with respect to therapeutic interventions. Figure 6 shows dynamic changes in pO_2 of six specific voxels of a breast tumor with respect to different inhaled gases. It is noteworthy that voxels with high baseline pO_2 had significantly different response characteristics from those with initially low pO_2, which showed small changes. Figure 7 shows pO_2 histograms obtained by FREDOM of HFB for a representative breast tumor. The histograms show the heterogeneity of pO_2 values within the tumor as well as the mean pO_2 values.
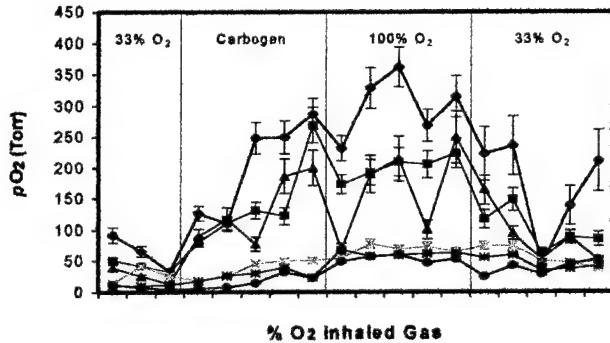
Figure 6. Dynamic changes in pO_2 of six specific voxels of a breast tumor.
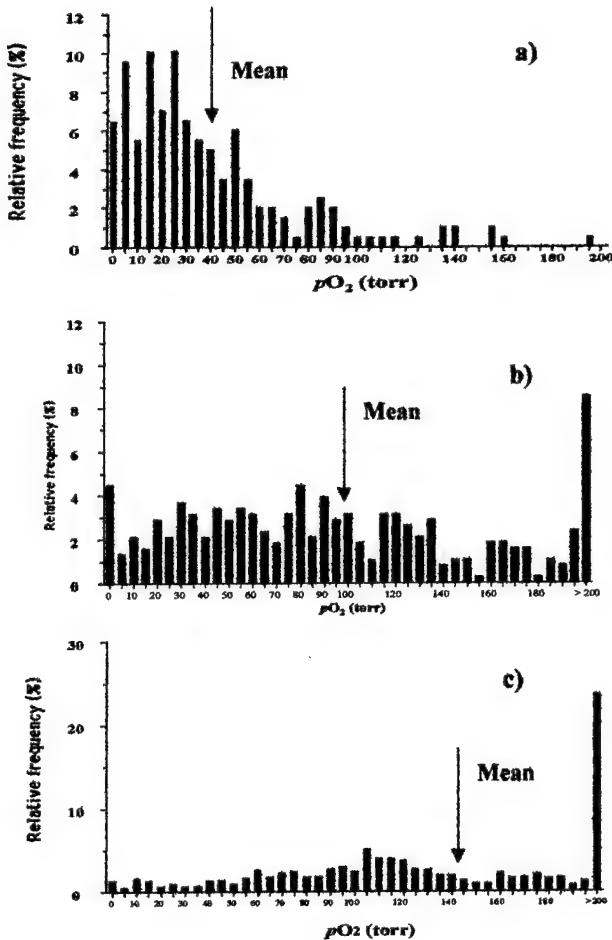
Figure 7. Histograms of oxygen tension for an NF13762 breast tumor determined by FREDOM of HFB. (a) pO_2 distribution while the rat breathed 33% O_2. Mean pO_2 = 44 ± 3 torr. (b) pO_2 distribution while the rat breathed carbogen (95% O_2 + 5% CO_2). Mean pO_2 = 99 ± 4 torr. (p<0.0001). (c) pO_2 distribution while the rat breathed 100% O_2. Mean pO_2 = 145 ± 4 torr.

4

Comparison

While absolute pO_2 values are important for investigating tumor hypoxia, dynamic changes may be more valuable for investigating tumor response to therapeutic interventions. Figure 8 shows comparisons between the dynamic changes in pO_2 and sO_2. Since the IQ system provides a global sO_2 value, each pO_2 data point is represented as an average over all voxels of each pO_2 map.
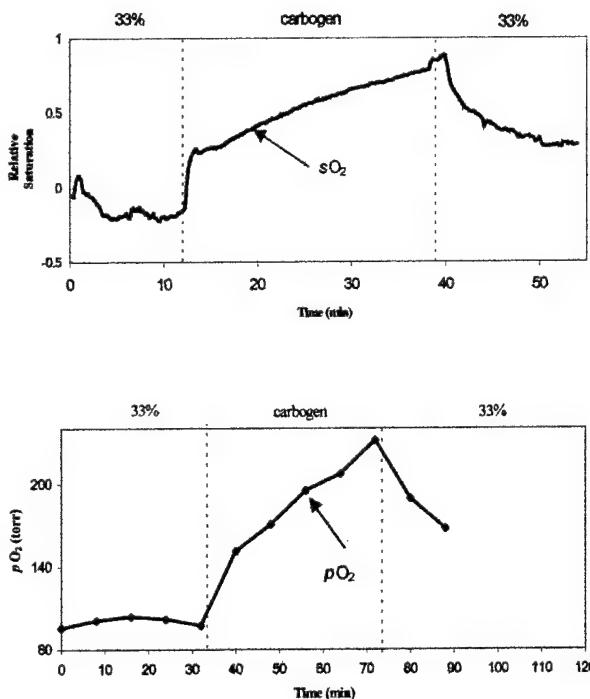

Figure 8. Comparison of pO_2 and hemoglobin saturation (sO_2) of a breast tumor. (a) sO_2 determined by NIR spectroscopy.(b) pO_2 determined by FREDOM. Both pO_2 and sO_2 increase with a transition from 33% to carbogen and begin to decrease when switched back to 33% O_2. Changes in vascular sO_2 precede tissue pO_2. The tumor size $= 1.9 \times 2.2 \times 2.0$ cm.

To further investigate the response, we modeled the temporal response in pO_2 and sO_2 using exponential equations:

$$y = a + b \cdot (1 - e^{-t/\tau}), \quad \text{for increasing trend} \quad (6)$$

$$y = a + b \cdot e^{-t/\tau} \qquad , \text{ for decreasing trend} \quad (7)$$

where y is pO_2 or sO_2, a and b are two constants, t is time, and τ is the time constant.

Changes in sO_2 were faster than pO_2 (Figure 9), especially in the case of larger tumor, which was found

to be less well oxygenated and presumably less well perfused.
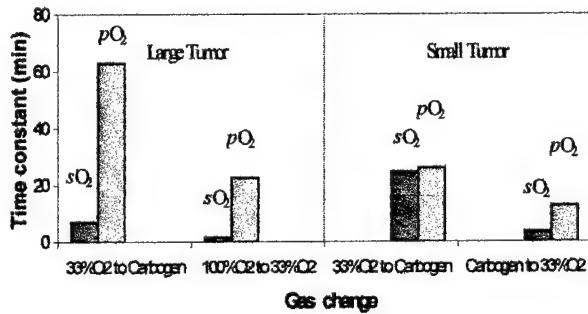
Figure 9. Comparison of pO_2 and sO_2 time constants of two breast tumors (small tumor $= 1.9 \times 2.2 \times 2.0$ cm, large tumor $= 2.4 \times 2.2 \times 2.1$ cm). The temporal responses in pO_2 and sO_2 were modeled using exponential equations.

DISCUSSION

Since poorly oxygenated tumors tend to resist conventional therapy, there have been many efforts to re-oxygenate tumors prior to therapy. A simple intervention is respiratory challenge, i.e., attempting the elevated oxygen concentration of the inhaled gas. Past clinical trials were often disappointing, but it is now thought that results were significantly influenced by the inability to identify hypoxic tumors (i.e., those which would benefit from manipulation), a priori. As techniques become available to measure tumor oxygenation, it is appropriate to reevaluate approaches to manipulating tumor oxygenation. By increasing the oxygen tension of the inspired gas, the arterial sO_2 should increase, leading to increased hemoglobin saturation of the tumor vasculature, and hence, increased tumor tissue pO_2. Our data indicate that breathing elevated O_2 did indeed have a significant effect on both tumor vascular sO_2 and tissue pO_2. For a typical large breast tumor, significant changes were found in vascular sO_2 ($p<0.05$) and in tissue pO_2 ($p<0.0001$) by ANOVA in the case of carbogen inhalation, and ($p<0.01$) and ($p<0.0001$) in the case of oxygen inhalation. There has been a debate as to whether carbogen is more effective at modulating tumor oxygenation than 100% oxygen since CO_2 is a vasodilator. Indeed, recent work in a human glioma xenografts suggested that oxygen alone had no influence on tumor vascular oxygenation, whereas carbogen produced a pronounced effect [12]. Our preliminary results indicate that both gases produced changes in sO_2

and pO_2, with vascular sO_2 increasing more with 100% O_2 inhalation than with carbogen.

We recently showed that the FREDOM approach indicates similar pO_2 values in tumors to electrodes [13], especially on interstitial tissue pO_2. By contrast, NIR investigates vascular oxygenation. As expected, changes in vascular oxygenation (sO_2) were found to be more rapid than tumor tissue pO_2, with greater differences in large tumors. This probably reflects the extensive perfusion of the small tumors with lesser perfusion of large tumors as reflected by lower mean pO_2 and larger hypoxic fraction [13].

Regional tumor tissue pO_2 and blood sO_2 are important physiological parameters. The capability to measure them will provide insight into progressive physiological changes in a tumor accompanying interventions. NIR has the advantages of being entirely noninvasive, inexpensive, portable, and real-time. But the MRI approach clearly reveals detailed oxygenation heterogeneity. The correlation of NIR and MR technologies will provide insight into issues of oxygen delivery and consumption. We believe that application of multiple approaches to tumor oxygenation can lead to better understanding of tumor physiology and probably optimized tumor therapy.

ACKNOWLEDGMENTS

REFERENCES

1. Pötgens, A.J.G., Westphal, H.R., de Waal, R.M.W, and Ruiter, D.J., *The Role of Vascular Permeability Factor and Basic Fibroblast Growth Factor in Tumor Angiogenesis*. Biol. Chem. Hopper-Seyler, 1995, 376:57-70.

2. Gray, L.H., Conger, A.D., Ebert, M., Hornsey, S., and Scott, O.C.A., *The Concentration of Oxygen Dissolved in Tissues at the Time of Irradiation as a Factor in Radiotherapy*. Br. J. Radiol. 1953, 26:638-648.

3. Brown, J.M., Giaccia, A.J., *Tumor Hypoxia: the Picture has Changed in the 1990s*. Int. J. Radiat. Biol. 1994, 65:95-102.

4. Stratford, I., Adams, G., Bremmer, J., Cole, S., *et al.*, *Manipulation and Exploitation of the Tumor Environment for Therapeutic Benefit*. Int. J. Radiat. Biol. 1994, 85-94.

5. Höckel, M., Schlenger, K., Aral, B., Mitze, M., Schäffer, U., and Vaupel, P., *Association between Tumor Hypoxia and Malignant Progression in Advanced Cancer of the Uterine Cervix*. Cancer Res. 1996, 56:4509-15.

6. Fyles, A.W., Milosevic, M., Wng, R., Kavanagh, M.C., Pintile, M., Sun, A., Chapman, W., Levin, W., Manchul, L., Keane, T.J., and Hill, R.P., *Oxygenation Predicts Radiation Response and Survival in Patients with Cervix Cancer*. Radiother. Oncol. 1998, 48:149-56.

7. Mason, R.P., *Non-invasive Physiology: ^{19}F NMR of Perfluorocarbons*. Artif. Cells Blood Subs, Immob. Biotechnol. 1994, 22:1141-1153.

8. Mason, R.P., Rodbumrung, W., Antich, P.P., *Hexafluorobenzene: a Sensitive ^{19}F NMR Indicator of Tumor Oxygenation*. NMR in Biomed. 1996, 9:125-134.

9. Yunsong, Y., Liu, H., Li, X., and Chance, B., *Low-Cost Frequency-Domain Photon Migration Instrument for Tissue Spectroscopy, Oximetry, and Imaging*. Opt. Eng. 1997, 36(5):1562-1569.

10. Hahn, E. W., Peschke, P., Mason, R.P., Babcock, E.E., and Antich, P.P., *Isolated Tumor Growth in a Surgically Formed Skin Pedicle in the Rat: A New Tumor Model for NMR Studies*. Magn. Reson. Imaging. 1993, 11:1007-1017.

11. Le, D., Mason, R.P., Hunjan, S., Constantinescu, A., Barker, B.R., and Antich, P.P., *Regional Tumor Oxygen Dynamics: ^{19}F PBSR EPI of Hexafluorobenzene*. Magn. Reson. Imaging. 1997, 15:971-981.

12. van der Sanden, B.P.J., Heerschap, A., Simonetti, A.W., Rijken, P.F.J.W., Peters, H.P.W., Stüben, G., and van der Kogel, A.J., *Characterization and Validation of Noninvasive Oxygen Tension Measurements in Human Glioma Xenografts by ^{19}F-MR Relaxometry*. Int. J. Radiat. Oncol. Biol. Phys. 1999, 44(3):649-658.

13. Mason, R.P., Constantinescu, A., Hunjan, S., Le, D., Hahn, E.W., Blum, C., Antich, P.P., and Peschke, P., *Regional Tumor Oxygenation and Measurement of Dynamic Changes*. Radiat. Res. 1999, 152:239-249.

Tumor Oximetry: A comparison between near-infrared frequency-domain spectroscopy of hemoglobin saturation and ^{19}F MRI of hexafluorobenzene

Katherine L. Worden[*], Yulin Song[*φ], Xin Jiang[*], Ralph P. Mason[φ], Hanli Liu[*]

[*]Joint Biomedical Engineering Program
University of Texas at Arlington/University of Texas Southwestern Medical Center at Dallas
Dallas, TX 75235

[φ]Department of Radiology
University of Texas Southwestern Medical Center at Dallas
Dallas, TX 75235

ABSTRACT

Studies have shown that hypoxic tumor cells are relatively more resistant to radiotherapy, chemotherapy, and photodynamic therapy. Tumor oximetry, e.g., measurement of oxygen tension (pO_2) of tissue and/or blood oxygenation (SO_2) of the vascular bed, could be valuable for optimizing treatment plans.

In this study, we employed a recently developed homodyne system to measure changes in hemoglobin saturation (SO_2) and concentration in the vascular bed of rat prostate and breast tumors. For comparison, tissue pO_2 values were measured using ^{19}F MR EPI of hexafluorobenzene, providing a map of regional tumor oxygenation tension. Both SO_2 and pO_2 measurements were taken while the inhaled gas was alternated between 33% oxygen, 100% oxygen and carbogen (95% oxygen, 5% CO_2).

The results obtained for both techniques showed significant changes in tumor oxygenation accompanying respiratory challenge, with changes in vascular SO_2 preceding tissue pO_2 change. The combined use of these two techniques provides new insight into the dynamics of tumor oxygenation by making available a method of obtaining regional information of the state of the tissue, as well as a non-invasive, real-time method for determining changes in the vascular bed.

Keywords: Frequency-Domain Spectroscopy, NIR spectroscopy, ^{19}F MRI, Hexafluorobenzene, Oximetry

1. INTRODUCTION

Frequently, blood vessel formation is unable to keep up with the rapid growth of a tumor. If this occurs, the cells in the tumor furthest from a fresh blood supply will suffer a lack of oxygen and hypoxic areas will form (chronic hypoxia). These regions can be as much as 3 times more resistant to radiotherapy.[1] In addition to studies in vitro and in animal tumors, there is increasing evidence from clinical trials that poorly oxygenated tumors indicate poor prognosis for patients.[2,3] Methods of determining the oxygen content of a tumor could, therefore, be helpful in the development of an optimal treatment plan. This paper will present the experimental results of two such methods: NIR spectroscopy to determine blood oxygenation (SO_2) of the tumor's vascular bed and ^{19}F MRI of hexafluorobenzene (HFB) to determine tissue pO_2.

NIR spectroscopy, through use of a recently developed frequency-domain system, based on an in-phase and quadrature (IQ) demodulator chip[4], is attractive as a non-invasive, inexpensive, portable, real-time system that can provide global SO_2 values. We show that this IQ system can be used to determine the SO_2 in a tumor's vascular bed and measure the

response of blood volume and oxygen saturation to inhaled gas. The technique of using ^{19}F MRI relaxometry to map tissue pO_2 is also relatively new.[5] The spin-lattice relaxation rate of hexafluorobenzene is particularly sensitive to oxygen while being insensitive to temperature.[6] Following direct injection of HFB into a tumor, ^{19}F MRI maps tissue pO_2 at millimeter resolution. This method facilitates measurements of dynamic changes in pO_2 accompanying therapeutic interventions and allows the fate of individual voxels to be traced.

Through comparison of these two techniques, it is possible to examine the relationship between SO_2 of the vascular bed and pO_2 of the tissue. Blood oxygenation, blood volume, arterial SO_2 and temperature may also be compared.

2. METHODS AND INSTRUMENTATION

2.1 Tumor Model

Dunning prostate adenocarcinoma R3327-AT1 was implanted in adult male Copenhagen rats and NF13762 breast tumor in female Fisher rats. The tumors were grown in pedicles[7] on the forebacks of the rats until they were approximately 2 cm in diameter. Rats were anesthetized with 200 μl ketamine hydrochloride (100 mg/ml) and maintained under general gaseous anesthesia with 33 % inhaled O_2 [0.3 dm^3/min O_2, 0.6 dm^3/min N_2O, and 0.5% methoxyflurane] through a mask placed over the mouth and nose. Body temperature was maintained by a warm water blanket. A fiber optic pulse oximeter was placed on the hind foot to monitor arterial oxygenation (A_{SO2}) and a fiber optic probe was inserted rectally to measure temperature. Inhaled gas was alternated between 33% oxygen, 100% oxygen and carbogen (95% oxygen, 5% carbon dioxide). NIR and EPI measurements were performed sequentially for comparison.

2.2 NIR Spectroscopy

As shown in **figure 1**, we used a new homodyne system able to determine amplitude and phase changes of light.[4] In this setup, an RF source modulates the light from two laser diodes (wavelengths 758 nm and 782 nm) at 140 MHz. The light passes through fiber optic cables, is transmitted through the tissue, and is collected by a second fiber bundle. The light is then detected by a PMT and is demodulated with a commercially available in-phase and quadrature (IQ) demodulator chip into I and Q components. Once these components are put through a low pass filter, they can be used to calculate amplitude and phase. These steps can be seen mathematically in equations 1-4.

(1) $I(t) = 2A \sin(\omega t+\theta) \sin(\omega t) = A \cos(\theta) - A \cos(\omega t+\theta)$ ---> low pass filter ---> $I_{dc} = A \cos(\theta)$

(2) $Q(t) = 2A \sin(\omega t+\theta) \cos(\omega t) = A \sin(\theta) + A \sin(\omega t+\theta)$ ---> low pass filter ---> $Q_{dc} = A \sin(\theta)$

(3) $\theta = \tan^{-1}(Q_{dc} / I_{dc})$

(4) $A = (I_{dc}^2 + Q_{dc}^2)^{1/2}$

A = amplitude of detected light; θ = phase of detected light; ω = modulation frequency (140 MHz)
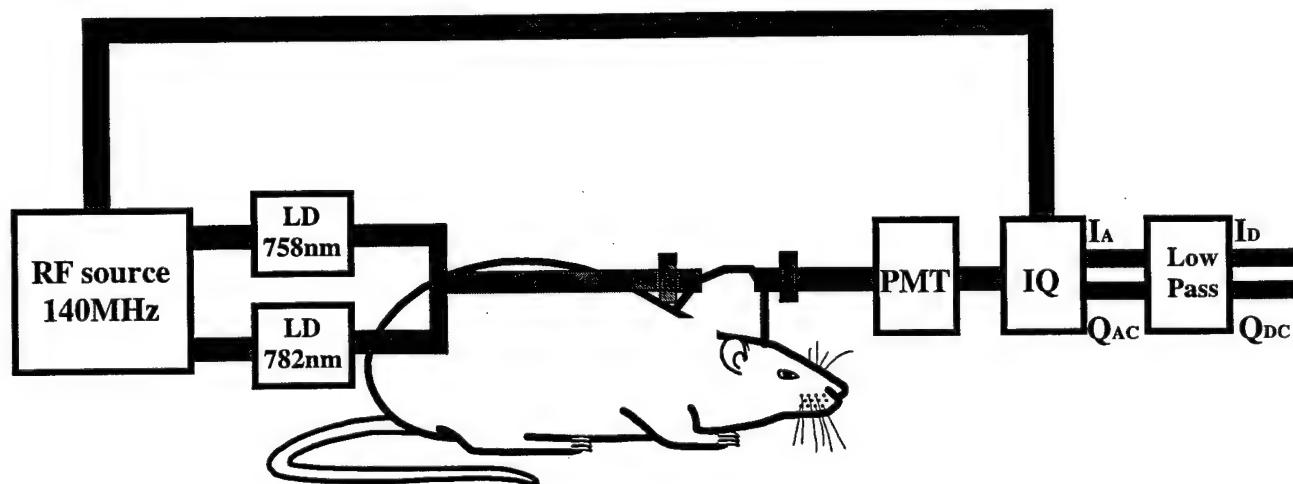

Figure 1: Setup for NIR experiment.

NIR spectroscopy can be used to determine hemoglobin saturation because the extinction coefficient values of deoxygenated hemoglobin differ from those of oxygenated hemoglobin at the wavelengths selected (758 nm and 782 nm). At this point in our algorithm calculations, we have assumed background absorbance to be negligible and estimated that the absorption coefficients were composed of the extinction coefficients for deoxy-hemoglobin and oxy-hemoglobin multiplied by their respective concentrations (equations 5&6).

(5) $\mu_a^{758} = \varepsilon_{Hb}^{758}[Hb] + \varepsilon_{HbO2}^{758}[HbO_2]$
(6) $\mu_a^{782} = \varepsilon_{Hb}^{782}[Hb] + \varepsilon_{HbO2}^{782}[HbO_2]$

The IQ system does give both phase and amplitude values, but given the tumor's small size and our fiber configuration, we haven't yet derived a suitable algorithm to compute μ_a and μ_s. The data presented in this paper was analyzed using Beer-Lambert's law and the amplitude values to find trends in the changing absorption coefficients (equation 7). By manipulating equations 5-7, algorithms were formed which allow the calculation of blood volume and saturation trends from the transmitted amplitude of the light through the tumor (equations 8&9).

(7) $\mu_{aC} - \mu_{aI} = 1/L * \log (A_I/A_C)$
(8) $\Delta[Hb]_{total} = -3.63 * \log (A_I/A_C)^{758} + 8.68 * \log (A_I/A_C)^{782}$
(9) $\Delta[HbO_2] - \Delta[Hb] = -18.49 * \log (A_I/A_C)^{758} + 21.20 * \log (A_I/A_C)^{782}$

A_I = initial amplitude (amplitude of first sample taken); A_C = current amplitude; L = source/detector separation; The constants were computed with extinction coefficients for oxy- and deoxy- hemoglobin at the two wavelengths used.

2.3 MRI Instrumentation and Procedure

MRI experiments were performed on an Omega CSI 4.7 T 40 cm system with actively shielded gradients. A homebuilt tunable 2 cm $^1H/^{19}F$ single turn solenoid coil was placed around the tumor. The first step of the MRI procedure is injection of hexafluorobenzene. HFB (40 µl) was administered directly into the tumor using a fine sharp (32 G) needle with deliberate dispersion along several tracts to interrogate both central and peripheral tumor regions. HFB is ideal for the imaging of pO$_2$ because it has a single resonance and its relaxation rate varies linearly with oxygen concentration. ^1H images were acquired for anatomical reference using a traditional 3D spin-echo pulse sequence as seen in figure 2a. Conventional ^{19}F MR images (**figure 2b**) were then taken to show the 3D distribution of the HFB in the tumor. Figure 2b may be directly overlaid over figure 2a to show the position of the HFB in that slice.
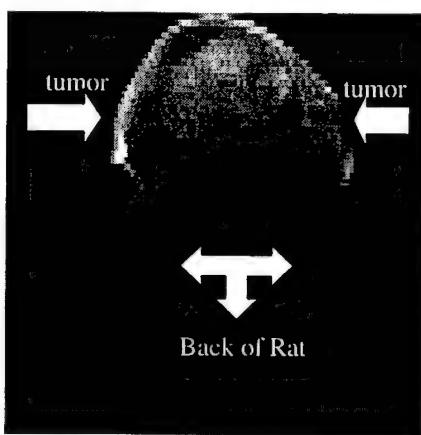

Figure 2a: Proton (^1H) coronal image of a representative slice through a breast tumor (NF13762): TR = 250 ms, TE = 8 ms, NA = 2, FOV = 48 x 48 mm, slice thickness = 4 mm, and matrix size = 128 x 64 x 8.
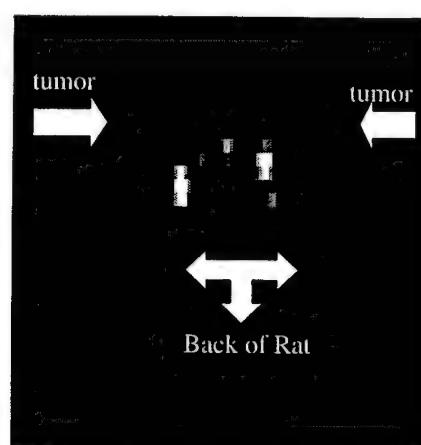
Figure 2b: Corresponding ^{19}F MR Image showing distribution of HFB within the tumor: FOV = 48 x 48 mm, matrix size = 128 x 64

Tumor oxygenation was assessed using ^{19}F PBSR-EPI of HFB.[8] The PBSR preparation pulse sequence consists of a series of 20 non-spatially selective saturating 90° pulses with 20 ms spacing to saturate the ^{19}F nuclei. Following a variable delay time τ, a single spin echo EPI sequence with "blipped" phase encoding was applied.[9] A PBSR-EPI image corresponding to the images shown in **figures 2a and 2b** is shown in **figure 2c**. Fourteen 32×32 PBSR-EPI images, with τ ranging from 200 ms to 90 sec and an FOV of 40×40 mm, were acquired in eight minutes. An $R1$ map was obtained by fitting signal intensity of each voxel of the fourteen images to a three parameter relaxation model by Levenberg-Marquardt least squares algorithm (equation 10):

(10)

$$y_n(i, j) = A(i, j) \cdot [1 - (1 + W) \cdot \exp(-R1(i, j) \cdot \tau_n)]$$

$$(n = 1, 2, \cdots\cdots, 14)$$

$$(i, j = 1, 2, \cdots\cdots, 32)$$

where $y_n(i, j)$ is the measured signal intensity corresponding to delay time τ_n (the nth images) for voxel (i, j), $A(i, j)$ is the fully relaxed signal intensity amplitude of voxel (i, j), W is a dimensionless scaling factor allowing for imperfect signal conversion, and $R1(i, j)$ is the relaxation rate of voxel (i, j) in unit of $\sec^{-1}$
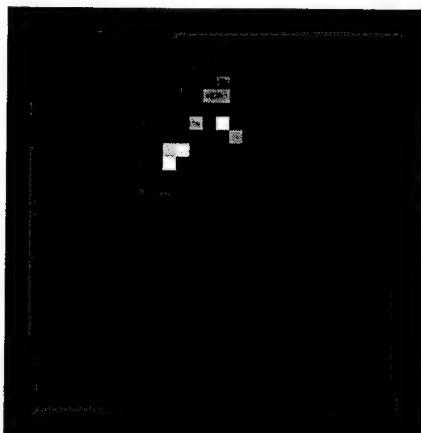
Figure 2c: ^{19}F PBSR-EPI projection image obtained from the tumor in **Figure 1** in a single acquisition ($\tau = 90$ s). Fourteen images, were acquired with variable relaxation delays (τ) ranging from 200 ms to 90 sec. Using a 32 x 32 matrix, FOV of 40 x 40 mm, pO$_2$ maps were generated with 1.25 x 1.25 mm resolution.

pO_2 maps were then generated by applying the calibration curve: $pO_2 \text{(torr)} = [R1(s^{-1}) - 0.074]/0.0016$ to the $R1$ maps.[10] The map shown in figure 2d focuses in on a region of the same slice that was presented in figures 2a-2c.

100

80

60

40

20

0

torr
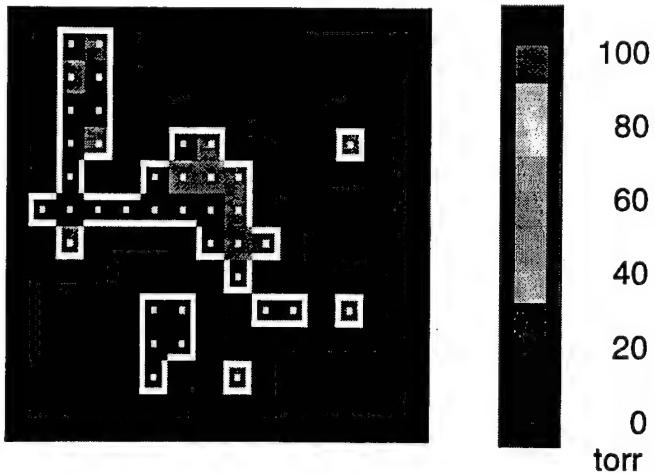
Figure 2d: Typical pO$_2$ map, composed of fourteen PBSR images from the tumor presented in **figure 2a-c**. Using a 32 x 32 matrix, FOV of 40 x 40 mm, pO$_2$ maps were generated with 1.25 x 1.25 mm resolution.

3. RESULTS

3.1 NIR Results

The effects of the inhaled gas on hemoglobin saturation and concentration as recorded by the IQ system are shown below in **figures 3a & 3b**, . The X-axis shows time in minutes from the start of the experiment and the dotted vertical lines mark the point when the gas was changed. Hemoglobin saturation and concentration are presented as unit-less, relative trends. It can easily be seen that hemoglobin saturation begins to increase almost immediately after a gas switch from baseline (33% oxygen) to either carbogen or 100% oxygen and increases steadily for several minutes. Total hemoglobin change is quite small in comparison, indicating relatively constant blood volume in the tumor. These trends seem fairly consistent for both breast and prostate tumors. Typical responses of a breast tumor and prostate tumor are presented below.
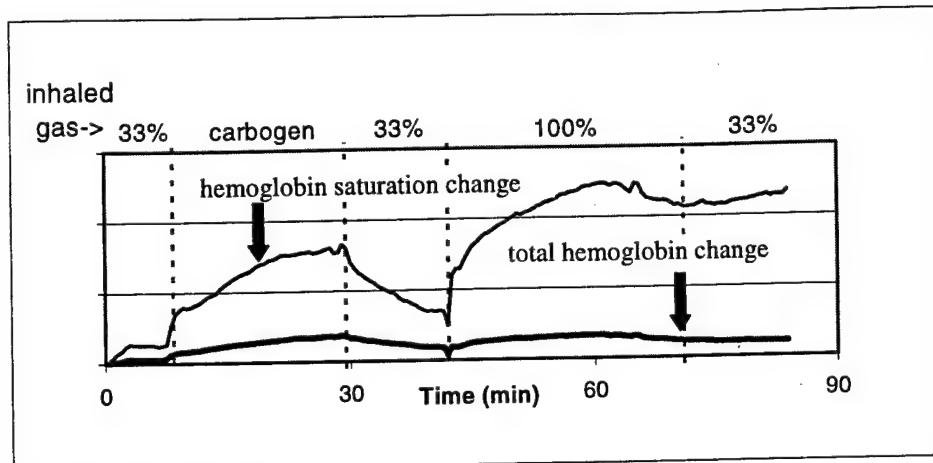
Figure 3a: Hemoglobin saturation and concentration change in a breast tumor.
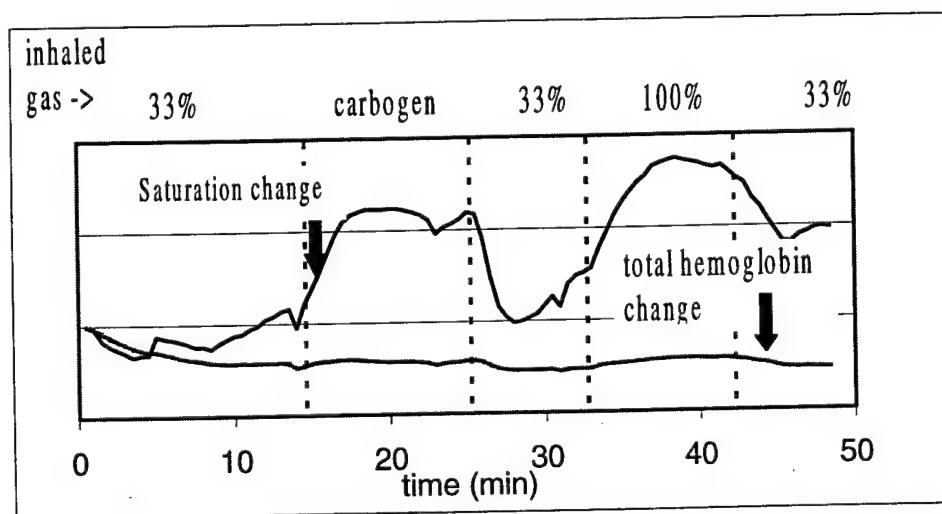
Figure 3b: Hemoglobin saturation and concentration change in a prostate tumor.

It is also worthwhile to compare the saturation changes measured in the tumors vascular bed by the IQ system with the arterial saturation changes measured by a pulse oximeter from the rat's hind foot. One such comparison taken from a prostate tumor is presented below as **figure 4**. Hemoglobin saturation in the vascular bed is again represented as a unit-less trend, arterial saturation values are presented to the right. Again, the X-axis gives the time from the beginning of the experiment in minutes and the dotted lines mark the time of gas change. In the case presented, the arterial saturation follows the same trend as the tumor vascular bed's hemoglobin saturation, but shows a faster change. It should be noted that not all the rats we've studied have behaved this way. We saw a great amount of variability.
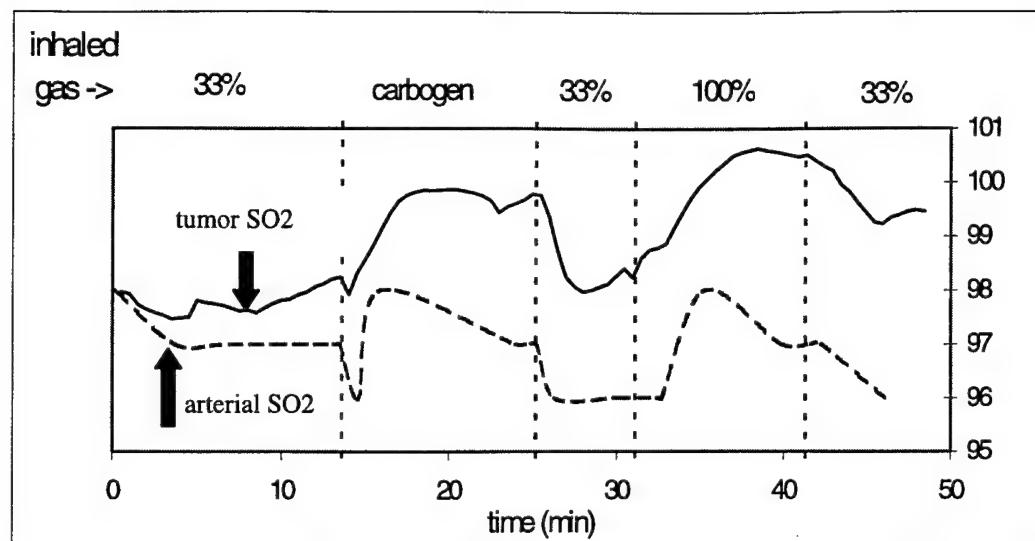
Figure 4: In the prostate tumor presented in Figure 4, both arterial SO_2 and the SO_2 in the tumor increased for inhaled gases carbogen and 100% O_2 and decreased for 33% O_2. Arterial SO_2 in hind foot measured by commercial pulse oximeter and SO_2 in tumor using IQ system.

3.2 MRI Results

MRI provides the advantage of being able to look at regional changes in pO_2 values. Histograms, such as those presented in **figure 5**, are able to show the heterogeneity of pO_2 values within the tumor as well as the average pO_2 values. The data presented here were taken from a breast tumor and show the average values from several pO_2 maps. In **figure 5a**, we see that when the rat was breathing 33% oxygen, the average pO_2 value was about 40 torr. When the rat was breathing carbogen (**figure 5b**), there was a large shift towards higher pO_2 values leading to a mean value of about 99 torr. These values increased further while the rat was breathing 100% oxygen (**figure 5c**) such that the average voxel now had a pO_2 value of about 145 torr. The time course of these changes will be presented later in the paper in **figure 7b**.

Figure 5a: percent voxels in a certain pO_2 range while the rat was breathing 33% oxygen.
Average value = 39.96 ± 3.09 torr
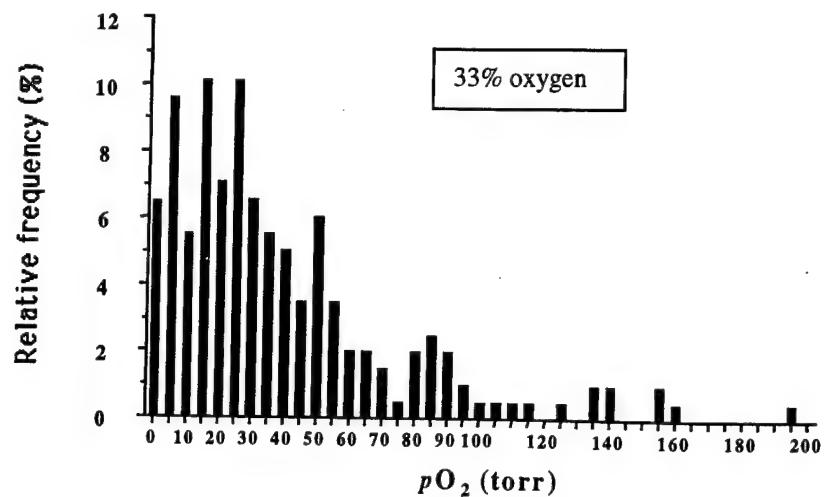
33% oxygen

Figure 5b: percent voxels in a certain pO_2 range while the rat was breathing carbogen.
Average value = 99.30 ± 3.70 torr

carbogen
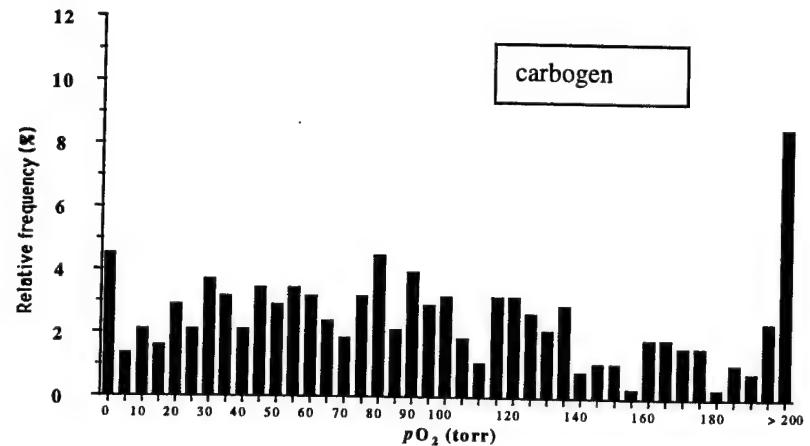
Figure 5c: percent voxels in a certain pO_2 range while the rat was breathing 100% oxygen.
Average value = 145.17 ± 3.52 torr

100% Oxygen
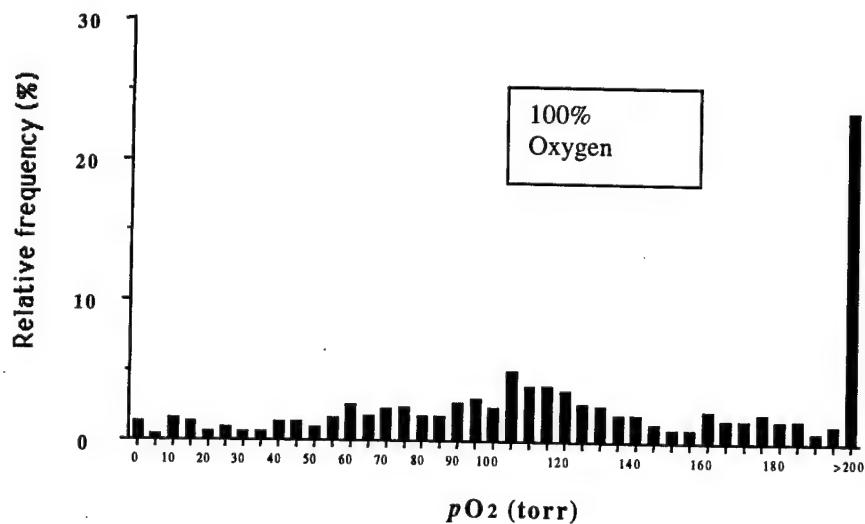
3.3 Comparison

While absolute pO$_2$ values are important for investigating hypoxia, dynamic changes may be more interesting for investigation of response to intervention. In **Figure 6 & 7,** the dynamic changes in pO$_2$ and SO$_2$ are compared. These plots show that pO$_2$ reacts in a very similar fashion to blood saturation, but that the effect is slower. Since the IQ system provies a global measure across the whole tumor, pO$_2$ measurements are presented as mean values attained from the pixels of each pO$_2$ map. The NIR and MRI data shown are for the same rat undergoing the same procedure, but on consecutive days. Data from two breast tumors of various size are presented. The larger tumor was about 2.1 x 2.4 x 2.2 cm, the smaller tumor was 1.9 x 2.2 x 2 cm. Carbogen and 100% oxygen each consistently showed increased SO$_2$ and pO$_2$ over 33% oxygen. The pO$_2$ and SO$_2$ measurements were plotted against the same X-axis to allow for rate of change comparisons.

Figure 6a: Saturation from IQ
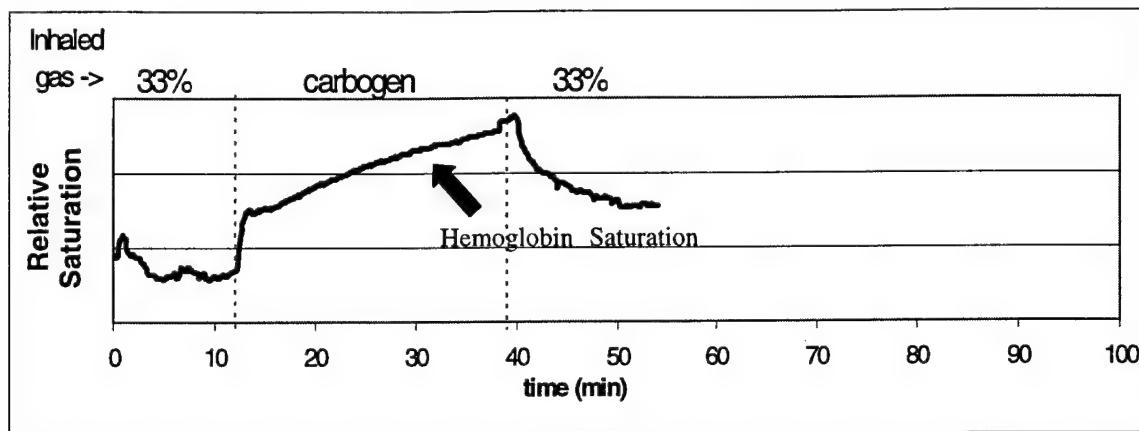
Figure 6b: pO$_2$ from MRI
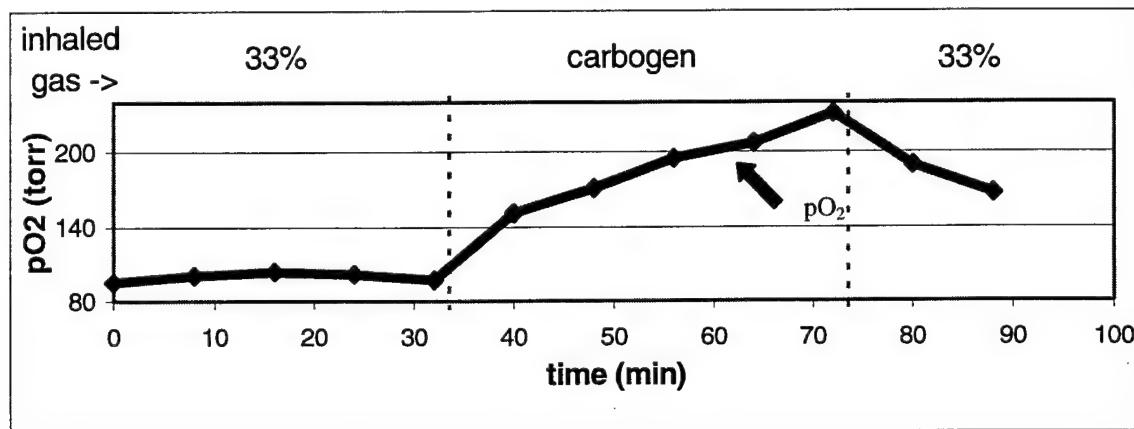
Figure 10: These two sets of data were taken from the small rat tumor on consecutive days. Both the pO$_2$ and blood saturation increased with a transition from 33% to carbogen, and decreased when switched back to 33%.

Figure 7a: Saturation from IQ
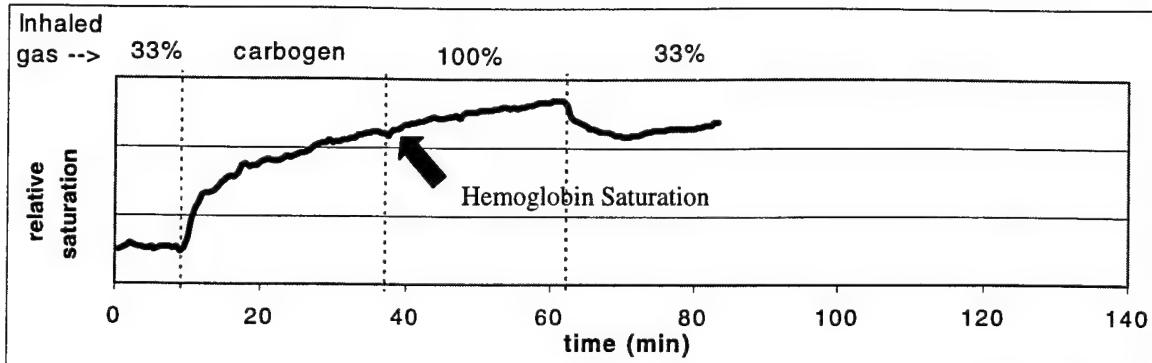

Figure 7b: pO₂ from MRI
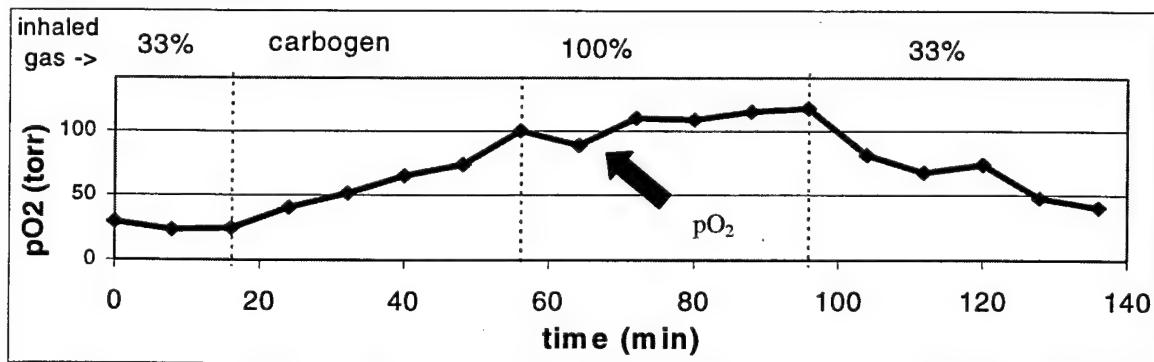
Figure 7: These two sets of data were taken from the large rat tumor on consecutive days. Both the pO_2 and blood saturation increased with a transition from 33% to carbogen, and then further increased slightly when switched from carbogen to 100% oxygen. Values began to decrease when switched back to 33%.

To further study the temporal response, the changes in pO_2 and SO_2 were modeled using the exponential equations 11 and 12 to provide time constant τ.

(11)   For increasing values: $Saturation = a + b*(1-e^{-t/\tau})$

(12)   For decreasing values: $Saturation = a + b*(e^{-t/\tau})$

Generally, blood saturation effects had a much shorter time constant than oxygen tension in the tissue (**Figure 8**). For the smaller tumor, the rate of increase and decrease were much faster for SO_2 than pO_2. Less difference was seen in the larger tumor.
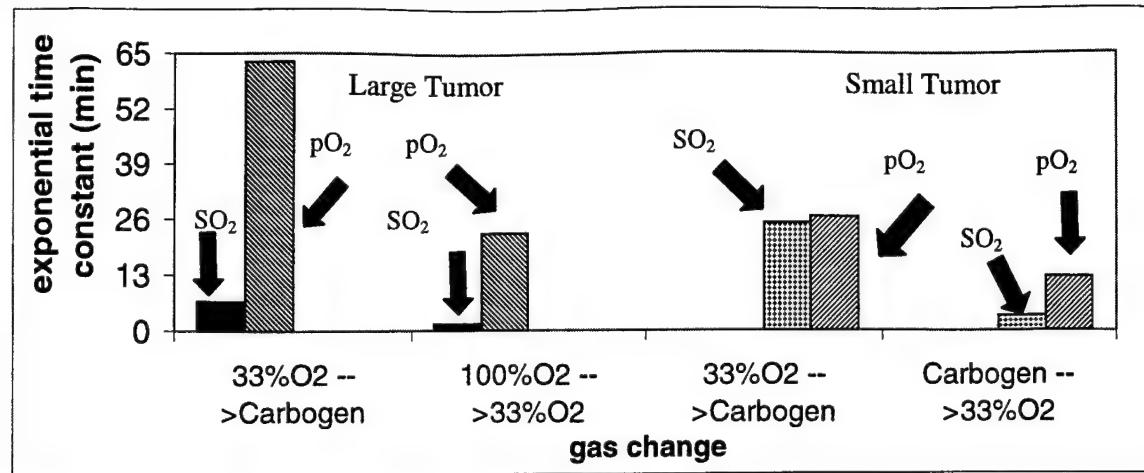
Figure 8: Time constants for the data presented in **Figures 6&7**.

4. CONCLUSION

The data suggest interesting correlations between several vascular parameters. Both tumor vascular Hb saturation and mean pO_2 increased in response to inhaling an elevated percent O_2, either through carbogen or 100% O_2. Arterial SO_2 and tumor SO_2 respond similarly to changes in inhaled gas, with arterial changes preceding changes in the tumor vascular bed. Changes in SO_2 are generally faster than pO_2, though absolute values are highly variable and suggest heterogeneity amongst the tumor population. Given the distinct heterogeneity among tumors even of a given type and size,[11] further investigations are required to form a sound picture of the interplay of multiple vascular parameters.

ACKNOWLEDGEMENTS

REFERENCES

[1] Denekamp, J. Physiological hypoxia and its influence on radiotherapy. *The Biological Basis of Radiotherapy, Second Edition*, Eds. G.G. Steel, G.E. Adams & A. Horwich (Elsevier Science Plblishers B.V., 1989)

[2] M. Hockel, K. Schlenger, B Aral, M. Mitze, U. Schaffer and P. Vaupel, Association between tumor hypoxia and malignant progression in advanced cancer of the uterine cervix. *Cancer Res.* **56**, 4509-15 (1996).

[3] A.W. Fyles, M. Milosevic, R. Wong, M.C. Kavanagh, M. Pintile, A. Sun, W. Chapman, W. Levin, L. Manchul, T.J. Keane and R. P. Hill, Oxygenation predicts radiation response and survival in patients with cervix cancer. *Radiother. Oncol.* **48**, 149-56 (1998).

[4] Yunsong, Y., Liu, H., Li, X., Chance, B. Low-cost frequency-domain photon migration instrument for tissue spectroscopy, oximetry, and imaging. *Opt. Eng.* 36(5) 1562-1569 May 1997

[5] R. P. Mason, Non-invasive physiology: ^{19}F NMR of perfluorocarbon. *Art. Cells, Blood Sub. & Immob. Biotech.* **22**, 4, 1141-1153 (1994).

[6] R.P. Mason, W. Rodbumrung and P.P. Antich, Hexafluorobenzene: a sensitive ^{19}F NMR indicator of tumor oxygenation. *NMR in Biomed.* **9**, 125-134 (1996).

[7] E. W. Hahn, P. Peschke, R. P. Mason, E. E. Babcock and P. P. Antich, Isolated tumor growth in a surgically formed skin pedicle in the rat: a new tumor model for NMR studies. *Magn. Reson. Imaging* **11**, 1007-1017 (1993).

[8] D. Le, R. P. Mason, S. Hunjan, A. Constantinescu, B. R. Barker and P. P. Antich, Regional tumor oxygen dynamics: ^{19}F PBSR EPI of hexafluorobenzene. *Magn. Reson. Imaging* **15**, 8, 971-81 (1997).

[9] B. R. Barker, R. P. Mason, N. Bansal and R. M. Peshock, Oxygen tension mapping by ^{19}F echo planar NMR imaging of sequestered perfluorocarbon. *JMRI* **4**, 595-602 (1994).

[10] D. Le, R. P. Mason, S. Hunjan, A. Constantinescu, B. R. Barker and P. P. Antich, Regional tumor oxygen dynamics: ^{19}F PBSR EPI of hexafluorobenzene. *Magn. Reson. Imaging* **15**, 8, 971-81 (1997).

[11] R. P. Mason, A. Constantinescu, S. Hunjan, D. Le, E. W. Hahn, P. P. Antich, C, Blum and P. Peschke, Regional tumor oxygenation and measurement of dynamic changes. *Radiat. Res.* (submitted 1998).

TUMOR OXIMETRY: COMPARISON OF ^{19}F MR EPI AND ELECTRODES

Ralph P. Mason, Sandeep Hunjan, Anca Constantinescu, Yulin Song, Dawen Zhao,

Eric W. Hahn, Peter P. Antich, and Peter Peschke[+].

U.T. Southwestern Medical Center, Dallas, TX and [+]DKFZ, Heidelberg, Germany

*address correspondence to:

Ralph P. Mason, Ph.D., C. Chem.,

Department of Radiology,

U.T. Southwestern Medical Center,

5323 Harry Hines Blvd.,

Dallas, TX 75235-9058

Tel: (214) 648-8926

Fax (214) 648-2991

E. mail: Ralph.Mason@email.swmed.edu

1

ABSTRACT

We recently described a novel approach to measuring regional tumor oxygen tension using ^{19}F pulse burst saturation recovery NMR echo planar imaging relaxometry of hexafluorobenzene. We have now compared oxygen tension measurements in a group of size matched Dunning prostate rat tumors R3327-AT1 made using this FREDOM (Fluorocarbon Relaxometry using Echo planar imaging for Dynamic Oxygen Mapping). approach with a traditional polarographic method: the Eppendorf Histograph. We also compare MR and electrode approaches to monitoring dynamic changes with respect to interventions and demonstrate extension of the MR technique to rat breast tumors.

Introduction

It is widely appreciated that tumor oxygenation may significantly influence therapeutic success. In particular, the efficacy of radiotherapy [1], photodynamic therapy [2] and hypoxia selective chemotherapeutic agents [3] depend on pO_2. It had been suggested that the ability to measure tumor oxygenation in patients could allow therapy to be individualized and optimized [4], and indeed, several recent studies have found significant prognostic value based on the Eppendorf Histograph in assessing clinical tumors [5-7]. While electrodes may be considered a "gold standard", they have certain shortcomings and there is clearly a need for alternative methods [8]. We have been developing a new approach based on ^{19}F NMR of perfluorocarbons [9-12] and believe the method can now provide useful measurements of tumor oxygen dynamics *in vivo*.

The FREDOM approach exploits the exceptional response of the ^{19}F NMR spin lattice relaxation rate, R1, of fluorocarbons to changes in oxygen tension. Fluorocarbons act as ideal liquids and solvation of gases is directly proportional to the partial pressure of the gas (Henry' law). Since oxygen (O_2) is paramagnetic it induces relaxation in solution directly proportional to the concentration of oxygen, and hence, pO_2 [13]. The highly hydrophobic nature of fluorocarbons ensures both a high solubility of gases, providing molecular amplification, and minimal solvation of other materials (*e.g.*, metal ions) minimizing interference from other environmental factors. We, and others, have explored the use of numerous PFC reporter molecules and various routes of administration [14]. We believe that direct intra tumoral (i.t.) injection of HFB provides an optimal approach to tumor oximetry, and should provide measurements comparable to those obtained using electrodes. In addition, this minimally invasive approach facilitates mapping of dynamic changes in pO_2 with respect to interventions.

Methods

Dunning prostate adenocarcinomas (R3327-AT1) were implanted in male Copenhagen rats (~250 g), as described in detail previously [15]. Tumors were divided

3

into two groups and allowed to grow to about ~2 cm^3 or > 3.5 cm^3 volume. For MR investigations rats were placed under general gaseous anesthesia with 33% inhaled O_2 (0.3 dm^3/min O_2, 0.6 dm^3/min N_2O, and 0.5% methoxyflurane. Hexafluorobenzene (25 - 40 μl) was injected directly into the tumors in both central and peripheral regions using a Hamilton syringe with a custom made fine sharp needle (32 G). A fiber optic probe was placed rectally to monitor core temperature. NMR experiments were performed using an Omega CSI 4.7 Tesla horizontal bore magnet system with actively shielded gradients with a tunable (^{1}H/^{19}F) single turn size-matched solenoid coil placed around the tumor. Following traditional imaging to establish the distribution of HFB, tumor oxygenation was estimated on the basis of ^{19}F PBSR EPI relaxometry of the HFB [10] with a typical 1.25 mm in plane resolution. For initial work three consecutive R1 measurements were made over a period of 1 hour to investigate reproducibility, and stability of the system when the rats breathed 33% O_2 (baseline). Since R1 is a linear function of pO_2 at constant temperature, pO_2 was estimated on a voxel by voxel basis using the relationship pO_2 (torr) = (R1 - 0.074)/0.0016 [10]. The inhaled gas was then altered to 100% oxygen, and relaxation measurements (three) were immediately repeated over a period of 1 hour. Finally, the gas was switched back to the baseline state and three further pO_2 determinations were immediately performed over 1 hour. Our initial studies required 20 mins to produce a pO_2 map, but more recent introduction of the ARDVARC acquisition protocol [12] provides enhanced maps in 8 mins. Breast 13762 NF adenocarcinomas were examined similarly.

Histography was applied to groups of size matched tumors, which did not receive HFB. Halothane was used in place of methoxyflurane. Using the Eppendorf Histograph 100 to 200 individual pO_2 determinations were made in each tumor ,as recommended by the manufacturer. For dynamic measurements a Diamond General micro-electrode (700 μm) was inserted to a specific location. Baseline pO_2 was measured and the inhaled gas altered to 100% O_2 or carbogen (95%O_2/5%CO_2) for 30 mins. At this stage pO_2 was

4

again measured. Following a series of measurements with different gases at one location, the needle was moved and the gases cycled again.

Statistical significance of changes in oxygenation was assessed using analysis of variance (ANOVA) on the basis of Fisher PLSD. Experiments were approved by the Institutional Animal Care and Advisory Committee conducted in accordance with National Laws.

Results

Both FREDOM and electrode methods indicated similar oxygen tension distributions for the AT1 tumors (Fig. 1). Moreover, both techniques showed that tumors with volume > 3.5 cm^3 were significantly ($p < 0.0001$) less well oxygenated than smaller tumors (volume < 2 cm^3). For the large tumors FREDOM indicated median $pO_2 = 2$ torr and fraction < 10 torr (HF$_{10}$) $= 82$ %, while the Eppendorf electrode indicated median $pO_2 = 3$ torr and HF$_{10} = 84\%$. For the small tumors the match was less good with median $= 15$ v 8 torr and HF$_{10} = 44$ versus 66% for FREDOM and electrode, respectively. Examination of the MR images showed that for 1 small tumor most of the HFB resided very close to the tumor edge and may have biased the apparent pO_2. Indeed, if this tumor was excluded there was no significant difference between the respective pO_2 distributions.

Using the FREDOM approach we also examined response to respiratory challenge. Increasing the concentration of inspired oxygen from 33% to 100% O_2 produced a significant increase ($p < 0.0001$) in tumor oxygenation for the group of small tumors. In contrast no change was observed in the mean pO_2 for the group of large tumors. A strength of the FREDOM approach is the ability to follow individual tumor regions, with respect to intervention, in this case respiratory challenge. Six representative regions were selected from a single tumor (Fig. 2a). Three regions, which were initially well oxygenated ($pO_2 > 10$ torr) showed rapid and significant increases within 8 minutes of switching from 33% O_2 to 100% O_2. Changes in relatively poorly oxygenated regions

were much slower, although 2 of 3 regions did show a significant change in pO_2 after 24 mins.

Electrode investigation of dynamic changes in pO_2 also showed 3 of six regions with significant changes in switching from 33% O_2 to 100% O_2, but only 1 region was also significantly different with carbogen (Fig. 2b).

In a representative large breast tumor (~ 4 cm^3) we found significant changes in pO_2 ($p < 0.0001$) with respect to respiratory challenge with baseline mean $pO_2 = 40\pm3$ rising to mean $pO_2 = 99\pm4$, when rat inhaled carbogen and mean $pO_2 = 145 \pm4$ for oxygen inhalation.

Discussion

These results demonstrate the similarly of measurements obtained using traditional electrodes or the new FREDOM approach to tumor oximetry. In each case there was a significant difference in pO_2 observed in small versus large AT1 tumors. For larger tumors the hypoxic fraction, mean and median were very similar, together with the range of typical pO_2 values. In smaller tumors MR suggested a larger range with a number of measurements in excess of 100 torr. This may have arisen from measurements close to the tumor periphery, which are less common using electrodes.

A significant strength of the FREDOM approach is the ability to monitor dynamic changes in regional pO_2 in response to acute interventions. Others have used the Eppendorf system to examine acute chnages [16], but this required reintroduction of the needle electrode and generation of new tracks. Not only was this invasive, but it also led to sampling of parallel tissue regions rather than the fate of specific regions. Given the extensive heterogeneity encountered in tumors and steep local gradients in pO_2 we believe it will be valuable to follow individual tumor regions. Historically, regional response to intervention was assessed by placing an electrode at a specific location and monitoring changes in pO_2 [17]. We have now performed such experiments with a micro

electrode and found a range of baseline pO_2 values and response to respiratory challenge similar to those seen using MRI.

We have now shown both that there is distinct intra tumoral heterogeneity in baseline oxygenation in the Dunning prostate AT1 tumor and also in the response to intervention. In common with our previous observations a three fold change in FO_2 seems to lead to a threefold response in tumor pO_2. However, the rate of change in highly variable. Preliminary data with 8 min time resolution suggest that well oxygenated regions respond rapidly, whereas those poorly oxygenated require much longer. Such observations could have significant implications for patient inhalation times prior to therapy: while previous work had shown that Pre Irradiation Breathing Times (PIBT) could substantially influence the effect of oxygen or carbogen breathing [18], the differential response of individual tumor regions may not have been fully appreciated.

In developing a new technique it is important demonstrate its reliability, robustness and general application. We and several other groups have now applied the FREDOM approach to tumor oximetry. Initially investigators favored intra venous or intra peritoneal administration of emulsions of fluorocarbons. While material became trapped in tumors and could be used to report pO_2 [19-22], it became increasingly apparent that material delivered via the vasculature tended to bias measurements towards well perfused tumor regions [22]. Indeed, recent measurements by Griffiths *et al.* have confirmed such a bias [23]. Furthermore, the use of emulsions to carry the PFCs tend to lead to extensive uptake by the reticuloendothelial system with hepatomegaly. Intra tumoral administration is minimally invasive provided that a fine sharp needle is applied, as we have used here. We have now extended our work from the Dunning prostate R3327-AT1 tumor, which is poorly differentiated, has only microscopic necrotic foci and is firm, to the 13762 breast tumor, which has less structure and considerable cystic fluid. Here, we have simply reported the ability to measure dynamic changes in the breast tumor oxygenation, but in the accompanying work (Song *et al.*, this volume), we show more extensive results.

7

Since the MR and electrode approaches appear to give similar results one may debate the relative their merits. Clearly, MR is very expensive, with a typical imaging system costing upwards of $1 M, compared with $60 000 for the Eppendorf and < $5 000 for a laboratory micro electrode system. However, MR facilitates the simultaneous measurements of dynamic changes in response to intervention at multiple points within a tumor. While we were able to follow changes in pO2 at specific regions using a needle electrode with placement at sequential locations accompanied by cycling of the intervention, such an approach would be less satisfactory for other interventions, and even here, may have led to some conditioning or hysteresis. The FREDOM approach may be readily combined with other measurements such as blood flow/perfusion [24], pH [25] or metal ions by infusion of appropriate reporter molecules [26].

As a reporter molecule HFB has many advantageous properties. It is cheap, readily available, and exhibits minimal acute toxicity ($LD_{50} > 25$ g/kg) [27]. No signs of renal or hepatic toxicity have been found [28] and others have tested doses as high as 50 g/kg (twice weekly) orally in rats over 35 weeks [29]. We typically find substantial clearance from tumors within 24 h, though this does limit our measurements to acute response to interventions [12]. High symmetry within the molecule leads to a single ^{19}F MR resonance providing optimal SNR. The R1 ($=1/T1$) is highly sensitive to pO2 while showing little response to temperature [9]. Long T1s up to 14 s appear to make HFB less efficient for spin lattice relaxometry, but use of the pulse burst saturation recovery approach minimizes the length of th experiment [10] and a large range of T1 values is a requisite for sensitivity to changes in pO2. The long transverse relaxation time (T2) is ideally suited to echo planar imaging.

The ultimate value of a novel technique will depend on its adoption by multiple laboratories, and the significance of the results that can be generated. We believe that the FREDOM approach is versatile and we are demonstrating increasing applications, and thus, we foresee expanded future application of the technique.

Reference:

1. Hall EJ. The oxygen effect and reoxygenation. In: Hall EJ, ed. Radiobiology for the Radiologist. 3 ed. Philadelphia: Lippincott, J. B., 1994: 133-152.

2. Chapman JD, Stobbe CC, Arnfield MR, Santus R, Lee J, McPhee MS. Oxygen Dependency of Tumor Cell Killing *In Vitro* by Light Activated Photofrin II. Radiat. Res. 1991;126:73-79.

3. Brown JM, Giaccia AJ. Tumor hypoxia: the picture has changed in the 1990s. Int. J. Radiat. Biol. 1994;65:95-102.

4. Vaupel PW, Höckel M. Oxygenation status of human tumors: a reappraisal using computerized pO_2 histography. In: Vaupel PW, Kelleher DK, Günderoth M, eds. Tumor Oxygenation. Stuttgart: Gustav Fischer, 1995: 219-232. (Thews G, ed. Funktionsanalyse biologischer Systeme; vol 24).

5. Fyles AW, Milosevic M, Wong R, et al. Oxygenation predicts radiation response and survival in patients with cervix cancer. Radiother. Oncol. 1998;48:149-56.

6. Höckel M, Schlenger K, Aral B, Mitze M, Schäffer U, Vaupel P. Association between tumor hypoxia and malignant progression in advanced cancer of the uterine cervix. Cancer Res. 1996;56:4509-15.

7. Nordsmark M, Overgaard M, Overgaard J. Pretreatment oxygenation predicts radiation response in advanced squamous cell carcinoma of the head and neck. Radiother. Oncol. 1996;41:31-40.

8. Stone HB, Brown JM, Phillips T, Sutherland RM. Oxygen in human tumors: correlations between methods of measurement and response to therapy. Radiat. Res. 1993;136:422-434.

9. Mason RP, Rodbumrung W, Antich PP. Hexafluorobenzene: a sensitive ^{19}F NMR indicator of tumor oxygenation. NMR in Biomed. 1996;9:125-134.

10.   Le D, Mason RP, Hunjan S, Constantinescu A, Barker BR, Antich PP. Regional tumor oxygen dynamics: [19]F PBSR EPI of hexafluorobenzene. Magn. Reson. Imaging, 1997;15(8):971-81.

11.   Mason RP, Constantinescu A, Hunjan S, et al. Regional tumor oxygenation and measurement of dynamic changes. Radiat. Res. 1999;152:239.

12.   Hunjan S, Mason RP, Constantinescu A, Peschke P, Hahn EW, Antich PP. Regional tumor oximetry: ^{19}F NMR spectroscopy of hexafluorobenzene. Int. J. Radiat. Oncol. Biol. Phys. 1998;40(5):161-71.

13.   Delpuech J-J, Hamza MA, Serratice G, Stébé M-J. Fluorocarbons as oxygen carriers. I. An NMR study of oxygen solutions in hexafluorobenzene. J. Chem. Phys. 1979;13:399.

14.   Mason RP. Non-invasive physiology: ^{19}F NMR of perfluorocarbon. Art. Cells, Blood Sub. & Immob. Biotech. 1994;22(4):1141-1153.

15.   Hahn EW, Peschke P, Mason RP, Babcock EE, Antich PP. Isolated tumor growth in a surgically formed skin pedicle in the rat: a new tumor model for NMR studies. Magn. Reson. Imaging 1993;11:1007-1017.

16.   Laurence V, Ward R, Bleehen N. Tumor pO_2 distribution in patients treated with the combination of nicotinamide and carbogen breathing. In: P. W. Vaupel, D. K. Kelleher, M. Günderoth, eds. Tumor Oxygenation. Stuttgart: Gustav Fischer,, 1995: 185-193.

17.   Cater D, Silver I. Quantitative measurements of oxygen tension in normal tissues and in the tumors of patients before and after radiotherapy. Acta Radiol. 1960;53:233-256.

18.   Chaplin DJ, Horsman MR, Siemann DW. Further evaluation of nicotinamide and carbogen as a strategy to reoxgenate hypoxic cells *in vivo*: importance of nicotinamide dose and pre-irradiation breathing time. Br. J. Cancer 1993;68:269-73.

19. Dardzinski BJ, Sotak CH. Rapid tissue oxygen tension mapping using ^{19}F Inversion-recovery Echo-planar imaging of Perfluoro-15-crown-5-ether. Magn. Reson. Med. 1994;32(1):88-97.

20. Baldwin NJ, Ng TC. Oxygenation and metabolic status of KHT tumors as measured simultaneously by ^{19}F magnetic resonance imaging and ^{31}P magnetic resonance spectroscopy. Magn. Reson. Imaging 1996;14(5):514-551.

21. Fishman JE, Joseph PM, Carvlin MJ, Saadi-Elmandjra M, Mukherji B, Sloviter HS. *In vivo* measurements of vascular oxygen tension in tumors using MRI of a fluorinated blood substitute. Invest. Radiol. 1989;24:65-71.

22. Mason RP, Antich PP, Babcock EE, Constantinescu A, Peschke P, Hahn EW. Non-invasive determination of tumor oxygen tension and local variation with growth. Int. J. Radiat. Oncol. Biol. Phys. 1994;29: 95-103.

23. McIntyre DJO, McCoy CL, Griffiths JR. Tumour oxygenation measurements by ^{19}F MRI of perfluorocarbons. Curr. Sci. 1999;76:753-762.

24. Brown SL, Ewing JR, Lolozsvary A, Butt S, Cao Y, Kim JH. Magnetic Resonance Imaging of perfusion in rat cerebral 9L tumor after nicotinamide administration. Int. J. Radiat. Oncol. Biol. Phys. 1999;43:627-33.

25. Mason R, Hunjan S, He S, et al. Tumor trans membrane pH gradient and regional oxygen tension measured by fluorine magnetic resonance. In: Moraes M, Brentani R, Bevilacqua R, eds. 17th International Cancer Congress. Rio de Janeiro: Monduzzi, 1998: 1627-31. vol 2).

26. Mason RP. Transmembrane pH gradients *in vivo*: measurements using fluorinated vitamin B6 derivatives. *Curr. Med. Chem.* 1999;6:533-51.

27. Lancaster. Material Safety Data Sheet. In: Lancaster Synthesis Inc., 1998:

28. Hall LW, Jackson SRK, Massey GM. Hexafluorobenzene in veterinary anaesthesia. In: Arias A, Llaurado R, Nalda MA, Lunn JN, eds. Recent Progress in Anaesthesiology and Resuscitation. Oxford: Excerpta Medica, 1975: 201-204.

11

29.   Rietjens IMCM, Steensma A, den Besten C, et al. Comparative biotransformation of hexachlorobenzene and hexafluorobenzene in relation to the induction of porphyria. Eur. J. Pharmacol. 1995;293:292-299.

Figure legends

Figure 1

Comparison of oxygenation in size-matched groups of AT1 tumors based on ^{19}F MR EPI relaxometry (left) and electrode polarography (right), when rats inhaled 33% O_2. Small tumors are shown at top (volume < 2 cm^3) and large tumors below (volume > 3.5 cm^3). Each method shows a significant difference in tumor oxygenation for small versus large tumors ($p < 0.0001$).

Figure 2

a) Dynamic changes in pO_2 of six specific regions of an AT1 tumor. The three high pO_2 regions had significantly different pO_2 (* $p < 0.05$)) from those with low pO_2 at each time point. Within 8 mins of elevating inspired O_2 the three high pO_2 voxels had significantly increased pO_2 ($p < 0.05$) while the low pO_2 voxels required > 24 mins to show significant changes. All six regions were observed simultaneously using the FREDOM approach.

b) Dynamic changes in pO_2 of six specific regions of an AT1 tumor. The electrode was placed in one location at a time and inhaled gases cycled for subsequent locations.
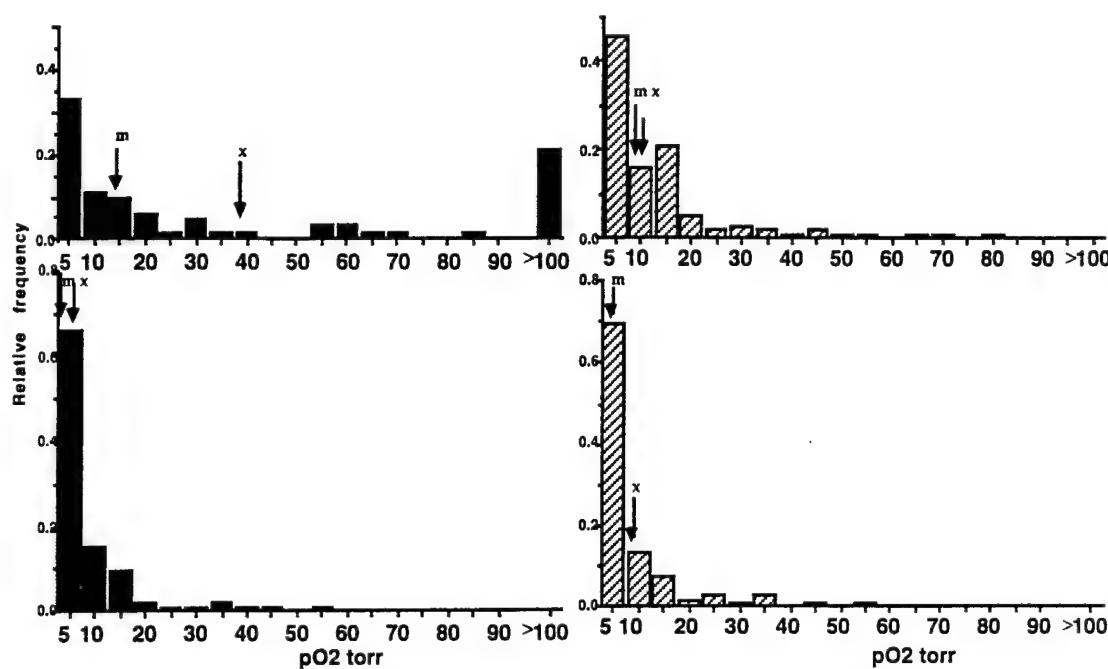
Figure 1
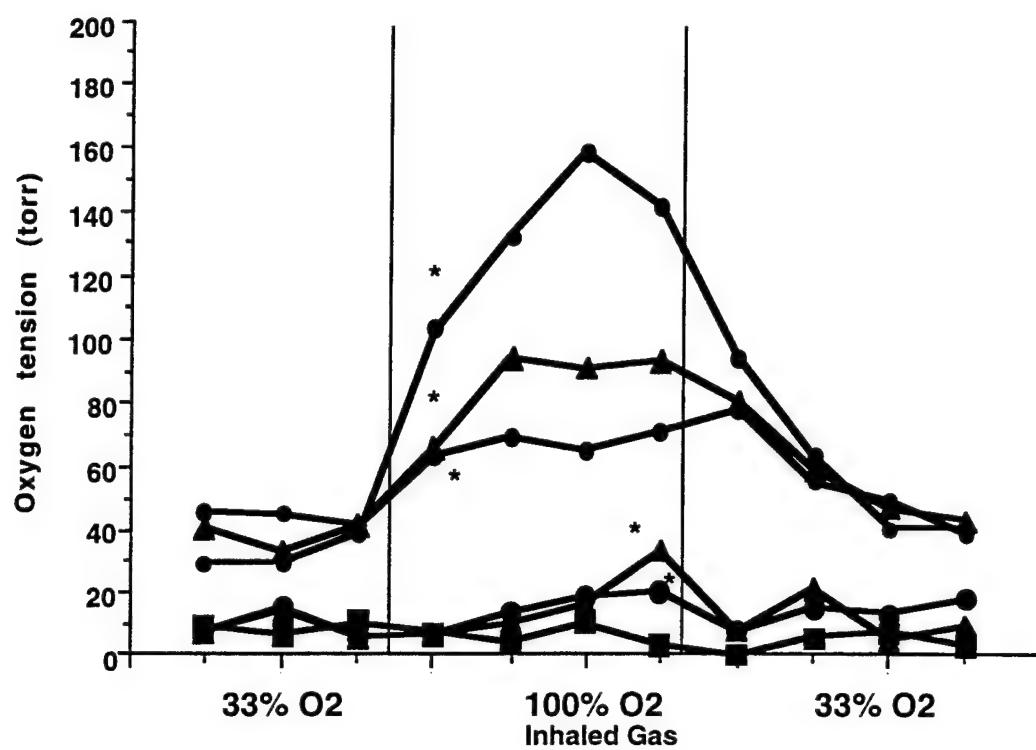
Figure 2a
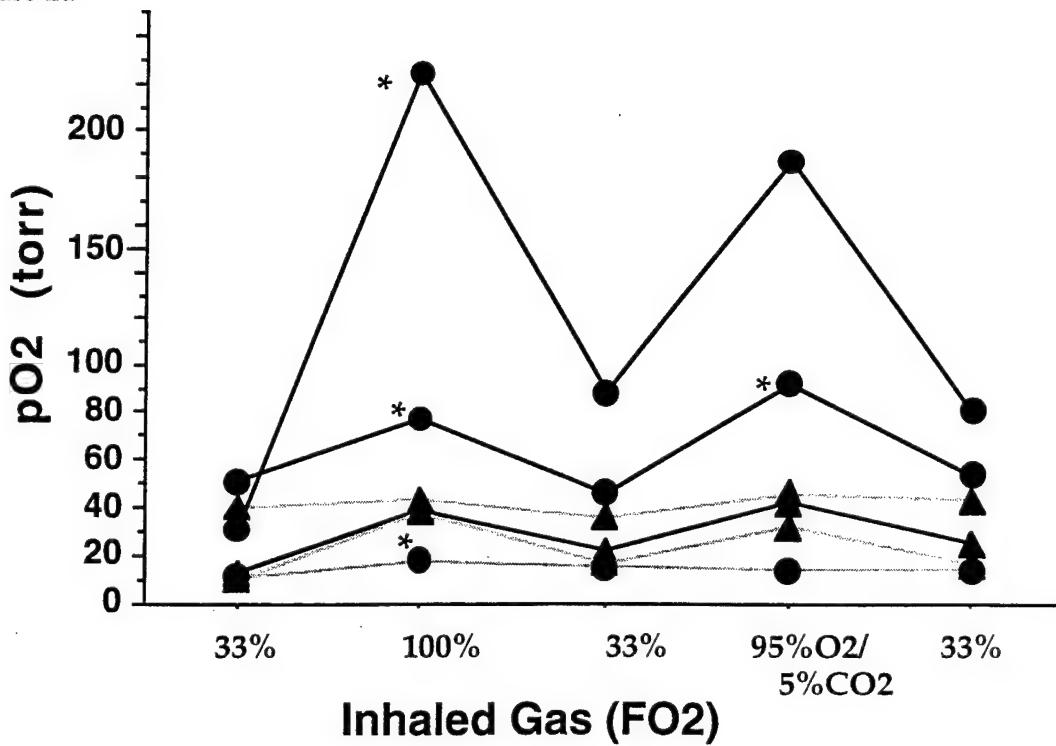
Figure 2b

14

Regional Tumor Oxygen Tension and Blood Flow:
Correlation Studies Using ^{19}F PBSR-EPI of Hexafluorobenzene

Y. Song, R. P. Mason, S. Hunjan, A. Constantinescu, E. W. Hahn, and P. P. Antich,
Department of Radiology, UT Southwestern Medical Center, Dallas, Texas, USA

Introduction: It is recognized that therapeutic efficacy may be influenced by tumor oxygenation. In particular, hypoxic tumors resist radiotherapy. We have recently shown the feasibility of monitoring tumor oxygen tension based on ^{19}F PBSR-EPI of hexafluorobenzene (HFB) [1]. We also found that HFB clears from tumors over a period of hours [2]. Since HFB is a non-ionic freely diffusable tracer, it appeared that clearance rate would provide an indication of relative tumor blood flow (TBF). We have now investigated the feasibility of mapping the clearance rate of HFB and correlating this putative blood flow marker with corresponding pO_2.

Methods: Dunning prostate R3327-AT1 or breast 13762 NF adenocarcinoma was implanted in a skin pedicle on the foreback of a rat. When the tumor reached 1~2 cm diameter, 40 μl HFB were injected directly into the tumor (IT), both centrally and peripherally. The rat was maintained under general gaseous anesthesia (33% O_2, 66% N_2O and 0.5% methoxyflurane). A homebuilt tunable 2 cm ^{1}H/^{19}F single turn solenoid coil was placed around the tumor and MR experiments were performed using a 4.7 T magnet equipped with actively shielded gradients. 3D ^{1}H images were acquired for anatomical reference and corresponding ^{19}F images were obtained to show the distribution of HFB. Tumor oxygenation was assessed using ^{19}F PBSR-EPI of HFB. By applying the acquisition protocol ARDVARC (Alternated Relaxation Delays with Variable Acquisitions to Reduce Clearance effects) [2], we achieved $R1$ maps in 8 min. A series of maps were acquired over a period of 2 hours with respect to respiratory challenges. pO_2 maps were then generated by applying the relationship: $pO_2(\text{torr}) = [R1(s^{-1}) - 0.074]/0.0016$ to the $R1$ maps. The data also allowed us to produce a clearance map based on EPI images with the longest delay (90 s).

Results: pO_2 maps were generated with a typical precision of 2 ~ 5 torr and 30 ~ 100 individual voxels within a tumor. For many regions, the HFB signal intensity was found to decline exponentially with a typical clearance half-life ranging from $T_{1/2}$ = 700 to 1200 min, though many voxels indicated no apparent changes.

Discussion: Regional tumor oxygen tension and blood flow are important physiological parameters and the opportunity to measure both simultaneously would be of value in physiological research. Based on the preliminary data presented here, we believe that clearance of HFB provides an indication of relative TBF by analogy with studies of cerebral blood flow using freon-23 [3]. In future studies, such measurements will be rigorously evaluated.

References:
[1] D. Le, *et al.*, *MRI*, 15, 971-981 (1997). [2] S. Hunjan, *et al.*, *IJROBP*, 41, 161-171 (1998)
[3] J. R. Ewing, *et al.*, *Stroke*, 21, 100-106 (1990).

TUMOR OXIMETRY: COMPARISON OF ^{19}F MR EPI AND ELECTRODES

Mason, Ralph; Hunjan, Sandeep; Constantinescu, Anca; Song, Yulin; Zhao, Dawen; Hahn, Eric; Antich, Peter; and Peschke, Peter[+]. U.T. Southwestern Medical Center, Dallas, TX and [+]DKFZ, Heidelberg, Germany

Therapeutic efficacy may be influenced by tumor oxygenation. In particular, hypoxic tumors resist radiotherapy and may be good candidates for hypoxia selective cytotoxic agents. We recently described a novel approach to measuring regional tumor oxygen tension using ^{19}F pulse burst saturation recovery (PBSR) nuclear magnetic resonance (NMR) echo planar imaging (EPI) relaxometry of hexafluorobenzene (HFB) (1). We have now compared oxygen tension measurements in a group of size matched Dunning prostate rat tumors R3327-AT1 made using this new method with a traditional polarographic method: the Eppendorf Histograph. We also demonstrate extension of the MR technique to rat breast tumors.

Methods: Dunning prostate R3327-AT1 or breast 13762 NF adenocarcinoma was implanted in a skin pedicle on the foreback of a rat. When the tumor reached a volume ~2 cm^3 or > 3.5 cm^3, 40 μl HFB were injected directly into both central and peripheral regions of the tumor. The rat was maintained under general anesthesia (33% O_2, 66% N_2O and 0.5% methoxyflurane). A tunable 2 cm ^{1}H/^{19}F single turn solenoid coil was placed around the tumor and MR experiments were performed using a 4.7 T magnet equipped with actively shielded gradients. 3D ^{1}H images were acquired for anatomical reference and corresponding ^{19}F images were obtained to show the distribution of HFB. Tumor oxygenation was assessed using ^{19}F PBSR-EPI of HFB. A series of pO_2 maps was acquired over a period of 2 hours with respect to respiratory challenge using the relationship: pO_2 (torr) = (R1-0.074)/0.0016. Histography was applied to groups of size matched tumors, which did not receive HFB.

Results: Similar oxygen tension distributions were found using each method and both techniques showed that tumors with volume > 3.5 cm^3 were significantly ($p < 0.0001$) less well oxygenated than smaller tumors (volume < 2 cm^3). Using the ^{19}F EPI approach we also examined response to respiratory challenge. Increasing the concentration of inspired oxygen from 33% to 100% O_2 produced a significant increase ($p < 0.0001$) in tumor oxygenation for a group of small tumors. In contrast no change was observed in the mean pO_2 for a group of large tumors. Consideration of individual tumor regions, irrespective of tumor size showed a strong correlation between the maximum pO_2 observed when breathing 100% O_2, as compared with mean baseline pO_2.

Discussion: These results demonstrate the similarity of results obtained using electrode or MR approaches to tumor oximetry. They also indicate the feasibility of ^{19}F MR to monitor dynamic changes in regional pO_2 in response to acute interventions. The ability to measure pO_2 could be valuable in pre-clinical evaluation of novel therapies and could allow therapy to be individualized and optimized for patients.

Reference:
1. D. Le, R. P. Mason, S. Hunjan, A. Constantinescu, B. R. Barker and P. P. Antich, Regional tumor oxygen dynamics: ^{19}F PBSR EPI of hexafluorobenzene. *Magn. Reson. Imaging*, 15, 971-81 (1997).
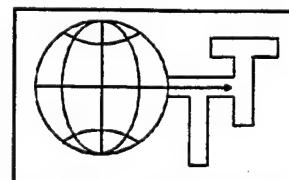
TUMOR OXYGEN DYNAMICS: COMPARISON BETWEEN ^{19}F MR-EPI OF HEXAFLUOROBENZENE AND FREQUENCY DOMAIN NIR SPECTROSCOPY

Song[1,2], Y.; Worden[1], K. L.; Jiang[1], X.; Zhao[2], D.; Constantinescu[2], A.; Liu[1], H.; and Mason[2], R. P.
[1]Joint Graduate Program in Biomedical Engineering,
[2]Department of Radiology, UT Southwestern Medical Center, Dallas, TX 75235, USA

Introduction: Oxygen plays a key role in tumor therapy and may be related to tumor development: *e.g.*, angiogenesis and metastasis. Using noninvasive techniques to accurately measure oxygenation could assist in developing novel therapies. Here, we have used ^{19}F MR-EPI relaxometry of hexafluorobenzene (HFB)[1] to monitor tissue oxygen tension (pO_2) of rat breast tumors and compared the results with changes in hemoglobin saturation (sO_2) and concentration in the vasculature of the tumors observed using a new dual wavelength homodyne near-infrared (NIR) system.

Methods: Breast 13762 NF adenocarcinomas were implanted in skin pedicles on the forebacks of adult female Fischer rats. Once the tumors reached ~1cm diameter, the tumor blood sO_2 was assessed by NIR spectroscopy using a dual wavelength NIR system (758 nm and 782 nm) in transmission geometry [2]. The tumor blood volume and sO_2 were calculated from the light amplitude. The rats were maintained under general gaseous anesthesia (33% O_2, 66% N_2O and 0.5% methoxyflurane). Once stable baseline measurements were achieved, the inhaled gas was altered to pure oxygen or carbogen and dynamic changes were observed over a period of two hours. Both the magnitude and rate of change of sO_2 were examined. Following the NIR experiments, 40 µl HFB were injected directly into both central and peripheral regions of the tumors. A tunable 2 cm ^{1}H/^{19}F single turn solenoid coil was placed around the tumor and MR experiments were performed using a 4.7 T magnet. Regional tumor pO_2 was estimated using the relationship: $pO_2(torr) = [R1 - 0.074]/0.0016$, where $R1$ is the spin lattice relaxation rate of HFB. Twenty-three pO_2 maps were produced in 3 hours with respect to respiratory challenge.

Results: NIR showed significant changes in vascular oxygenation accompanying respiratory interventions. [19]F MR-EPI also showed significant changes in tissue pO_2, with considerable regional heterogeneity in both absolute values and rate of change accompanying interventions. Generally, changes in vascular sO_2 preceded tissue pO_2, particularly for smaller tumors.

Discussion: Regional tumor pO_2 and blood sO_2 are important physiological parameters. The capability to measure them will provide insight into progressive physiological changes in a tumor accompanying interventions. NIR has the advantage of being entirely noninvasive, but the MRI approach clearly reveals detailed oxygenation heterogeneity. We believe that better understanding and monitoring of tumor oxygenation can lead to improved tumor therapy.

References:
[1] D. Le, *et al.*, *MRI*, 15, 971-981 (1997). [2] K. Worden, *et al.*, SPIE, 3597 (1999)
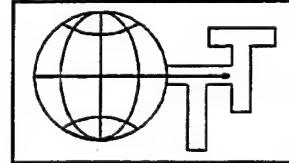
Tumor oxygenation and measurement of regional dynamic changes

Ralph P. Mason, Sandeep Hunjan, Anca Constantinescu, Yulin Song, Eric W. Hahn, and Peter P. Antich, Advanced Radiological Sciences, U.T. Southwestern Medical Center, Dallas, Texas and Christian Blum and Peter Peschke, Deutsches Krebsforschungszentrum, Heidelberg, Germany

Therapeutic efficacy may be influenced by tumor oxygenation. In particular, hypoxic tumors resist radiotherapy and may be good candidates for hypoxia selective cytotoxic agents. We recently described a novel approach to measuring regional tumor oxygen tension using ^{19}F pulse burst saturation recovery (PBSR) nuclear magnetic resonance (NMR) echo planar imaging (EPI) relaxometry of hexafluorobenzene (HFB) (1). We have now compared oxygen tension measurements in a group of size matched Dunning prostate rat tumors R3327-AT1 made using this new method with a traditional polarographic method: the Eppendorf Histograph. We also demonstrate extension of the MR techniques to rat breast tumors.

Methods: Rat Dunning prostate R3327-AT1 or breast 13762 NF adenocarcinomas were examined at a volume <2 cm^3 or > 3.5 cm^3: for MRI 40 μl HFB were injected directly into the tumor, both centrally and peripherally. The rat was maintained under general gaseous anesthesia (33% O_2, 66% N_2O and 0.5% methoxyflurane). A tunable 2 cm ^{1}H/^{19}F single turn solenoid coil was placed around the tumor and MR experiments were performed using a 4.7 T magnet equipped with actively shielded gradients. Tumor oxygenation was assessed using ^{19}F PBSR-EPI of HFB. By applying the acquisition protocol ARDVARC (Alternated Relaxation Delays with Variable Acquisitions to Reduce Clearance effects), we achieved R1 maps in 8 min. A series of maps was acquired over a period of 2 hours with respect to respiratory challenges. pO2 maps were then generated by applying the relationship: pO_2 (torr) = (R1 -0.074)/0.0016. In parallel experiments pO_2 was determined polarographically

Results: Similar oxygen tension distributions were found using ^{19}F MRI or polarography and both techniques showed that tumors with volume > 3.5 cm^3 were significantly ($p < 0.0001$) less well oxygenated than smaller tumors (volume < 2 cm^3). Using the ^{19}F EPI approach we also examined response to respiratory challenge. Increasing the concentration of inspired oxygen from 33% to 100% O_2 produced a significant increase ($p < 0.0001$) in tumor oxygenation for a group of small tumors. In contrast no change was observed in the mean pO_2 for a group of large tumors. Consideration of individual tumor regions, irrespective of tumor size showed a strong correlation between the maximum pO_2 observed when breathing 100% O_2. as compared with mean baseline pO_2.

Conclusions: These results further demonstrate the usefulness of ^{19}F EPI to assess changes in regional tumor oxygenation. The ability to measure pO_2 could be valuable in pre-clinical evaluation of novel therapies and ultimately allow therapy to be individualized and optimized for patients.

1. D. Le, R. P. Mason, S. Hunjan, A. Constantinescu, B. R. Barker and P. P. Antich, Regional tumor oxygen dynamics: ^{19}F PBSR EPI of hexafluorobenzene. *Magn. Reson. Imaging.* 15. 8, 971-81 (1997).

REGIONAL TUMOR OXYGEN DYNAMICS: RELATING TISSUE pO_2 TO THE VASCULATURE

Y. Song[1,2], X. Jiang[1], D. Zhao[2],
A. Constantinescu[2], H. Liu[1], and R. P. Mason[2]

[1]*Joint Graduate Program in Biomedical Engineering,*
[2]*Department of Radiology, UT Southwestern Medical Center, Dallas, TX 75235, USA*

E-mail: song1058@hotmail.com

INTRODUCTION Tumor oxygenation has a critical influence on success in radiotherapy and is thought to play a key role in angiogenesis and metastasis. However, no non-invasive procedure for tumor oximetry has been established in clinical practice, so far. Here, we present and compare two oximetry techniques: the FREDOM (Fluorocarbon Relaxometry using Echo planar imaging for Dynamic Oxygen Mapping) approach based on hexafluorobenzene (HFB) to measure tumor tissue oxygen tension (pO_2) and near infrared (NIR) spectroscopy based on a new I/Q system to measure changes in tumor vascular hemoglobin saturation (sO_2) and concentration [Hb].

METHODS NF 13762 breast adenocarcinomas were implanted in skin pedicles on the forebacks of adult female Fischer rats. Once the tumors reached ~1 cm diameter, the dynamic characteristics of tumor vascular sO_2 in response to respiratory challenge were monitored by NIR spectroscopy. Then, 40 µl HFB were injected directly into the tumor. 3-D MR spin-echo ^1H images were acquired for anatomical reference and corresponding ^{19}F images were then obtained to reveal the distribution of HFB in the tumor. The dynamic characteristics of regional tumor pO_2 were assessed using FREDOM.

RESULTS Tumor vascular sO_2 increased rapidly after a gas switch from baseline (33% O_2) to either carbogen or 100% O_2 and then slowly returned to baseline after the gas was switched back to baseline. Total hemoglobin change was insignificant. Tumor tissue pO_2 also showed significant changes, but with considerable regional heterogeneity in both absolute values and rate of change. Changes in sO_2 preceded those in pO_2. Tumor voxels with high baseline pO_2 had significantly different response characteristics from those with initially low pO_2, with voxels of high baseline pO_2 showing significant changes in pO_2, while voxels of low baseline pO_2 showing small changes. Strong correlation existed between the maximum pO_2 value attained during the course of an experiment and mean baseline pO_2.

CONCLUSIONS Synergistic application of the FREDOM and NIR techniques will provide new insight into issues of tumor angiogenesis and perfusion, and could lead to improved tumor therapy.

DIVERSE APPROACHES TO MONITORING OXYGEN DYNAMICS IN RAT BREAST AND PROSTATE TUMORS

Dawen Zhao, Yulin Song, Hanli Liu[+], Anca Constantinescu, Eric W. Hahn, and Ralph P. Mason, Department of Radiology, UT Southwestern, Dallas, TX 75390 and [+]BME, UT-Arlington, TX 76109

Summary: The increasing evidence that direct measurement of pO_2 in patient's tumors has prognostic value provides strong impetus to develop robust methods for measuring tumor oxygen dynamics. Using the *FREDOM* NMR approach (Fluorocarbon Relaxometry using Echo planar imaging for Dynamic Oxygen Mapping) we are able to examine regional variations in tumor pO_2 in response to interventions. To obtain a more complete view of vascular dynamics, we now incorporate Near Infrared (NIR) measurements of hemoglobin concentration [Hb] and saturation ($sHbO_2$) in tumors.

Methods: Dunning prostate R3327 (AT1 and HI) and 13762NF breast tumors were implanted in pedicles (1) on the foreback of syngeneic Copenhagen and Fisher rats, respectively. Once tumors reached ~ 1 cm diameter, rats were anesthetized (generally, 1.2% isoflurane in air) and examined using a homodyne dual wavelength NIR device in transmission mode, to monitor relative $\Delta[Hb]$ and $\Delta sHbO_2$ (2). A pulse oximeter simultaneously provided s_aO_2 in the leg. Variations in these values were observed with respect to respiratory challenge and vasoactive drugs (oxygen, carbogen and hydralazine). The following day the same tumors were interrogated by ^{19}F NMR EPI with respect to the same interventions (3). Hexafluorobenzene (45 μl) was injected directly into both central and peripheral regions of the tumors using a fine sharp needle (32G) and pO_2 maps determined with 8 minute time resolution and 1.25 mm in plane spatial resolution using pulse burst saturation NMR echo planar imaging relaxometry (*FREDOM*). In some instances, additional studies were performed using oxygen microelectrodes and the OxyLite™ optical fiber sensor.

Results: As expected, the fastest changes in oxygenation in response to respiratory challenge occurred in the arterial saturation (s_aO_2) in the leg with a typical time constant $\tau < 20$ s (Fig. 1). Small tumors often showed biphasic vascular response with a rapid ΔHbO_2 component ($\tau < 30$ s) approaching that of s_aO_2 and a more sluggish component increasing over 20 mins. The slow component alone was typical of larger tumors. Changes in $\Delta[Hb]$ indicated that vascular volume was also modulated. Changes in tumor tissue pO_2 were highly variable. Well oxygenated regions responded significantly with a time constant in the range $\tau = 10 - 30$ mins. The response of initially poorly oxygenated regions was highly tumor dependent. AT1 tumor regions initially <10 torr showed little response, whereas most regions in the slower growing HI responded, significantly reducing the hypoxic fraction with oxygen or carbogen (see accompanying abstract by Zhao *et al.*). Although the breast tumors grow rapidly, hypoxic regions were also found to respond in these tumors (Fig. 2). Both oxygen microelectrodes and the OxyLite™ showed changes in pO_2 which were comparable to the *FREDOM* results, in terms of both rates and magnitude of change.

Conclusions: The *FREDOM* approach allows dynamic changes in regional tumor pO_2 to be followed in diverse tumors. These data indicate that regional response to respiratory challenge depends not only on the baseline tumor oxygenation, but also the degree of tumor differentiation. By adding NIR, we are additionally able to probe changes in vascular volume and hemoglobin oxygen saturation. These preliminary data were obtained sequentially, but

simultaneous NIR and *FREDOM* investigations are imminently feasible to provide deeper insight into tumor vascular phenomena. We believe the complimentary applications of the two techniques will provide deeper insight into tumor physiology and mechanisms of modulating tumor physiology for therapeutic enhancement.
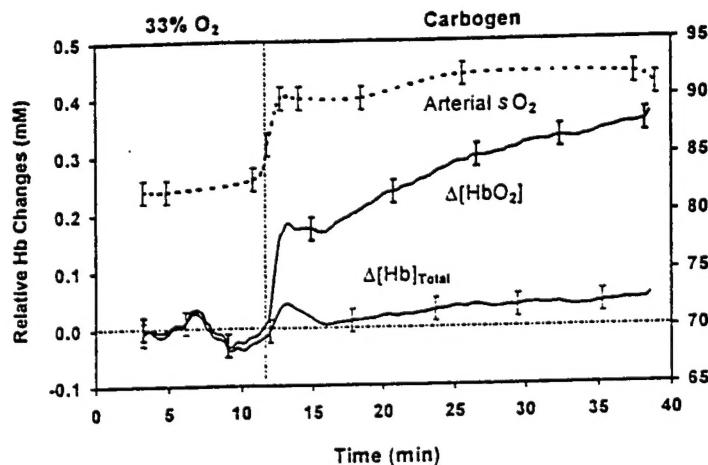

Fig. 1 Dynamic response in s_aO_2, ΔHbO_2, and ΔHb_{Total} in 4.5-cm^3 rat breast tumor with respect to respiratory challenge observed using NIR instrument. A bi-exponential curve fit for changes in ΔHbO_2 gave time constants $\tau_1 = 11$ s and $\tau_2 = 27.8$ mins, respectively.
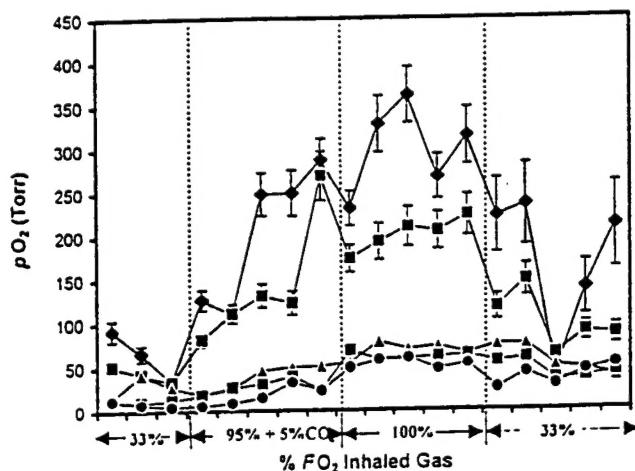

Fig. 2 Dynamic changes in pO_2 measured using *FREDOM* of representative regions in a second breast tumor (3.5 cm^3). The local response depended strongly on initial baseline pO_2, both in terms of rate and magnitude (measurements at 8 min intervals).

References
1. Hahn, E. W., Peschke, P., Mason, R. P., Babcock, E. E., and Antich, P. P. Isolated tumor growth in a surgically formed skin pedicle in the rat: A new tumor model for NMR studies., Magn. Reson. Imaging. *11:* 1007-1017, 1993.
2. Liu, H., Song, Y., Worden, K. L., Jiang, X., Constantinescu, A., and Mason, R. P. Noninvasive Investigation of Blood Oxygenation Dynamics of Tumors by Near-Infrared Spectroscopy, *Appl. Optic,* in the press 2000.
3. Mason, R. P., Constantinescu, A., Hunjan, S., Le, D., Hahn, E. W., Antich, P. P., Blum, C., and Peschke, P. Regional tumor oxygenation and measurement of dynamic changes, Radiat. Res. *152:* 239-249, 1999.

FREDOM (Fluorine Relaxometry using Echo planar imaging for Dynamic Oxygen Mapping): a contextual review.

Ralph P. Mason, Dawen Zhao, Anca Constantinescu, Yulin Song, Lan Jiang & Eric W. Hahn, Department of Radiology, UT Southwestern Medical Center, Dallas, Texas 75390

Tumor oxygenation has been widely recognized as a potent factor, which influences tumor response to therapy. Recent development of methods to measure pO_2 in the clinic has generated data confirming a prognostic relationship between tumor pO_2 and clinical outcome. Such results provide a powerful stimulus for development of enhanced methods for monitoring tumor oxygenation. Many diverse techniques exist with characteristic virtues, providing unique insight, as represented by this session on Tumor Oximetry. We have developed an approach using ^{19}F NMR echo planar relaxometry of hexafluorobenzene (HFB) following direct intra tumoral administration. Currently, this provides maps of pO_2 in eight minutes with a typical precision of 1-3 torr at 30 – 100 locations within a plane of an individual tumor. We will describe applications to interrogate pO_2 dynamics in response to a variety of interventions, such as respiratory challenge and vasoactive drugs in rat prostate and breast tumors and human lymphoma.

FREDOM exploits the well known sensitivity of the spin lattice relaxation rate, R1, of perfluorocarbons to oxygen. The choice of HFB as the interrogating molecule reflects its remarkable characteristics: single resonance, which is exceedingly sensitive to changes in pO_2 [pO_2 (torr)= (R1-0.0835)/0.001876 at 37 °C], while being insensitive to changes in temperature [at 5 torr and 37 °C, a 2 °C error in temperature estimate would yield An error in pO2 =??]. Hexafluorobenzene is readily available, cheap and has well documented lack of toxicity.

Correlative studies show that results achieved using FREDOM or the Eppendorf electrode system provide a similar representation of a tumor (1). Investigation of dynamic changes at specific locations show similarity with polarographic electrodes or fiber optic probes. Most tumors exhibit great heterogeneity in baseline oxygenation with regions ranging from relatively hypoxic (< 5 torr) to well oxygenated (> 20 torr). Most tumors show reduced baseline pO_2 at larger size, *e.g.*, in the anaplastic Dunning prostate R3327-AT1 subline (Volume doubling time (VDT) ~ 5 days) tumors with a vol. > 3.5 cm^3 were significantly (p < 0.0001) less well oxygenated than tumors (< 2 cm^3). Similar results were found in the slower growing moderately well differentiated R3327-HI subline (VDT ~ 10 days). Changes in pO_2 in response to respiratory challenge with oxygen or carbogen were found to be dependent on baseline pO_2 in the AT1 tumor. However, by contrast, even the poorly oxygenated areas of the HI tumors were very sensitive, and responded with highly significant transient increases in pO_2. These findings, if confirmed, in human tumors could be valuable in treatment planning.

We believe the ability to probe oxygen tension dynamics quantitatively at multiple selected locations of interest within a tumor will be valuable in probing tumor development and the efficacy of adjuvant interventions to modulate tumor physiology.

1. Mason, R. P., Constantinescu, A., Hunjan, S., Le, D., Hahn, E. W., Antich, P. P., Blum, C., and Peschke, P. Regional tumor oxygenation and measurement of dynamic changes, Radiat. Res. *152:* 239-249, 1999.

Regional Tumor Tissue pO_2 and Blood sO_2 : Comparison of ^{19}F MR EPI and Frequency Domain NIR Spectroscopy

Y. Song[1,2]; X. Jiang[1]; D. Zhao[2]; A. Constantinescu[2]; H. Liu[1]; and R. P. Mason[2]

[1]*Joint Graduate Program in Biomedical Engineering,*
[2]*Department of Radiology, UT Southwestern Medical Center, Dallas, TX 75235, USA*

INTRODUCTION

Tumor oxygenation has a profound effect on growth and development, and hypoxia reduces radiosen-sitivity. Moreover, increasing evidence from clinical trials has indicated that poorly oxygenated tumors have poor prognosis. Therefore, development of non-invasive techniques to accurately measure oxygenation is essential in cancer treatment planning and prognosis prediction. Here, we present and compare two such techniques: the FREDOM (Fluorocarbon Relaxometry using Echo planar imaging for Dynamic Oxygen Mapping) approach based on hexafluorobenzene (HFB)[1] to measure tumor tissue oxygen tension (pO_2) and NIR spectroscopy to measure changes in tumor vascular hemoglobin saturation (sO_2) and concentration [Hb]. The synergistic application of MR and NIR techniques could provide new insight into issues of tumor angiogenesis and perfusion.

METHODS

NF 13762 breast and Dunning prostate R3327-AT1 adenocarcinomas were implanted in skin pedicles on the forebacks of adult female Fischer and male Copenhagen rats (~250 g), respectively. Once the tumors reached ~1 cm diameter, the rats were anesthetized with 200 μl ketamine hydrochloride (100 mg/ml) and maintained under general gaseous anesthesia (33% O_2, 66% N_2O and 0.5% methoxyflurane). The tumor vascular sO_2 was assessed by NIR spectroscopy using a new dual wavelength, homodyne system (wavelengths 758 nm and 782 nm)[2], while inhaled gas was alternated between 33% O_2, carbogen (95% O_2 + 5% CO_2), and 100% O_2. The light amplitude and phase changes caused by the tumor are related to changes in hemoglobin concentration [Hb] and hemoglobin saturation [HbO_2], i.e., sO_2:

$$\Delta[Hb]_{total} = - [3.56^* \log (A_I/A_C)^{758} + 8.59^* \log (A_I/A_C)^{782}]/d \quad (1)$$

$$\Delta[HbO_2] - \Delta[Hb] = - [18.27^* \log (A_I/A_C)^{758} + 20.92^* \log (A_I/A_C)^{782}]/d \quad (2)$$

where A_I is the initial amplitude (amplitude of baseline), A_C the current amplitude, d the direct source-detector separation in cm, and $\Delta[]$ the change in concentration in mM.

Following the NIR experiments, a tunable 2 cm ^{1}H/^{19}F single turn solenoid coil was placed around the tumor and 40 μl HFB were injected directly into both central and peripheral regions of the tumor using a 32 G needle. 3D spin-echo (SE) ^{1}H images were acquired for anatomical reference and corresponding ^{19}F images were then obtained to show the distribution of HFB in the tumor. Regional tumor pO_2 maps were generated using ^{19}F PBSR-EPI based on the relationship: $pO_2(\text{torr}) = [R1 - 0.0836]/0.00188$, where $R1$ (1/T) is the spin lattice relaxation rate of HFB in 1/sec.

RESULTS

Tumor vascular sO_2 increased almost immediately after a gas switch from baseline (33% O_2) to either carbogen or 100% O_2 and increased steadily for several minutes, and then gradually returned to baseline after the gas was switched back to baseline. In contrast, total hemoglobin change was insignificant, indicating relatively constant blood volume in the tumor. Tumor tissue pO_2 also showed significant changes, but with considerable regional heterogeneity in both absolute values and rate of change. Both carbogen and 100% O_2 inhalation produced significant changes in sO_2 and pO_2, especially with 100% O_2 inhalation. Temporal dynamic response in both sO_2 and pO_2 were modeled and exponential time constants were determined. The FREDOM technique also allowed us to compute the time constant on a voxel-by-voxel basis. It was found that sO_2 had a faster time constant than pO_2, especially in the cases of larger tumors, which were found to be less well oxygenated and presumably less well perfused. It was also found that some tumors showed a bimodal response (slow plus fast) in sO_2, as compared to a unimodal response (slow) in pO_2.

DISCUSSION

An increase in inspired gas FO_2 should lead to increased tumor vascular sO_2, and hence, increased tumor tissue pO_2. Our data indicate that breathing elevated O_2 did indeed have a significant effect on both tumor vascular sO_2 and tissue pO_2. Vascular sO_2 values were found to have a faster time constant than tumor tissue pO_2, with greater differences in large tumors. This probably reflects the extensive perfusion of the small tumors with lesser perfusion of large tumors since time constant should be inversely proportional to tumor blood flow (TBF), as reflected by lower mean pO_2 and larger hypoxic fraction. We believe that application of multiple approaches to tumor oxygenation can lead to better understanding of tumor physiology and probably optimized tumor therapy.

ACKNOWLEDGMENTS

REFERENCES

1. Le, D., Mason, R.P., Hunjan, S., Constantinescu, A., Barker, B.R., and Antich, P.P., *Regional Tumor Oxygen Dynamics: ^{19}F PBSR EPI of Hexafluorobenzene*. Magn. Reson. Imaging. 15:971-981, 1997.

2. Yunsong, Y., Liu, H., Li, X., and Chance, B., *Low-Cost Frequency-Domain Photon Migration Instrument for Tissue Spectroscopy, Oximetry, and Imaging*. Opt. Eng. 36(5):1562-1569, 1997.